

# Unravelling the mechanism of ultrafast photoinduced charge generation in organic and hybrid photovoltaic systems

Présentée le 9 décembre 2022

Faculté des sciences de base

Groupe Moser

Programme doctoral en chimie et génie chimique

pour l'obtention du grade de Docteur ès Sciences

par

## George Cameron FISH

Acceptée sur proposition du jury

Prof. J. Vanicek, président du jury

Prof. J.-E. Moser, directeur de thèse

Prof. E. Vauthey, rapporteur

Prof. N. Stingelin, rapporteuse

Prof. K. Sivula, rapporteur





## Abstract

At the current time, the world as we know it is at a crossroads; there is an urgent need to lower greenhouse gas emissions to limit the global rise in temperature. However, this is at odds with the increasing energy demands of the world's growing population. As such, to ensure that we can have our cake and eat it too, it is necessary to further develop renewable and low-carbon energy sources to minimise irreversible damage to our planet.

Third generation solar photovoltaics are low-cost materials which can generate electricity whilst having a minimal impact on the environment. To ensure efficiencies of these materials continue to improve, it is necessary to have a good fundamental understanding of how they generate charges, as well as the fate of these charges. This allows us to provide vital information to further material design, and thus push device efficiencies to new highs.

The first chapter of this thesis will provide the scientific background and historical context as well as introducing the material systems that will be studied later. Likewise, the second chapter introduces the laser-based ultrafast spectroscopic techniques that will be used to probe the ultrafast charge generation processes.

The third chapter focuses on neat pentamethine cyanine dyes; in particular, transient absorption spectroscopy is used to evidence high efficiency intrinsic charge generation occurring via a symmetry-breaking charge separation process. The efficiency of this process was shown to be dependent on the size of the counterion used, allowing us to conclude that the interchromophore distance and degree of H-aggregation are vital

parameters in ensuring efficient charge generation.

The first part of the fourth chapter explores whether a similar symmetry-breaking charge separation process could occur in neat dicyanomethylene-substituted squaraine dyes. Transient absorption spectroscopy, on both neat squaraine and squaraine/C<sub>60</sub> bi-layer samples, was used to determine that intrinsic charge generation cannot occur. The second part of this chapter focuses on the photochemistry of spiro-OMeTAD, a material often exploited as a hole transport layer in third generation solar cells. Once again, transient absorption spectroscopy was used to show that oxidised spiro-OMeTAD was generated via a symmetry-breaking charge separation process which could be catalysed by the addition of lanthanum-based TFSI salts.

The final results chapter targets two-dimensional hybrid organic-inorganic lead halide perovskites, where the impact of spacer size and layer orientation on the photo-generation of charge transfer excitons was studied using temperature dependent transient absorption spectroscopy. Furthermore, electroabsorption spectroscopy was used as a novel method to quantify the strength of the photoinduced electric field. Finally, it was possible to demonstrate that charge transfer can occur between the perovskite and electroactive naphthalene diimide-based spacers, an important result for future material design.

Key words: cyanine dyes - squaraine dyes - symmetry-breaking - intrinsic charge generation - two-dimensional perovskites - charge transfer excitons - ultrafast spectroscopy





## Résumé

A l'heure actuelle, le monde tel que nous le connaissons est à la croisée des chemins : il est urgent de réduire les émissions de gaz à effet de serre afin de limiter l'augmentation de la température moyenne globale. Cependant, cela va à l'encontre de la demande énergétique croissante et de l'augmentation de la population mondiale. Pour avoir le beurre et l'argent du beurre, il est donc nécessaire de développer davantage les sources d'énergies renouvelables et non carbonnées pour minimiser les dommages irréversibles causés à notre planète.

Les systèmes photovoltaïques de troisième génération sont basés sur des matériaux peu coûteux qui peuvent produire de l'électricité tout en ayant un impact minimal sur l'environnement. Pour que l'efficacité de ces matériaux continue à s'améliorer, il est nécessaire d'avoir une bonne compréhension fondamentale de la façon dont ils génèrent des charges sous l'effet de la lumière, ainsi que du devenir de ces charges. Cela nous permettra de fournir des informations vitales pour la conception des matériaux, et donc de pousser l'efficacité des dispositifs vers de nouveaux sommets.

Le premier chapitre de cette thèse présente le contexte scientifique et historique ainsi que les systèmes de matériaux qui seront étudiés par la suite. De même, le deuxième chapitre présente les techniques spectroscopiques basées sur des impulsions laser ultracourtes qui seront utilisées pour sonder les processus de génération de charges ultrarapides.

Le troisième chapitre se concentre sur des sels solides de colorants cyanine pentaméthine intacts ; en particulier, la spectroscopie d'absorption transitoire est utilisée

pour mettre en évidence la haute efficacité de la génération photoinduite intrinsèque de charges par un processus de séparation de charges par brisure de symétrie. L'efficacité de ce processus dépend de la taille du contre-ion utilisé, ce qui nous permet de conclure que la distance entre les chromophores et le degré d'agrégation H sont des paramètres essentiels pour assurer une génération de charges efficace.

La première partie du quatrième chapitre examine si un processus similaire de séparation de charge par brisure de symétrie pourrait se produire dans les colorants squaraines substitués par un dicyanométhylène. La spectroscopie d'absorption transitoire a été appliquée à des films de squaraine pure et de bicouches squaraine/C<sub>60</sub>, a été utilisée pour déterminer si la génération de charge intrinsèque peut se produire. La deuxième partie de ce chapitre se concentre sur la photochimie du spiro-OMeTAD, un matériau souvent exploité comme couche de transport de trous dans les cellules solaires de troisième génération. Une fois de plus, la spectroscopie d'absorption transitoire a été utilisée pour montrer que le spiro-OMeTAD oxydé était généré par un processus de séparation de charge par brisure de symétrie qui pourrait être catalysé par l'ajout de sels TFSI à base de lanthane.

Le dernier chapitre de résultats porte sur les pérovskites hybrides organiques-inorganiques bidimensionnelles d'halogénure de plomb - l'impact de la taille et de l'orientation de la barrière organique sur la photogénération d'excitons de transfert de charge a été étudié en utilisant la spectroscopie d'absorption transitoire dépendante de la température. En outre, la spectroscopie d'électroabsorption a été utilisée comme une nouvelle méthode pour quantifier l'intensité du champ électrique photoinduit. Enfin, il a été possible de démontrer qu'un transfert de charge peut se produire entre la pérovskite et les barrières organiques électroactives à base de naphthalène diimide, un résultat important pour la conception de futurs matériaux.

Mots-clés : cyanines - squaraines - brisure de symétrie - photo-génération intrinsèque de charges - pérovskites bidimensionnelles - excitons de transfert de charges - spectroscopie ultrarapide



# Contents

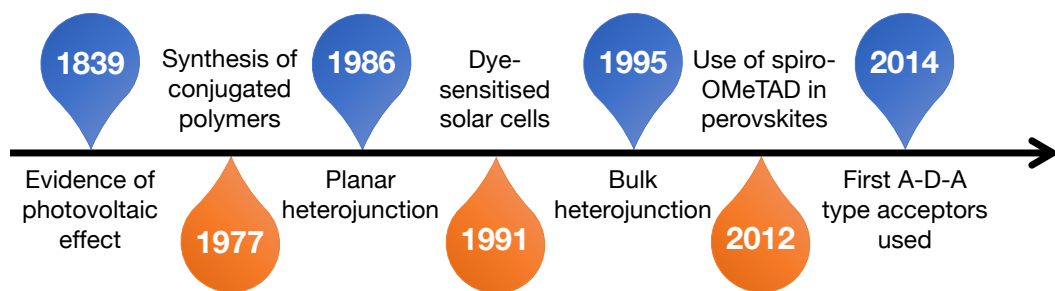
<b>Abstract</b>	<b>iii</b>
<b>Résumé</b>	<b>v</b>
<b>1 Introduction</b>	<b>1</b>
1.1 Why action is needed . . . . .	2
1.2 Scientific background . . . . .	4
1.2.1 Light . . . . .	4
1.2.2 Absorption in molecules . . . . .	5
1.2.3 Fate of excited states . . . . .	6
1.2.4 Semiconductor photophysics . . . . .	10
1.3 Organic photovoltaics . . . . .	14
1.3.1 Historical overview . . . . .	14
1.3.2 Charge generation in OPVs . . . . .	16
1.3.3 Active layer design . . . . .	18
1.3.4 Ultrafast studies in OPVs . . . . .	25

1.4	Perovskite solar cells . . . . .	29
1.4.1	Structural overview . . . . .	29
1.4.2	History in the solar field . . . . .	30
1.4.3	Charge generation and recombination in 3D perovskites . . . . .	31
1.4.4	2D perovskites . . . . .	32
<b>2</b>	<b>Experimental methods</b>	<b>43</b>
2.1	An introduction to laser spectroscopy . . . . .	44
2.2	Transient absorption spectroscopy . . . . .	45
2.2.1	Experimental setup . . . . .	47
2.3	Electroabsorption spectroscopy . . . . .	52
2.4	Time-of-flight . . . . .	55
<b>3</b>	<b>Mechanism of ultrafast intrinsic charge generation in pentamethine cyanine dyes</b>	<b>61</b>
3.1	Introduction . . . . .	62
3.2	Results and discussion . . . . .	64
3.2.1	A comparison between solution and thin film . . . . .	64
3.2.2	The search for oxidised species . . . . .	67
3.2.3	Impact of interchromophore distance . . . . .	68
3.2.4	Changing the counterion . . . . .	71
3.2.5	Charge transport . . . . .	75

3.3	Conclusion . . . . .	79
3.4	Sample preparation and experimental methods . . . . .	80
<b>4</b>	<b>Charge separation processes in squaraine dyes and spiro-OMeTAD</b>	<b>85</b>
4.1	Introduction . . . . .	86
4.2	Results and discussion . . . . .	89
4.2.1	Understanding the transient absorption spectrum . . . . .	90
4.2.2	Investigating the impact of aggregation . . . . .	92
4.2.3	Bilayers with C <sub>60</sub> . . . . .	95
4.2.4	A comparison with the cyanine system . . . . .	97
4.2.5	Spiro-OMeTAD redox photochemistry . . . . .	98
4.3	Conclusion . . . . .	103
4.4	Sample preparation . . . . .	104
<b>5</b>	<b>Photophysics of 2D perovskites</b>	<b>109</b>
5.1	Introduction . . . . .	110
5.2	Results and discussion . . . . .	112
5.2.1	Impact of interlayer distance . . . . .	112
5.2.2	Comparing Dion-Jacobsen and Ruddlesden-Popper perovskites . . . . .	120
5.2.3	Evidencing charge transfer to electroactive spacers . . . . .	122
5.3	Conclusion . . . . .	126
5.4	Sample preparation . . . . .	128

<b>6 Conclusion and outlook</b>	<b>133</b>
<b>Acknowledgements</b>	<b>137</b>
<b>A List of abbreviations and chemical names</b>	<b>141</b>
<b>B Supplementary figures</b>	<b>145</b>

# 1 Introduction



This chapter aims to provide context and scientific background for the research that is presented later in this thesis. The first part will introduce fundamental concepts which will be drawn upon later, whilst the second part will provide some historical context and present the different material systems that will be investigated as well as discussing the current state of the art in these fields.

### 1.1 Why action is needed

The Earth's temperature has been consistently rising by 0.08 °C per decade since 1880 and this rate has more than doubled since 1981 (to 0.18 °C). This rise in temperature has predominantly been caused by an increase in the concentration of greenhouse gases in the atmosphere since the onset of the Industrial Revolution; the concentration of carbon dioxide, methane and nitrous oxide is currently higher than at any time in the past 800,000 years.<sup>1</sup>

Rapid action is required in order to limit warming by 2050 - it is thought that in order to limit global warming to below 1.5 °C, CO<sub>2</sub> emissions resulting from energy systems will have to fall by 87 - 97%. Furthermore, CO<sub>2</sub> emissions from the electricity sector will have to be zero by 2045 - 2055.<sup>2</sup>

The urgent need to reduce greenhouse gas emissions resulting from energy systems is complicated by an increasing global demand for energy - between 2015 and 2019, global energy consumption grew by 6.6% and there was also an accompanying increase in CO<sub>2</sub> emissions during this time frame of 4.6%. It is therefore evident that to be successful in reducing harmful emissions from energy systems, whilst still being able to satisfy the increasing energy demands of the global population, it is necessary to turn to alternative methods of producing energy.<sup>2</sup>

Renewable energy sources, such as solar photovoltaics, wind power and hydroelectric power, alongside other low-carbon methods of electricity generation (e.g. nuclear), are key to ensuring that the global energy demand can be met whilst reducing greenhouse gas emissions. In the past, one issue that hindered the uptake of renewable



energy sources, such as solar photovoltaics, was their high cost; however, the electricity price of solar photovoltaics and wind power dropped by 56 and 45%, respectively, between 2015 and 2020. This has helped increase their uptake, with low-carbon electricity accounting for 37% of global electricity production in 2019.<sup>2</sup>

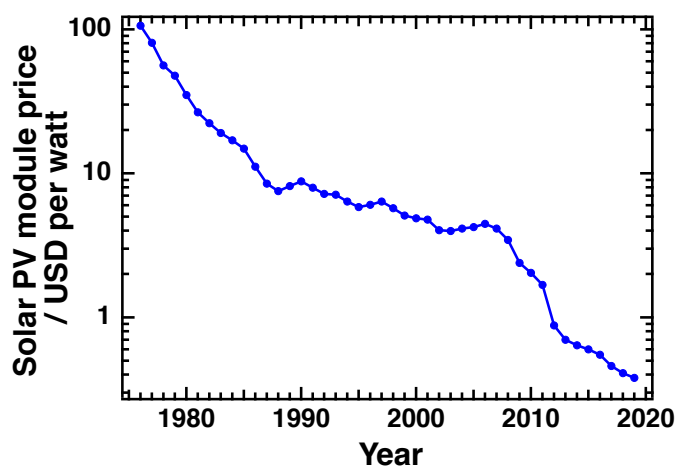


**Figure 1.1:** A graph showing the global average price of solar photovoltaic modules from 1976 to 2019, measured in US dollar (USD) per watt. Prices are shown in 2019 USD.<sup>3,4</sup>

Within the realm of photovoltaics, silicon-based technologies still represent the lion's share of total production (accounting for 95% of total production in 2020).<sup>5</sup> However, in spite of their market dominance, silicon-based photovoltaics are not without issues - the materials can be expensive and there are also environmental issues arising from the manufacturing process, resulting in a long energy payback time. As a result, research into other photovoltaic technologies has continued at a rapid pace.

Third generation materials encompass a wide range of technologies, such as organic photovoltaics, perovskites and dye-sensitised solar cells (DSSCs), and are at the forefront of current photovoltaic research. Whilst different in their material makeup, they are grouped together as they all generate free charges via a donor-acceptor heterojunction, in comparison to first generation silicon solar cells where charges are generated via band bending.

## 1.2 Scientific background

The following section is based on “Physical Chemistry” by Atkins and de Paula, as well as lecture course notes from “Photochemistry I” by Prof. Jacques-E Moser (2021-2022) and “Photochemistry” by Prof. Saif Haque (2015-16).<sup>6-8</sup>

### 1.2.1 Light

The photovoltaic effect was first evidenced by Edmond Becquerel in 1839 and is the basic principle behind photovoltaic devices: light, typically from the sun, is absorbed by a material thus generating a voltage and electric current.<sup>9</sup>

Visible light is a form of electromagnetic radiation formed by electromagnetic waves comprised of oscillating electric and magnetic fields perpendicular to one another and perpendicular to the direction of propagation. The electromagnetic spectrum ranges from radio waves (corresponding to wavelengths greater than 10 m) to gamma and cosmic rays (less than  $10^{-12}$  m). Visible light (typically defined as the wavelength range from 400-700 nm), and indeed any wave, can also be treated as a particle as a result of wave-particle duality. Before this idea was introduced, it had previously been shown by Planck that energy is quantised where the permitted energy of an electromagnetic oscillator can be given by:

$$E = nh\nu \quad (1.1)$$

where  $n$  is a positive integer value,  $h$  is Planck’s constant and  $\nu$  is the frequency.<sup>10</sup>

Given the quantisation of energy, it was proposed that electromagnetic radiation could comprise of particles, known today as photons, with each photon having an energy equal to  $h\nu$ . This was proposed by Albert Einstein in 1905 in order to explain previous experiments on the photoelectric effect.<sup>11</sup>

### 1.2.2 Absorption in molecules

Given that light is composed of photons, it is possible for a molecule to absorb a photon resulting in an electronic transition between different molecular orbitals. Molecular orbitals are formed from a linear combination of the atomic orbitals of which the molecule is composed of. When combined symmetrically, the result is a lower energy bonding molecular orbital which can be filled by two electrons of opposite spin. Similarly, the anti-symmetric combination of atomic orbitals yields high energy anti-bonding molecular orbitals. Organic molecules typically comprise of several different bonding and anti-bonding orbitals; however, the most interesting from a photochemistry perspective are the highest occupied molecular orbital (HOMO) and the lowest unoccupied molecular orbital (LUMO).

In order for a molecule to absorb a photon with a certain frequency,  $\nu$ , the molecule must possess a dipole oscillating at that same frequency. This transition dipole can be expressed as:

$$\mu_{fi} = \langle \Psi_f | \hat{\mu} | \Psi_i \rangle \quad (1.2)$$

where  $\Psi_i$  and  $\Psi_f$  are the wavefunctions of the initial and final states, respectively, and  $\hat{\mu}$  is the electric dipole moment operator.

This can be expanded further to give:

$$\langle \Psi_f | \hat{\mu} | \Psi_i \rangle = \langle \phi_f | \hat{\mu} | \phi_i \rangle \cdot \langle \sigma_f | \sigma_i \rangle \cdot \langle \chi_f | \chi_i \rangle \quad (1.3)$$

where  $\langle \phi_f | \hat{\mu} | \phi_i \rangle$  is the electronic transition dipole moment,  $\langle \sigma_f | \sigma_i \rangle$  the electronic spin overlap integral and  $\langle \chi_f | \chi_i \rangle$  the nuclear wave function overlap integral.

For a transition to be allowed, the transition dipole moment must be non-zero. As a result, there are several selection rules which apply, based on **equation 1.3**:

- $\langle \phi_f | \hat{\mu} | \phi_i \rangle \neq 0$ : The symmetry of occupied orbitals must be conserved during the transition.
- $\langle \sigma_f | \sigma_i \rangle \neq 0$ : The transition should take place between states of the same spin multiplicity (i.e. from a singlet state to a singlet state, or a triplet state to a triplet state). This is to ensure that the magnetic momentum is conserved.
- $\langle \chi_f | \chi_i \rangle \neq 0$ : The probability that a transition takes place is proportional to the square of the nuclear wave function integral.

As a result of the Franck-Condon principle, which states that because nuclei are far more massive than electrons, electronic transitions take place before the nuclei can respond (i.e. the nuclei remain stationary). As electronic states are comprised of several vibrational energy levels, the impact of this is that the intensity of a vertical transition depends upon the overlap of the vibrational wavefunctions.

Experimentally, it was found that the radiation transmitted,  $I$ , through a sample,  $J$ , depends upon the thickness of the sample,  $L$ , and the molar concentration,  $[J]$ , with the following relation:

$$I = I_0 10^{-\epsilon [J] L} \quad (1.4)$$

where  $I_0$  is the incident intensity and  $\epsilon$  is the molar extinction coefficient. This relation is called the Beer-Lambert law, and can be rewritten as follows to give the absorbance,  $A$ , of the sample:

$$A = \epsilon [J] L \quad (1.5)$$

### 1.2.3 Fate of excited states

Once an excited state has been generated following light absorption ( $S_0 \rightarrow S_n$ ), there are several different processes that can take place. These can be broadly grouped into

the following categories: radiative decay processes, non-radiative decay processes and intermolecular electronic energy transfer. Both radiative and non-radiative decay processes can be summarised using a Jablonski diagram (figure 1.2).

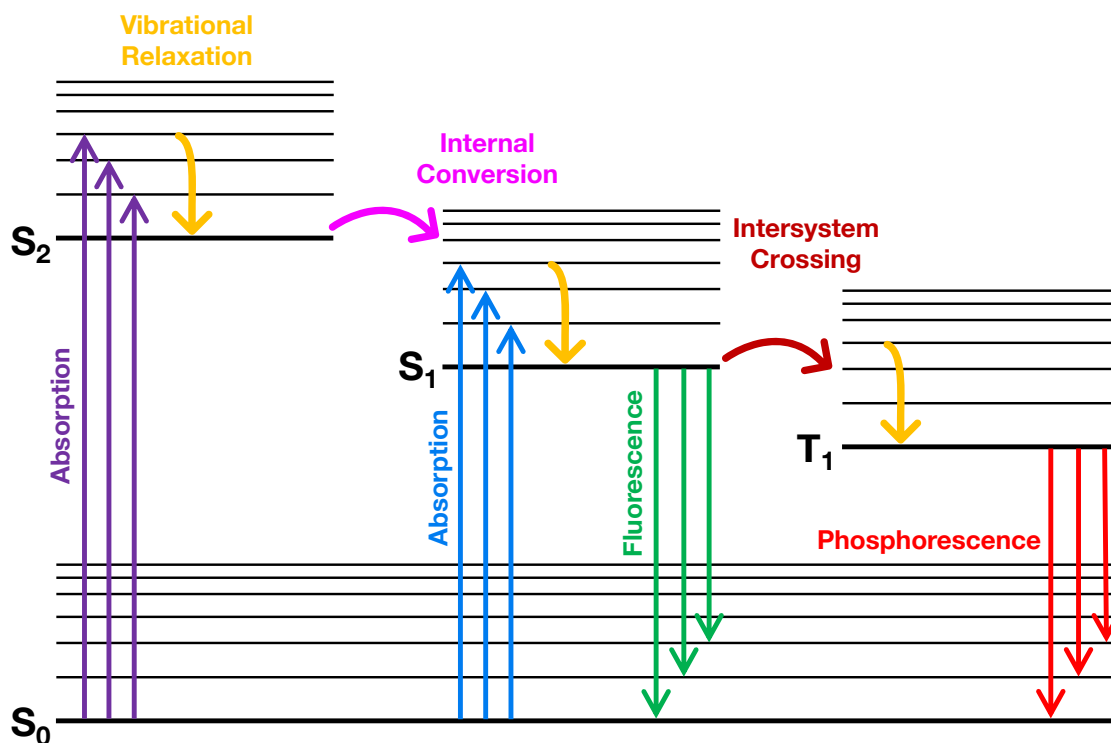


**Figure 1.2:** Jablonski diagram summarising the processes that can occur following light absorption generating an excited state: vibrational relaxation (yellow), internal conversion (pink), intersystem crossing (dark red), fluorescence (green) and phosphorescence (red).

### Non-radiative decay processes

Non-radiative decay processes result in the excess energy in the molecule being transferred to surrounding molecules as heat, rotational, vibrational or translational energy.

One non-radiative decay process that can occur is vibrational relaxation (VR). From the Franck-Condon principle, it is evident that light absorption will result in the

molecule being not only in an excited electronic energy level (e.g.  $S_1$ ) but also in a higher vibrational energy level. VR is the process by which molecules quickly relax to the lowest vibrational energy level within the electronic energy level. This process typically occurs on a picosecond/sub-picosecond timescale.

Another non-radiative decay process that can occur is internal conversion (IC) which is a non-radiative conversion to a state of the same multiplicity. IC takes place most readily at the intersection of the potential energy surfaces of two molecules, as the geometry of the two nuclei is the same at this point. This process occurs on a micro/nanosecond timescale.

A third process that can take place following the generation of an excited state is intersystem crossing (ISC), which is a non-radiative conversion to a state of different multiplicity. ISC can occur when the potential energy surface of the singlet and triplet state of the molecule intersect, followed by a spin-orbit coupling process resulting in the transfer from the singlet to the triplet state (e.g.  $S_1 \rightarrow T_1$ ). As it relies upon spin-orbit coupling, ISC is of particular interest in molecules with heavy atoms due to their larger spin-orbit coupling.

### **Radiative decay processes**

A radiative decay process is where the excess energy following excitation is released as a photon. More commonly termed emission, there are two different types of emission depending on the multiplicity of the emissive state.

Fluorescence is the name given to the radiative decay process occurring between states of the same multiplicity ( $S_n \rightarrow S_0$  or  $T_n \rightarrow T_0$ ). Fluorescence typically occurs on the nanosecond timescale. On the other hand, phosphorescence is the radiative decay process occurring between states of different multiplicity (from triplet states to singlet states). Whilst technically spin-forbidden, spin-orbit coupling allows for the molecule to emit weakly on the millisecond to hundreds of seconds timescale. In accordance with Kasha's rule, both fluorescence and phosphorescence occur from the lowest vibrational

energy level within the higher electronic energy level.

### Intermolecular electronic energy transfer

As well as undergoing the various excited state decay processes mentioned previously, it is also possible for the electronic excitation energy to be transferred from the excited molecule (termed the donor) to a different molecule (termed acceptor). As with excited state decay processes, this energy transfer can take place via radiative or non-radiative mechanisms.

If occurring radiatively, the excited state of the donor molecule decays back to the ground state emitting photons (fluorescence) which can then be subsequently absorbed by the acceptor molecule.

Alternatively, if the process occurs non-radiatively, there are two possible non-radiative intermolecular energy transfer mechanisms that can take place: Dexter energy transfer and Förster resonance energy transfer (FRET). Dexter energy transfer involves the bilateral exchange of electrons between the donor and acceptor molecule. It requires a good overlap of the donor and acceptor wavefunctions in order to occur and, as such, only takes place at short distances (typically less than 10 Å). The rate of Dexter energy transfer is given by the following equation:

$$k_{\text{Dexter}} \propto K \cdot J \cdot \exp\left(\frac{-2R_{\text{DA}}}{L}\right) \quad (1.6)$$

where  $K$  is a constant,  $J$  the spectral overlap integral,  $R_{\text{DA}}$  the distance between the donor and acceptor and finally  $L$  is the sum of the van der Waals radii. Dexter energy transfer conserves the spin multiplicity (i.e. it can take place between two singlet states or two triplet states).

Unlike Dexter energy transfer, FRET occurs at larger distances (typically exceeding the sum of the van der Waals radii of the donor and acceptor). It is caused by a non-radiative coupling between the dipoles of the donor and acceptor which enables the

energy of the excited donor molecule to be transferred to the acceptor. The rate of FRET is given by the following equation:

$$k_{\text{FRET}} = \frac{1}{\tau_D} \left( \frac{R_0}{R_{\text{DA}}} \right)^6 \quad (1.7)$$

where  $\tau_D$  is the radiative lifetime of the donor molecule,  $R_{\text{DA}}$  is once again the donor-acceptor distance and  $R_0$  is the Förster radius, the distance at which the efficiency of energy transfer by FRET is 50%. The value of  $R_0$ , and in turn  $k_{\text{FRET}}$ , is dependent upon the orientation of the two dipoles as well as the spectral overlap between the donor and acceptor, amongst other parameters.

## 1.2.4 Semiconductor photophysics

### Band Structure

A key feature of solids, which determines their electronic properties, is the distribution of electrons into bands.

To understand the origin of this band structure, we can take an example of a simple one dimensional solid consisting of atoms with one s orbital available for the formation of molecular orbitals. With two atoms, the orbitals overlap to form one bonding and one antibonding orbital. If a third atom is added, three orbitals are formed. As the number of atoms becomes infinitely large, the separation between neighbouring levels becomes infinitely small and, importantly, the resulting band has a finite width.

As well as being formed from s orbitals, a band can also be formed from other orbitals, such as p orbitals (yielding a p-band). If there is a difference in energy between the s and the p orbitals, then the s and p bands will be at different energies separated by a bandgap,  $E_g$ . The highest occupied energy band is known as the valence band whilst the lowest empty, or partially filled, band is known as the conduction band.



**Insulators, conductors and semiconductors**

An insulator is a material whereby the valence band is completely filled whilst the conduction band is empty, and the two bands are separated by a large bandgap. This large bandgap means that few electrons can be promoted from the valence band to the conduction band at regular temperatures, and so the conductivity remains close to zero.

On the other hand, conductors are materials where either the valence band and conduction band overlap, or the conduction band is partially filled. As such, they are able to transport charge. The conductivity of such a material decreases with increasing temperature, in spite of the fact that as the temperature increases more electrons are excited into the conduction band. This can be explained by an increase in atomic motion with increasing temperature, leading to a higher number of collisions between the conducting electrons and the atoms.

A third class of materials are semiconductors. These are insulating materials (with a complete valence band and empty/partially empty conduction band) which can become conductive under certain conditions via the promotion of electrons from the valence band to the conduction band. Unlike metallic conductors, the conductivity of semiconductors increases with increasing temperature.

There are different ways in which an electron can be promoted from the valence band to the conduction band. If  $E_g < 3k_B T$  then electrons can be promoted thermally across the bandgap, resulting in a negatively charged electron in the conduction band and a positively charged hole in the valence band. In this case, both the electron and hole contribute to the conductivity. Furthermore, the absorption of photons with energy greater than or equal to the bandgap can also result in the promotion of electrons into the conduction band.

Semiconductors can then be further subdivided into two categories: intrinsic and extrinsic semiconductors. Intrinsic semiconductor is the name given to materials where the conduction is a property of the material itself as a result of its band structure.

Examples of intrinsic semiconductors include silicon and CdS. Conversely, extrinsic semiconductors are materials whereby the charge carriers are present as a result of chemical doping.

The doping material can have fewer valence electrons than the semiconductor it is doping, and so can form a narrow band above the semiconductor valence band which can accept electrons; the resulting holes in the semiconductor are mobile giving rise to the conductivity. This is called p-type semiconductivity, as the holes are positive relative to the rest of the electrons in the band. Likewise, it is also possible for the dopant to have more valence electrons than the semiconductor it is doping, allowing it to form a narrow band which can donate electrons into the conduction band. This is called n-type semiconductivity, and the two types (p and n) can be seen in **figure 1.3**.

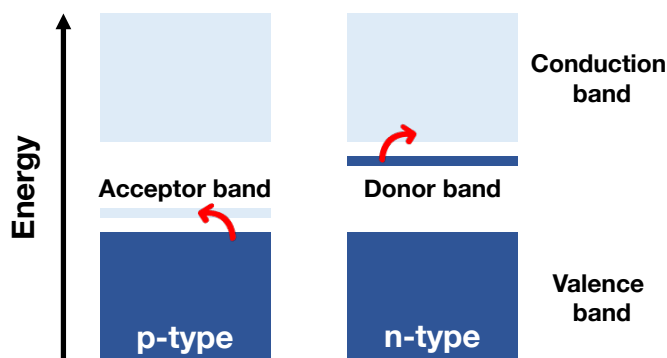


**Figure 1.3:** Diagram showing the energy levels of electron acceptors and electron donors resulting in p- and n-type doping. The red arrows show the movement of electrons.

### Direct and indirect transitions

The band structure of materials is often represented as a graph detailing how the energy of the states change in relation to the crystal momentum which can be characterised by a wave vector,  $k$ . In an ideal system, the energy bands would appear as a series of parabolas with the following equation:

$$E = \frac{\hbar^2 \cdot k^2}{2m_e^*} \text{ where } k = \frac{2\pi \cdot p}{h} \quad (1.8)$$

where  $k$  is the previously mentioned wave vector and  $m_e^*$  is the reduced electron mass. In reality, however, the band structure of a material is more complex as a result of the reduced mass not being the same in all directions.

The transitions that occur between the valence and conduction bands can be differentiated based on whether there is a change in  $k$ . A direct electronic transition takes place when the valence band maximum and conduction band minimum have the same  $k$  value. As such, the transition follows the Franck-Condon principle. This can be seen visually in **figure 1.4**.

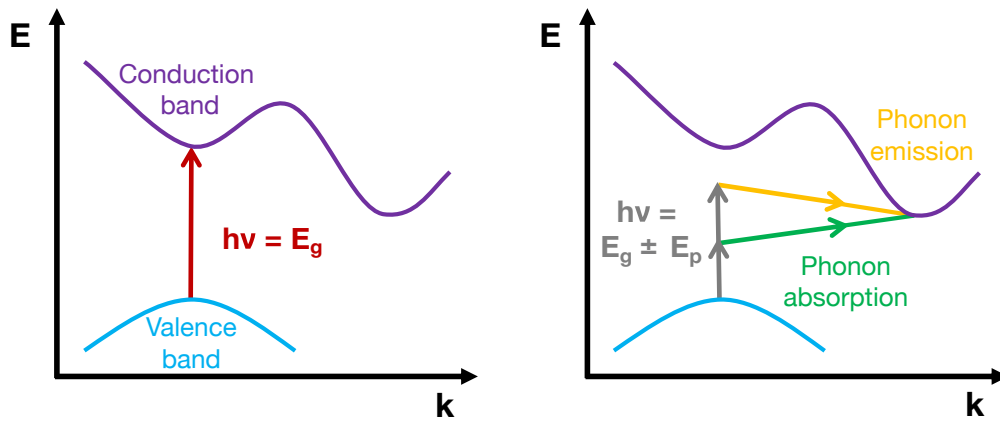


**Figure 1.4:** Direct (left) and indirect (right) electronic transitions in semiconductors between the valence and conduction bands. For direct transitions, the energy of the incoming photon should be equal to the bandgap ( $h\nu = E_g$ ). For indirect transitions, the photon energy is equal to the bandgap plus or minus the energy of a phonon ( $h\nu = E_g \pm E_p$ ).

An indirect transition, on the other hand, occurs in a scenario where the valence band maximum and conduction band minimum have different  $k$  values and the electronic transition between them is coupled with a vibration in the solid lattice. As photons themselves possess a negligible momentum, the change in momentum arises from the absorption or emission of a phonon with energy  $E_p$ . A phonon is a type of quasi-particle and consists of a quantised microscopic vibration in a crystal lattice.

## 1.3 Organic photovoltaics

Having covered the requisite scientific background, this section introduces organic photovoltaics (OPVs). It includes historical milestones within the field and the operational mechanism of OPVs, before covering OPV materials in depth as well as detailing ultrafast studies in the field.

### 1.3.1 Historical overview

The first report of photoconductivity in an organic system came from Pochettino in 1906, where he evidenced photoconductivity in anthracene<sup>12</sup>; however, it wasn't until 1958 that the photovoltaic effect was demonstrated in an organic material.<sup>13</sup> Here, magnesium phthalocyanine (MgPc) discs were coated with a thin film of tetramethyl-*p*-phenylenediamine (TMD) giving a photovoltage of 200 mV. Given the positive potential of the MgPc relative to the TMD layer, it was thought that electron transfer took place from the MgPc discs to the TMD layer.

Around this time, phthalocyanines were widely studied because of their facile preparation, ease of forming crystalline thin films by vacuum sublimation and their strong absorption in the visible region.<sup>14</sup> Later studies on MgPc revealed that the photovoltaic properties of the MgPc layer were highly dependent upon the degree of exposure to oxygen.<sup>15</sup>

Throughout the 1970's, other single layer dye-based devices were studied although the power conversion efficiencies (PCEs) of these systems were typically very small (less than 0.1 %). Their efficiency was often dependent upon the electrode composition and they also suffered from poor fill factors (FF), a measure of a solar cell which is the ratio of the maximum obtained power to the product of the open circuit voltage and short circuit current.

A key breakthrough came in 1986 with the advent of the planar heterojunction, which combined two materials in the active layer.<sup>16</sup> The idea was that one material

would act as the electron donor and the other as the acceptor, with the two materials having mismatched energy levels. As such, there was therefore a driving force for charge separation to occur. By combining copper phthalocyanine with a perylene tetracarboxylic derivative layer, a device efficiency of 0.95% with a fill factor of 0.65 was achieved, a vast improvement over single layer devices of the same era.

However, these planar heterojunctions, whilst better than single layer devices, still had some issues which centred on the low exciton diffusion length in organic materials (5 - 10 nm). This short diffusion length meant that any excitons that were formed far from the donor-acceptor (D/A) interface would undergo recombination before being able to migrate to the interface where separation occurs. An exciton is the name given to a localised excited state comprised of a coulombically bound electron-hole pair. One strategy to overcome this was to fabricate devices with a very thin active layer (typically 10's of nm), as this would result in a higher proportion of excitons being generated within a diffusion length of the D/A interface. Unfortunately, it was typically the case that the thickness required to satisfy this condition was below the optical absorption depth of the material, and so photon absorption was dramatically reduced.

One idea, that came about in 1990, was to fabricate an interlayer within the active layer consisting of a co-deposited donor and acceptor material (thus creating a donor/interlayer/acceptor active layer structure). The result was an increase in the photocarrier generation efficiency.<sup>17</sup>

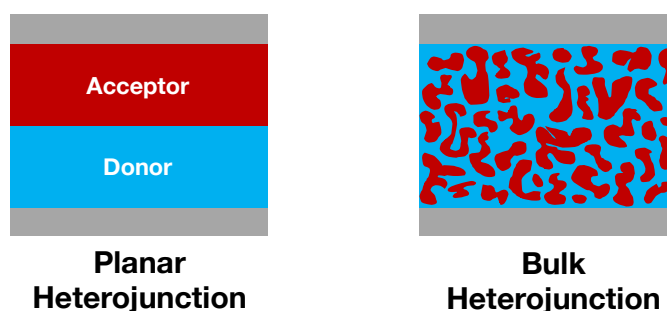


**Figure 1.5:** A comparison of the planar heterojunction and bulk heterojunction OPV architectures.

This concept was further developed in 1995 into a new OPV architecture termed bulk heterojunction (BHJ).<sup>18,19</sup> The BHJ architecture consisted of an interpenetrating network of donor and acceptor composites, leading to a vast increase in the D/A interfacial area. The result was that more excitons could be generated within an exciton diffusion length of the interface, thereby leading to less recombination and an increased device efficiency. A schematic of the bulk heterojunction active layer morphology, in comparison to a planar heterojunction, can be seen in **figure 1.5**.

### 1.3.2 Charge generation in OPVs

To gain an appreciation for the benefits of the BHJ architecture, as well as recognise why a D/A heterojunction is needed in the first place, it is important to understand the mechanism of charge generation in OPVs.

The charge generation mechanism in OPVs can be divided into four key processes: exciton generation, exciton diffusion, charge separation and finally charge collection. It is the efficiency of these processes that go a long way in determining the overall efficiency of the device itself. These four processes are shown pictorially in **figure 1.6** and are described below.

Exciton generation proceeds via the absorption of a photon by either the donor or acceptor material which generates an exciton. An exciton is the name given to a coulombically bound electron hole pair, and if generated within the donor material it is known as channel I excitation, whilst generation of the exciton in the acceptor is termed channel II excitation. The molar extinction coefficient,  $\epsilon$ , of the absorbing material governs the efficiency of photon absorption and, therefore, exciton generation.

Excitons can be classified into two main categories differentiated by their binding energy. The first of these, Wannier-Mott excitons, are weakly bound and are typically found in inorganic semiconductors. The high dielectric constant of the material leads to an increase in the charge screening of the carriers by the lattice thus resulting in their low binding energy. As a result of their low binding energy, Wannier-Mott excitons can

readily dissociate into free charges.

The second type of excitons, called Frenkel excitons, are comprised of tightly bound electron-hole pairs and are typically generated within organic semiconductors due to their low dielectric constants. Due to their high binding energy, which greatly exceeds thermal energy at room temperature, a charge separation process is required to form free charges.

Once the Frenkel excitons have been formed in the active layer, they can then undergo diffusion to the D/A interface. As mentioned in the previous section, the introduction of the BHJ active layer architecture greatly helped in increasing the efficiency of this diffusion process.

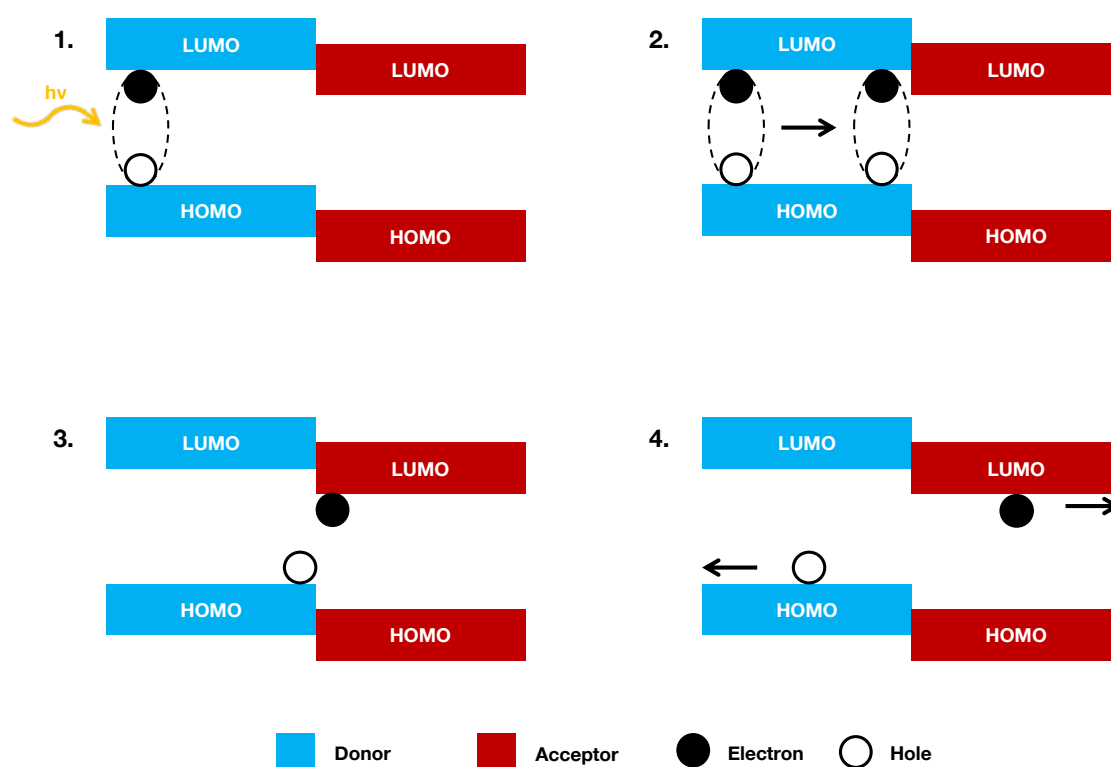


**Figure 1.6:** A pictorial representation of the charge generation mechanism in OPVs following donor (channel I) photoexcitation. 1) Photon absorption and exciton generation, 2) exciton diffusion to the D/A interface, 3) separation of the exciton into free charges and 4) charge transport and subsequent collection at the electrodes.

Charge separation then takes place at the D/A interface with the exciton separating into an electron and hole. The driving force for charge separation ( $\Delta E_{CS}$ ) arises from differences in the HOMO and LUMO energy level of the donor and acceptor material, and can be summarised with the following equation:

$$\Delta E_{CS} = (IP_D - EA_A) - E_{ex} \quad (1.9)$$

where  $IP_D$  and  $EA_A$  are the ionisation potential and electron affinity of the donor and acceptor material, respectively, and  $E_{ex}$  is the exciton binding energy.

Having undergone separation, it is possible for the electron and hole to form a charge transfer (CT) exciton, due to the coulombic attraction between the two charges. This is a concept that will be explored in further detail in **section 1.3.4**.

The efficiency of the charge separation process is governed, primarily, by the energy level offset between the donor and acceptor material. However, charge separation is still possible in devices where there is minimal offset.

Finally, the free charges can then be collected at the electrodes, a process which can be hampered by non-geminate recombination. This is a process whereby free electrons and holes recombine, emitting photons. Non-geminate recombination is particularly prevalent in materials where there is no charge percolation pathway present in the material.

### 1.3.3 Active layer design

Research in the field of organic photovoltaics can be split into a few key areas including, but not limited to, material design, morphology optimisation and fundamental mechanistic studies. It is a combination of advances within these areas that have led to device efficiencies improving from around 2.9% in 1995 to well over 18% today.<sup>20</sup>

Organic solar cells typically comprise of several layers each performing a particular role to ensure that the PCE is maximised. A basic structure of an OPV device is shown



in **figure 1.7**. The principal component of an organic solar cell is the active layer which, as already discussed, is where light is absorbed and free charges are generated. Either side of this active layer are interlayer materials which selectively transport electrons or holes. Finally, the device is sandwiched between two electrodes one of which is transparent (typically a transparent conductive oxide such as indium-doped tin oxide, ITO), whilst the other is an evaporated metal contact (e.g. aluminium or silver).

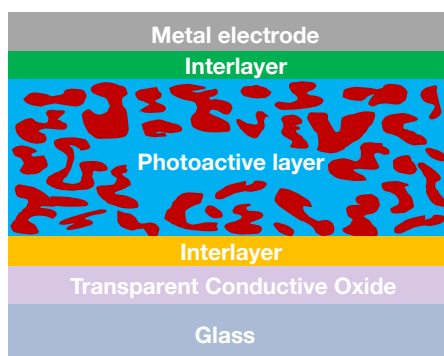


**Figure 1.7:** Schematic of the device structure in an organic photovoltaic device.

As well as being able to have several different architectures, the active layer can also be comprised of different donor and acceptor materials such as conjugated polymers, fullerene acceptors and small molecule donors. This section will introduce key research areas related to active layer donor and acceptor materials.

### Conjugated polymers

The majority of donor materials used within active layers in OPVs fall into the category of conjugated polymers. These are polymers with a backbone consisting of alternating single and double bonds. The p-orbitals on neighbouring atoms overlap, creating a system where electrons can be delocalised across the entire backbone of the molecule. The development of conjugated polymers began in the 1970's, and work done on developing a highly conductive iodine-doped polyacetylene polymer was awarded the Nobel prize in the year 2000.<sup>21</sup>

Whilst first utilised in OPVs in 1984, it took the invention of the BHJ as well as the observation of ultrafast charge transfer between conjugated polymers and C<sub>60</sub> for their usage to become widespread.<sup>22</sup> Initially, poly(*p*-phenylenevinylene) derivatives were used, with efficiencies of 2.50% being achieved.<sup>23</sup> However, polythiophene derived polymers such as poly(3-hexylthiophene), commonly known as P3HT, quickly became the material of choice thanks to their extensive  $\pi$ -electron delocalisation and high thermal stability.<sup>24</sup> Furthermore, P3HT can be synthesised on large scales, making it a suitable candidate for commercial OPV devices.<sup>25</sup>

Often used alongside fullerene-based electron acceptor materials, such as [6,6]-phenyl-C<sub>61</sub>-butyric acid methyl ester (PC<sub>61</sub>BM), device efficiencies increased from around 0.6% to over 7%.<sup>26</sup> However issues with P3HT, such as its mismatched absorption and high-lying HOMO energy level, limit the efficiency of P3HT/fullerene devices. Due to these issues, attention has more recently been focused on low bandgap donor-acceptor (D-A) type polymers.

D-A type polymers consist of alternating electron rich and electron deficient moieties, which allow for greater tuneability of the absorption profile, energy levels and transport properties. The lower bandgap originates from electron delocalisation across the backbone as well as the hybridisation of frontier orbitals.<sup>27</sup> A variety of different moieties have been used to great success: for example, polymers based on thieno[3,4-b]thiophene and diketopyrrolopyrrole (DPP) units such as PTB7-Th and PBDTTT-SeDPP have achieved efficiencies of 10.6 and 7.2%, respectively, when combined with PC<sub>71</sub>BM.<sup>28,29</sup> Since the introduction of small molecule non-fullerene acceptors, conjugated polymers based on benzothiophene repeating units, such as PBQx-TF and PM6, have been used to achieve PCEs of over 17%.<sup>20,30</sup>

Whilst able to achieve high PCEs, conjugated polymer donor materials are not without issues; they are often difficult and costly to synthesise. Furthermore, their synthesis often produces toxic metallic by-products and so, at the current time, they are not viable candidates for commercialisation.

These problems can be mitigated through the use of small molecule electron donors.

These materials have a well defined structure and their properties exhibit no dependence on the molecular weight resulting in better synthetic reproducibility when compared to conjugated polymers. Small molecule electron donors encompass a wide variety of materials ranging from pentacene derivatives<sup>31</sup> to oligothiophenes,<sup>32</sup> and they have been used extensively in the OPV field since merocyanine was first used in 1978.<sup>33</sup>

### Small molecule donors - cyanine dyes

Cyanine dyes, introduced here as they will be the focus of the third chapter of this thesis, consist of a cationic chromophore paired with a counterion. They have been used extensively in a variety of fields including as biomarkers,<sup>34</sup> in the photographic industry,<sup>35</sup> in OPVs and in light emitting electrochemical cells.<sup>36</sup> The characteristic structure of a cyanine chromophore is two nitrogen atoms linked with a polymethine chain. In the OPV field, it is typical for the nitrogen atoms to be part of a heterocycle, an example of which is shown in **figure 1.8**.

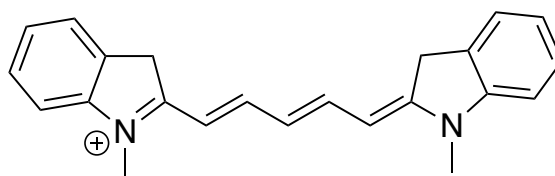


**Figure 1.8:** An example of a cyanine chromophore.

Although photoconductivity was first evidenced in cyanine thin films in 1956,<sup>37</sup> their first widespread usage in the field of photovoltaics was in DSSCs. They proved to be effective sensitisers thanks to their high molar extinction coefficients (typically exceeding  $100,000 \text{ L mol}^{-1} \text{ cm}^{-1}$ )<sup>38</sup> allowing the short circuit photocurrent to exceed that of devices sensitised with ruthenium complexes.<sup>39</sup>

Furthermore, cyanine dyes are solution processable which led to them being used as small molecule donors in OPVs alongside fullerene acceptors. In this case, their high extinction coefficients meant that they could successfully be used in planar architecture devices, as the active layer could be very thin (around 20 nm) whilst maintaining a high

photon absorption thus overcoming the issue of excitons being generated too far from the D/A interface.

Another benefit of cyanine dyes is that it is facile to tune their absorption spectrum. This can be done by functionalising the heterocycles or the polymethine chain itself. The latter is a technique which has been used extensively to shift the absorption spectrum into the near-IR for use in transparent OPVs, with efficiencies of such devices reaching 2.2%.<sup>40</sup>

An alternative method of changing the properties of the cyanine dye involves changing the counterion, which is done using an ion exchange column. The synthesis of cyanine dyes often results in the counterion being a halide ion, such as  $\text{Cl}^-$  or  $\text{I}^-$ , which often have a negative impact on redox stability and charge delocalisation. By exchanging these anions for ones where the negative charge can be delocalised across several atoms, such as bistriflimide, it is possible to increase the OPV performance.<sup>41</sup> This concept has been further explored by employing ‘super weak’ coordinating anions such as tetrakis(nonafluoro-tert-butoxy)aluminate, where the size of the anion results in highly amorphous thin films and excited state stabilisation yielding improved device performance.<sup>42</sup>

Cyanine dyes have also more recently been explored as suitable materials for use in tandem OPVs,<sup>43</sup> as well as being used to form hybrid organic-inorganic solar cells via co-sensitisation by CdTe/CdS quantum dots.<sup>44</sup> Furthermore, they have also been incorporated into hybrid organic-inorganic perovskites.<sup>45</sup>

### **Small molecule donors - squaraine dyes**

The second class of donor materials that will be focused on in this thesis are squaraine dyes. They were first synthesised in 1965<sup>46</sup> and comprise of an electron deficient squaryl ring flanked either side by donor aromatic/heterocyclic rings resulting in a zwitterionic structure. Like cyanine dyes, they have several advantageous properties which make them promising candidates for OPVs. For example, they have high

molar extinction coefficients and so the active layer can be thin and their bandgap can be easily tuned via molecular design to ensure a good match with acceptor materials. Furthermore, they can be synthesised easily without the need for expensive metal catalysts.<sup>47</sup>

Squaraine dyes were first used as an active layer material in OPVs in 1976, where one was sandwiched between an  $\text{In}_2\text{O}_3$  and a metallic Ga electrode yielding a PCE of 0.02%.<sup>48</sup> Whilst efficiencies of early squaraine devices left a lot to be desired, they were still exploited to good effect in DSSCs as a result of their high extinction coefficients.<sup>49</sup>

Efficiencies of squaraine-based OPVs finally breached the 1% barrier in 2008,<sup>50</sup> and further optimisation and material design led to huge PCE increases up to 3.2% in 2009<sup>51</sup> and 5.2% in 2011<sup>52</sup> for planar heterojunction devices. Subsequent incorporation into tandem OPVs has seen device efficiencies breach over 8%.<sup>53</sup> Currently, the poor mobility in squaraine dyes is seen as the primary limiting factor to their device performance in BHJ architecture devices. It is thought that by optimising the active layer morphology, as well as the molecular ordering, the carrier mobility could improve thus minimising charge recombination leading to an increase in device efficiencies.

Outside of the OPV field, squaraine dyes have recently attracted attention for use in short-wave infrared (SWIR) photodetectors. Nucleophilic substitution of a dicyanomethylene group resulted in the synthesis of dicyanomethylene squaraine (DCSQ) dyes, allowing for the absorption to be shifted into the SWIR region. Typical SWIR photodetectors are based on InGaAs and so are too expensive for low cost applications, and so the incorporation of SQ-based active layers into SWIR photodetectors remains an attractive possibility.<sup>54,55</sup>

### Fullerene acceptors

Fullerene-based electron acceptors, such as  $\text{PC}_{61}\text{BM}$  and  $\text{PC}_{71}\text{BM}$ , have been used extensively as acceptor materials in the OPV field since the 1990's. They became the go-to acceptor material in this time period due to several advantageous properties such

as (i) possessing a LUMO delocalised across the whole molecule allowing for efficient charge separation and transport in three dimensions, (ii) high electron mobilities, (iii) the ability to undergo multiple (reversible) reduction events and (iv) their ability to form aggregates which form both pure and intermixed domains leading to a suitable charge percolation pathway.<sup>56</sup>

Whilst competitive efficiencies (over 12% in a BHJ with two polymer donors)<sup>57</sup> have been achieved using PCBM, there are issues with stability as PCBM can aggregate with thermal ageing which disrupts the charge percolation pathway thus causing a reduction in the PCE.<sup>58</sup> Furthermore, it is difficult to tune their electronic and structural properties. These issues have been alleviated, in part, by the development of other fullerene-based acceptors such as indene-C<sub>60</sub> bisadduct (ICBA), which possesses a stronger absorption than PC<sub>71</sub>BM in the visible region, as well as a higher LUMO energy level; when combined with P3HT, ICBA gave a higher PCE than comparable PC<sub>71</sub>BM devices.<sup>59</sup>

### Non-fullerene acceptors

Given the aforementioned disadvantages of fullerene-based acceptors, research into non-fullerene acceptors (NFAs) has exploded in recent years. A wide variety of different NFAs have been used, including in the first planar heterojunction in 1986<sup>16</sup>; however, the majority of recent work in the NFA field has focused on fused ring electron acceptors.<sup>60</sup>

Fused ring electron acceptors consist of two electron withdrawing moieties either side of a fused ring core resulting in an A-D-A structure. By modifying the core itself, as well as the two withdrawing groups, it is possible to tune the properties of the acceptor to achieve a good energy level match with donor materials. The most well known fused ring electron acceptor, ITIC,<sup>61</sup> is based on an indacenodithienothiophene core which has since been modified to yield devices with a PCE of over 12%.<sup>62</sup> Other more elaborate acceptors have since been synthesised pushing the device efficiency to over 18%.<sup>30</sup>

### 1.3.4 Ultrafast studies in OPVs

Ultrafast charge transfer was first evidenced in OPV materials in 1992; spin resonance studies demonstrated that photoinduced electron transfer was occurring between a conducting polymer and  $C_{60}$ .<sup>63</sup> Although unable to precisely determine the timescale of the charge transfer process, it was thought to occur on a sub-picosecond timescale. This was confirmed in 2001 using transient absorption spectroscopy, where it was found that the photoinduced electron transfer took place in 45 fs.<sup>64</sup>

As mentioned in **section 1.3.2**, excitons are generated following photon absorption and can undergo separation at the D/A interface. Following this separation it is possible for charge transfer excitons (CTEs) to form, due to the coulombic attraction between the electron and hole. As CTEs are formed at junctions/interfaces within a system, they can also be termed interfacial CTEs. The dissociation of CTEs is a key step in the charge generation process in OPVs and, as such, it is a topic that has been studied extensively in recent years.

As CTEs are lower in energy when compared to excitons, hot CTEs are often formed; however, the fate of these hot CTEs is still debated. Some studies have shown that direct dissociation of hot CTEs can occur before the CTE can relax to the ground state.<sup>65,66</sup> Further studies have demonstrated that excess energy can result in an increase in charge carrier generation, implying that the excess energy can provide the driving force for CTE dissociation.<sup>67–69</sup> On the other hand, studies on high performance blends showed that the yield of free charge carriers was not dependent on the excitation energy, implying that CTE dissociation must occur via a different mechanism.<sup>70,71</sup> It is thought that CTE delocalisation is dependent upon the blend morphology, charge delocalisation and donor/acceptor energetics.

### Cyanine and squaraine based OPVs

Historically, research involving the study of ultrafast processes in cyanine dyes has focused on the photophysics of cyanine in solution, in particular examining the triplet

state characteristics<sup>72</sup> as well as the dynamics of excited states.<sup>73</sup>

Within the realm of photovoltaics, studies have focused on cyanine/C<sub>60</sub> bilayers as model systems for studying CTE dissociation given their simpler device architecture. Time resolved electroabsorption measurements were used to show that interfacial CTEs dissociated into free charge carriers in tens to hundreds of picoseconds.<sup>74</sup> These measurements were based on the Stark effect, which is where electronic transitions are influenced by an electric field causing a measurable shift in the absorption spectrum. The origin of the Stark effect will be explained fully in the following chapter. Blend morphology has also been studied in cyanine-based OPVs, where it was found that the phase morphology in cyanine/PCBM blends had a large impact on the efficiency of photoinduced charge separation.<sup>75</sup>

Similar to studies done on cyanine dyes, research into squaraine dyes has focused upon the excited state photophysics and exploring their fluorescence.<sup>76,77</sup> However, comparatively little work has focused on ultrafast charge generation in squaraine-based OPVs. Studies which have been done tend to focus on squaraine/PCBM blends, where it has been shown that CT states are formed with a lifetime of 550 ps.<sup>78</sup>

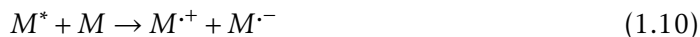
### **Symmetry-breaking charge separation**

Symmetry-breaking charge separation (SB-CS) is a process which results in the separation of charges following excitation of a chromophore, M, yielding oxidised and reduced species. SB-CS processes can be broadly grouped into two classes depending on the system. The first class relates to M-Q<sub>n</sub> systems, whereby Q is a quencher, and involves a charge transfer between the chromophore and the quencher. The second class, on the other hand, involves charge separation between two identical chromophores. It is also possible to further differentiate SB-CS processes into those that are intramolecular and those that are intermolecular.<sup>79</sup> The remainder of this section will be focused on intermolecular SB-CS between identical chromophores.

Intermolecular SB-CS can proceed via one of two mechanisms involving either the



excitation of both reactant chromophores, or just one of the chromophores:



In the first scenario, the photoexcited molecule is electronically coupled to the neighbouring chromophore allowing the charge transfer to take place. At first glance, it appears that SB-CS would be unfavourable as it is often the case that the energy levels of the  $M + M^*$  and  $M^{\cdot+} + M^{\cdot-}$  are very similar and so it is difficult to see where the thermodynamic driving force for such a process would come from. However, in reality, the solvation of the chromophores and electrostatic interactions help play a role in providing the driving force for SB-CS. As such, SB-CS is a process that has been studied in great depth in solution, in particular in the presence of polar solvents where the polar solvent helps to stabilise the CT state, thus making it more thermodynamically accessible.<sup>80</sup> The free energy change for SB-CS,  $\Delta G_{CS}$ , is given by the Weller formulation<sup>81,82</sup>:

$$\Delta G_{CS} = e[E_{ox} - E_{red}] - E_{00} + C + S \quad (1.12)$$

where  $e$  is the electronic charge,  $E_{ox}$  and  $E_{red}$  are the half wave potentials for a one-electron oxidation or reduction of the donor or acceptor, respectively,  $E_{00}$  is the energy of the singlet excited state,  $C$  is the coulombic interaction between the two ions and finally  $S$  is the solvation energies of the ions.

In spite of SB-CS being generally unfavourable in non-polar environments and the solid state, it has been evidenced in both cases. For example, SB-CS has been observed in 1,6,7,12-tetra(phenoxy)-perylene-3,4:9,10-bis(dicarboximide) (tpPDI) cyclophanes in toluene where it is thought that the quadrupole moment of the toluene helps to stabilise the charge transfer state.<sup>83</sup> Similarly, the extensive  $\pi$ -conjugation in rylene diimide systems leads to them having an appreciable quadrupolar character which also helps to stabilise the CT state making it more thermodynamically accessible.<sup>84</sup>

Recently, SB-CS has become an attractive research topic in the OPV field as a way of improving device efficiencies. OPVs are often limited by poor open circuit voltages ( $V_{OC}$ ) which directly impacts upon the device efficiency. The  $V_{OC}$  is related to the difference in energy between the HOMO of the donor material and the LUMO of the acceptor material (**figure 1.9**), and theoretically is maximised when the LUMO of the donor and acceptor materials are the same. However, in this scenario, there would be no driving force for charge separation, and so it would lead to a reduced proportion of free charge carriers being generated as charge separation would struggle to compete against exciton recombination. Therefore, a SB-CS process would provide a way for charge separation to occur whilst maximising the  $V_{OC}$ .

One example of this has been the use of zinc chlorodipyrin as an acceptor alongside tetraphenyldibenzoperylanthrene (DBP). The inclusion of zinc chlorodipyrin, which can undergo SB-CS, resulted in a  $V_{OC}$  increase of 0.45 V when compared to analogous DBP/ $C_{60}$  devices (from 0.88 to 1.33 V), a difference which was ascribed to the ability of the zinc chlorodipyrin to undergo SB-CS.<sup>85</sup>

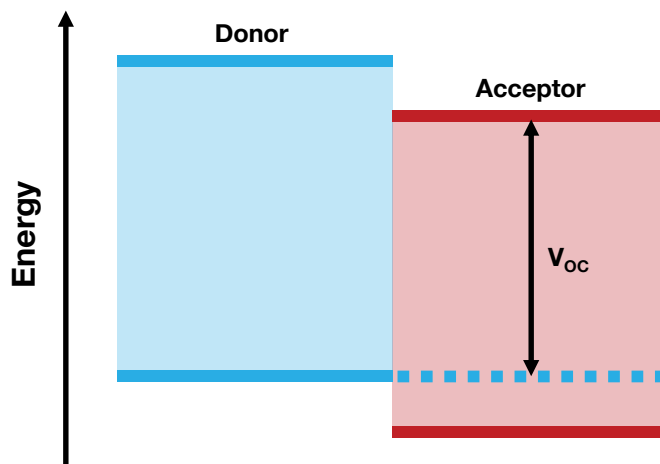


**Figure 1.9:** Schematic showing how the open circuit voltage is related to the difference in HOMO and LUMO energy levels of the donor and acceptor material.

## 1.4 Perovskite solar cells

The final part of the introduction is focused on perovskite solar cells, a material system which will be the focus of the final results chapter.

### 1.4.1 Structural overview

Originally the name of the mineral calcium titanate ( $\text{CaTiO}_3$ ), perovskite is now used to refer to a material with the same  $\text{ABX}_3$  structure where A is a large monovalent cation, B is a divalent metal cation and X is an anion. A wide variety of elements can be combined to form a perovskite structure given they exhibit a suitable Goldschmidt tolerance factor,  $t$ , which can be calculated with the following equation:

$$t = \frac{R_A + R_X}{\sqrt{2}(R_B + R_X)} \quad (1.13)$$

where  $R_A$ ,  $R_B$  and  $R_X$  are the ionic radii of A, B and X, respectively. For example, halide perovskites can be formed if  $t$  is between 0.81 and 1.11.<sup>86</sup>

As well as large elemental cations, such as  $\text{Ca}^+$ , the perovskite structure can also accommodate organic cations such as methylammonium,  $\text{MA}^+$  ( $\text{CH}_3\text{NH}_3^+$ ), or formamidine,  $\text{FA}^+$  ( $\text{HC}((\text{NH})_2)_2^+$ ).

When referring to perovskite solar cells, lead halide perovskites are usually the materials in question, with  $\text{MAPbI}_3$  being the most well known.  $\text{MAPbI}_3$  typically has a tetragonal structure at room temperature, and can undergo phase changes to a cubic structure at higher temperatures (above 330 K, **figure 1.10**) or an orthorhombic phase at lower temperatures (below 160 K).<sup>87</sup> The structure is important, as it can impact upon the optical and electronic properties of the perovskite.

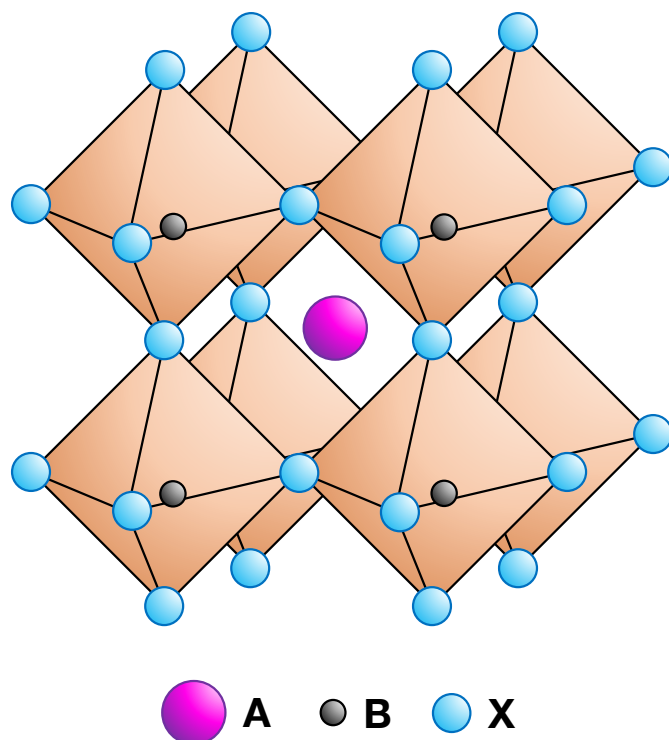


**Figure 1.10:** Cubic perovskite structure typically seen in MAPbI<sub>3</sub> at temperatures above 330 K.

#### 1.4.2 History in the solar field

Despite the discovery of MAPbI<sub>3</sub> taking place in 1978,<sup>88</sup> it wasn't until 2009 that it was first used in the solar field, being employed as a sensitiser in DSSCs yielding a modest PCE of 3.8%.<sup>89</sup> Subsequent improvements in the efficiency were made, reaching 6.5% in 2011.<sup>90</sup> However, issues arose with the perovskite that was adsorbed onto the TiO<sub>2</sub> surface undergoing dissolution into the liquid electrolyte. This issue was overcome by replacing the liquid electrolyte with 2,2',7,7'-tetrakis (N,N-di(4-methoxyphenylamine)-9,9'-spirobifluorene (spiro-OMeTAD), a solid state hole conducting material. The result was a solid-state device which was far more stable than its liquid electrolyte based counterpart with an efficiency of 9.7%.<sup>91</sup> Soon after, a PCE of 10.9% was achieved by replacing the mesoporous TiO<sub>2</sub> with mesoporous Al<sub>2</sub>O<sub>3</sub>.<sup>92</sup>

Given their high efficiencies, already surpassing that of solid state DSSCs, as well as

their facile preparation, research in the field of hybrid organic lead halide perovskites exploded. Through a combination of compositional tuning, the development of new processing techniques, interface engineering and defect passivation the efficiency of perovskite solar cells has reached over 25%, thus emerging as one of the most promising materials to challenge silicon-based solar cells.<sup>93</sup>

### 1.4.3 Charge generation and recombination in 3D perovskites

One of the main reasons behind the high efficiency of lead halide perovskites is their strong optical absorption due to their high molar extinction coefficients as well as them being direct bandgap semiconductors. The bandgap can also be tuned by changing the halide used, going from 1.65 eV when using iodide to 3.15 eV when using chloride in MAPbX<sub>3</sub> systems. Changes in the A-site cation also influence the bandgap albeit to a lesser extent.<sup>94</sup>

In contrast to what is seen in organic solar cells, the excitons generated in perovskites such as MAPbI<sub>3</sub> have a low exciton binding energy and so can readily dissociate into free carriers at room temperature.

Another contributing factor to their high performance is that the photogenerated carriers exhibit a longer than expected carrier lifetime (on the hundreds of ns to  $\mu$ s timescale).<sup>95</sup> To understand this, it is necessary to appreciate the different recombination mechanisms that can take place.

There are three recombination pathways in lead halide perovskites: Shockley-Read-Hall recombination, radiative recombination and Auger recombination.

- Shockley-Read-Hall (SRH) recombination: Also known as trap-assisted recombination, this is a non-radiative mechanism whereby electrons in the conduction band, or holes in the valence band, can become "trapped" in energy levels which exist within the bandgap as a result of crystal defects and impurities within the structure. Once in the trap state, the electrons (or holes) can then undergo recom-

bination with a hole (or electron) in the valence (or conduction) band. Traps can be categorised as shallow or deep traps based on how close they are to either the conduction or valence band. The rate of SRH recombination is dependent upon the defect density of the material in question.

- Radiative recombination: Also termed bimolecular recombination, this is simply when an electron in the conduction band recombines with a hole in the valence band, emitting a photon.
- Auger recombination: Another non-radiative recombination mechanism, this occurs when an electron recombines with a hole, but transfers its excess energy to a third carrier (which can either be an electron or hole). This mechanism is favoured under high photoexcitation intensities.

The evolution of charge carriers,  $N$ , over time can therefore be given by the following equation:

$$\frac{dN(t)}{dt} = -k_3N^3 - k_2N^2 - k_1N \quad (1.14)$$

where  $k_1$ ,  $k_2$  and  $k_3$  are the rate constants for SRH, radiative and Auger recombination, respectively.

#### 1.4.4 2D perovskites

In spite of 3D perovskites exhibiting high device efficiencies, as well as presenting a low cost alternative to silicon solar cells, their primary drawback at the moment is their stability.<sup>96</sup> Intrinsic factors which impact their stability include ion migration leading to potential collapse of the perovskite lattice, reactions between the metal electrode and the perovskite layer and finally residual strain within the lattice which leads to chemical degradation.<sup>97</sup> Furthermore, light and moisture induced degradation, amongst other extrinsic factors, also impact the stability.<sup>98</sup> Whilst these issues can, in part, be mitigated via numerous different strategies such as compositional engi-

neering, a promising strategy is to use a different perovskite structure altogether.<sup>99,100</sup>

2D perovskites are formed when large organic cations are included in the chemical composition ensuring that the typical 3-dimensional structure cannot be formed. Instead, a layered structure is formed with layers of  $\text{PbI}_6$  octahedra being separated by the aforementioned organic cations, also termed spacers. 2D perovskites have the general chemical formula  $(\text{A}')_m\text{A}_{n-1}\text{B}_n\text{X}_{3n+1}$  where  $\text{A}'$  is a divalent ( $m = 1$ ) or monovalent ( $m = 2$ ) organic spacer cation.<sup>101</sup>

There are different orientations for 2D perovskites, with  $\langle 100 \rangle$  being the most common. This class can be further sub-divided into Ruddlesden-Popper (RP), Dion-Jacobsen (DJ) and alternating cations in the interlayer (ACI) phases (although at present, this orientation can only be formed by guanidinium cations).<sup>102</sup>

RP perovskites (**figure 1.11**) are formed with monovalent spacers forming a bilayer in between the inorganic layers which are offset laterally by half an octahedral unit. DJ perovskites, on the other hand, are formed with divalent spacers undergoing hydrogen bonding with the lead halide sheets. In this scenario, there is no lateral displacement of the lead halide layers.

As well as having different crystal orientations, the number of perovskite layers that form between the organic spacers,  $n$ , can be adjusted which has a significant impact on their properties. As 2D perovskites can be thought of as consisting of alternating lead halide sheets and organic spacer interlayers, they form multiple quantum well structures. At low values of  $n$  there is a strong quantum confinement effect, which can be seen by the blue shift of the band gap. As the value of  $n$  increases, the properties of the 2D perovskite become more similar to that of 3D perovskites.<sup>103</sup> Whilst the value of  $n$  can be controlled, it can be difficult to obtain phase pure 2D perovskites.

The increased stability exhibited in 2D perovskites arises from their large organic cations which provide a steric barrier for water adsorption onto their surface.<sup>104</sup> However, whilst showing enhanced stability when compared to 3D perovskites, their efficiencies are generally much lower (21% vs 25.5%). This is due to their wider optical

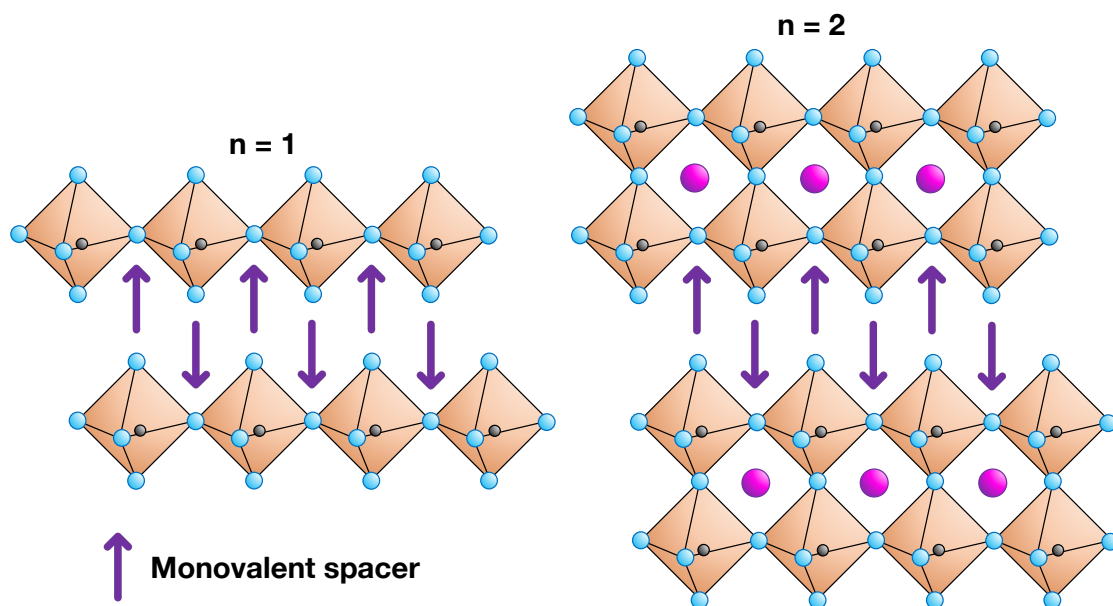


**Figure 1.11:** Structure of  $n = 1$  (left) and  $n = 2$  (right) 2D RP perovskites. The purple arrow corresponds to the monovalent organic cation.

bandgap as well as a larger exciton binding energy resulting in excitons being the dominant photoexcited species, as opposed to free charge carriers in 3D perovskites.<sup>93,105</sup> Therefore, they are often used as a capping layer atop regular 3D perovskites in order to benefit from their enhanced stability whilst maintaining a high efficiency.<sup>106</sup>

Asides from photovoltaics, the interesting properties of 2D perovskites have led them to be used in other applications. For example, their high exciton binding energy can enhance radiative recombination allowing them to be used as light-emitting diodes.<sup>107</sup> Furthermore, their strong spin-orbit coupling and enhanced Rashba effect make them good potential candidates for applications in the field of spintronics.<sup>108</sup>





## References

- (1) R. J. Dunn, D. M. Stanitski, N. Gobron and K. M. Willett, State of the Climate in 2019, Bull. Amer. Meteor., 2020, vol. 101, S9–S127.
- (2) P. Shukla, J. Skeea, R. Slade, A. Al Khourdajie, R. van Diemen, D. McCollum, M. Pathak, S. Some, P. Vyas, R. Fradera, M. Belkacemi, A. Hasija, G. Lisboa, S. Luz and J. Malley, Climate Change 2022: Mitigation of Climate Change, Cambridge University Press, Cambridge, UK and New York, USA, 2022.
- (3) F. Lafond, A. G. Bailey, J. D. Bakker, D. Rebois, R. Zadourian, P. McSharry and J. D. Farmer, *Technol. Forecast. Soc. Change*, 2018, **128**, 104–117.
- (4) IRENA, Renewable power generation costs in 2019, International Renewable Energy Agency, Abu Dhabi, 2020.
- (5) A. Bett, B. Burger, L. Friedrich, C. Kost, S. Nold, D. Peper, S. Philipps, R. Preu, J. Rentsch, G. Stryi-Hipp, H. Wirth and W. Warmuth, Fraunhofer ISE: Photovoltaics Report, Fraunhofer ISE, Freiburg, 2022.
- (6) P. Atkins and J. de Paula, Atkins' Physical Chemistry, Oxford University Press, Oxford, 10th, 2014.
- (7) J. Moser, Photochemistry I, EPFL, 2021.
- (8) S. Haque, Photochemistry, Imperial College London, 2015.
- (9) E. Becquerel, *C. R. Acad. Sci.*, 1839, 561.
- (10) M. Planck, *Ann. Phys.*, 1901, **4**, 553–563.
- (11) A. Einstein, *Ann. Phys.*, 1905, 132–148.
- (12) A. Pochettino, *Acad. Lincei Rend*, 1906, **15**, 355.

- (13) D. Kearns and M. Calvin, *J. Chem. Phys.*, 1958, **29**, 950–951.
- (14) H. Spanggaard and F. C. Krebs, *Sol. Energy Mater. Sol. Cells*, 2004, **83**, 125–146.
- (15) M. I. Federov and V. A. Benderskii, *Sov. Phys. Semiconduct.*, 1971, **4**, 1198–1199.
- (16) C. W. Tang, *Appl. Phys. Lett.*, 1986, **48**, 183–185.
- (17) M. Hiramoto, H. Fujiwara and M. Yokoyama, *Appl. Phys. Lett.*, 1991, **58**, 1062–1064.
- (18) J. J. M. Halls, C. A. Walsh, N. C. Greenham, E. A. Marseglia, R. H. Friend, S. C. Moratti and A. B. Holmes, *Nature*, 1995, **376**, 498–500.
- (19) G. Yu, J. Gao, J. Hummelen, F. Wudl and A. Heeger, *Science*, 1995, **270**, 1789–1791.
- (20) J. Yuan, Y. Zhang, L. Zhou, G. Zhang, H. L. Yip, T. K. Lau, X. Lu, C. Zhu, H. Peng, P. A. Johnson, M. Leclerc, Y. Cao, J. Ulanski, Y. Li and Y. Zou, *Joule*, 2019, **3**, 1140–1151.
- (21) C. Chaing, C. Fincher, Jr., Y. Park, A. Heeger, H. Shirakawa, E. Louis, S. Gau and A. MacDiarmid, *Phys. Rev. Lett.*, 1977, **39**, 1098–1101.
- (22) B. Kraabel, D. McBranch, C. Lee, A. Heeger, N. Sariciftci and D. Moses, *Chem. Phys. Lett.*, 1993, **213**, 389–394.
- (23) S. E. Shaheen, C. J. Brabec, N. S. Sariciftci, F. Padinger, T. Fromherz and J. C. Hummelen, *Appl. Phys. Lett.*, 2001, **78**, 841–843.
- (24) M. Jørgensen, K. Norrman, S. A. Gevorgyan, T. Tromholt, B. Andreasen and F. C. Krebs, *Adv. Mater.*, 2012, **24**, 580–612.
- (25) R. Po, A. Bernardi, A. Calabrese, C. Carbonera, G. Corso and A. Pellegrino, *Energy Environ. Sci.*, 2014, **7**, 925–943.
- (26) X. Guo, C. Cui, M. Zhang, L. Huo, Y. Huang, J. Hou and Y. Li, *Energy Environ. Sci.*, 2012, **5**, 7943–7949.
- (27) G. Li, W. H. Chang and Y. Yang, *Nat. Rev. Mater.*, 2017, **2**, 1–13.
- (28) Z. He, B. Xiao, F. Liu, H. Wu, Y. Yang, S. Xiao, C. Wang, T. P. Russell and Y. Cao, *Nat. Photonics*, 2015, **9**, 174–179.

- 
- (29) L. Dou, W. H. Chang, J. Gao, C. C. Chen, J. You and Y. Yang, *Adv. Mater.*, 2013, **25**, 825–831.
- (30) Y. Cui, Y. Xu, H. Yao, P. Bi, L. Hong, J. Zhang, Y. Zu, T. Zhang, J. Qin, J. Ren, Z. Chen, C. He, X. Hao, Z. Wei and J. Hou, *Adv. Mater.*, 2021, **33**, 2102420.
- (31) S. Yoo, B. Domercq and B. Kippelen, *Appl. Phys. Lett.*, 2004, **85**, 5427–5429.
- (32) R. Fitzner, E. Mena-Osteritz, A. Mishra, G. Schulz, E. Reinold, M. Weil, C. Körner, H. Ziehlke, C. Elschner, K. Leo, M. Riede, M. Pfeiffer, C. Uhrich and P. Bäuerle, *J. Am. Chem. Soc.*, 2012, **134**, 11064–11067.
- (33) D. Morel, A. Ghosh, T. Feng, E. Stogryn, P. Purwin, R. Shaw and C. Fishman, *Appl. Phys. Lett.*, 1978, **32**, 495–497.
- (34) C. M. Lin, S. M. Usama and K. Burgess, *Molecules*, 2018, **23**, 2900.
- (35) L. Brooker, F. Hamer and C. Mees, *J. Opt. Soc. Am.*, 1933, **23**, 216–222.
- (36) A. Pertegás, D. Tordera, J. J. Serrano-Pérez, E. Ortí and H. J. Bolink, *J. Am. Chem. Soc.*, 2013, **135**, 18008–18011.
- (37) R. C. Nelson, *J. Opt. Soc. Am.*, 1956, **46**, 10–13.
- (38) G. Pepe, J. M. Cole, P. G. Waddell and S. McKechnie, *Mol. Syst. Des. Eng.*, 2016, **1**, 86–98.
- (39) A. Ehret, L. Stuhl and M. Spitler, *J. Phys. Chem. B*, 2001, **105**, 9960–9965.
- (40) A. C. Véron, H. Zhang, A. Linden, F. Nüesch, J. Heier, R. Hany and T. Geiger, *Org. Lett.*, 2014, **16**, 1044–1047.
- (41) D. Gesevičius, A. Neels, S. Jenatsch, E. Hack, L. Viani, S. Athanasopoulos, F. Nüesch and J. Heier, *Adv. Sci.*, 2018, **5**, 1700496.
- (42) D. Gesevičius, A. Neels, S. Yakunin, E. Hack, M. V. Kovalenko, F. Nüesch and J. Heier, *ChemPhysChem*, 2018, **19**, 3356–3363.
- (43) H. Zhang, B. Niesen, E. Hack, S. Jenatsch, L. Wang, A. C. Véron, M. Makha, R. Schneider, Y. Arroyo, R. Hany and F. Nüesch, *Org. Electron.*, 2016, **30**, 191–199.
- (44) M. F. Abdelbar, T. A. Fayed, T. M. Meaz, T. Subramani, N. Fukata and E. Z. M. Ebeid, *J. Photochem. Photobiol. A*, 2019, **375**, 166–174.

- (45) A. C. Véron, A. Linden, N. A. Leclaire, E. Roedern, S. Hu, W. Ren, D. Rentsch and F. A. Nüesch, *J. Phys. Chem. Lett.*, 2018, **9**, 2438–2442.
- (46) A. Treibs and K. Jacob, *Angew. Chem., Int. Ed. Engl.*, 1965, **4**, 2547.
- (47) G. Chen, H. Sasabe, T. Igarashi, Z. Hong and J. Kido, *J. Mater. Chem. A*, 2015, **3**, 14517–14534.
- (48) V. Y. Merritt and H. J. Hovel, *Appl. Phys. Lett.*, 1976, **29**, 414–415.
- (49) A. Otsuka, K. Funabiki, N. Sugiyama, T. Yoshida, H. Minoura and M. Matsui, *Chem. Lett.*, 2006, **35**, 666–667.
- (50) F. Silvestri, M. D. Irwin, L. Beverina, A. Facchetti, G. A. Pagani and T. J. Marks, *J. Am. Chem. Soc.*, 2008, **130**, 17640–17641.
- (51) S. Wang, E. I. Mayo, M. D. Perez, L. Griffe, G. Wei, P. I. Djurovich, S. R. Forrest and M. E. Thompson, *Appl. Phys. Lett.*, 2009, **94**, 233304.
- (52) G. Wei, S. Wang, K. Sun, M. E. Thompson and S. R. Forrest, *Adv. Energy Mater.*, 2011, **1**, 184–187.
- (53) J. D. Zimmerman, B. E. Lassiter, X. Xiao, K. Sun, A. Dolocan, R. Gearba, D. A. Vanden Bout, K. J. Stevenson, P. Wickramasinghe, M. E. Thompson and S. R. Forrest, *ACS Nano*, 2013, **7**, 9268–9275.
- (54) K. Strassel, A. Kaiser, S. Jenatsch, A. C. Véron, S. B. Anantharaman, E. Hack, M. Diethelm, F. Nüesch, R. Aderne, C. Legnani, S. Yakunin, M. Cremona and R. Hany, *ACS Appl. Mater. Interfaces*, 2018, **10**, 11063–11069.
- (55) K. Strassel, W. H. Hu, S. Osbild, D. Padula, D. Rentsch, S. Yakunin, Y. Shynkarenko, M. Kovalenko, F. Nüesch, R. Hany and M. Bauer, *Sci. Technol. Adv. Mater.*, 2021, **22**, 194–204.
- (56) C. B. Nielsen, S. Holliday, H. Y. Chen, S. J. Cryer and I. McCulloch, *Acc. Chem. Res.*, 2015, **48**, 2803–2812.
- (57) T. Kumari, S. M. Lee, S. H. Kang, S. Chen and C. Yang, *Energy Environ. Sci.*, 2017, **10**, 258–265.
- (58) Y. J. Hsieh, Y. C. Huang, W. S. Liu, Y. A. Su, C. S. Tsao, S. P. Rwei and L. Wang, *ACS Appl. Mater. Interfaces*, 2017, **9**, 14808–14816.

- 
- (59) H. Youjun, C. Hsiang-Yu, H. Jianhui and L. Yongfang, *J. Am. Chem. Soc.*, 2010, **132**, 1377–1382.
- (60) C. Yan, S. Barlow, Z. Wang, H. Yan, A. K. Jen, S. R. Marder and X. Zhan, *Nat. Rev. Mater.*, 2018, **3**, 1–19.
- (61) Y. Lin, J. Wang, Z. G. Zhang, H. Bai, Y. Li, D. Zhu and X. Zhan, *Adv. Mater.*, 2015, **27**, 1170–1174.
- (62) F. Zhao, S. Dai, Y. Wu, Q. Zhang, J. Wang, L. Jiang, Q. Ling, Z. Wei, W. Ma, W. You, C. Wang and X. Zhan, *Adv. Mater.*, 2017, **29**, 1700144.
- (63) F. Wudl, N. Sariciftci, L. Smilowitz and A. Heeger, *Science*, 1992, **258**, 1474–1476.
- (64) C. J. Brabec, G. Zerza, G. Cerullo, S. De Silvestri, S. Luzzati, J. C. Hummelen and S. Sariciftci, *Chem. Phys. Lett.*, 2001, **340**, 232–236.
- (65) G. Grancini, M. Maiuri, D. Fazzi, A. Petrozza, H. J. Egelhaaf, D. Brida, G. Cerullo and G. Lanzani, *Nat. Mater.*, 2013, **12**, 29–33.
- (66) T. Virgili, D. Marinotto, C. Manzoni, G. Cerullo and G. Lanzani, *Phys. Rev. Lett.*, 2005, **94**, 1–4.
- (67) H. Ohkita, S. Cook, Y. Astuti, W. Duffy, S. Tierney, W. Zhang, M. Heeney, I. McCulloch, J. Nelson, D. D. Bradley and J. R. Durrant, *J. Am. Chem. Soc.*, 2008, **130**, 3030–3042.
- (68) T. M. Clarke, A. M. Ballantyne, J. Nelson, D. D. Bradley and J. R. Durrant, *Adv. Func. Mater.*, 2008, **18**, 4029–4035.
- (69) T. M. Clarke, J. R. Durrant, A. M. Ballantyne, J. Nelson, S. Tierney, M. Heeney, W. Duffy and I. McCulloch, *J. Phys. Chem. C*, 2010, **114**, 8068–8075.
- (70) J. Lee, K. Vandewal, S. R. Yost, M. E. Bahlke, L. Goris, M. A. Baldo, J. V. Manca and T. V. Voorhis, *J. Am. Chem. Soc.*, 2010, **132**, 11878–11880.
- (71) K. Vandewal, S. Albrecht, E. T. Hoke, K. R. Graham, J. Widmer, J. D. Douglas, M. Schubert, W. R. Mateker, J. T. Bloking, G. F. Burkhard, A. Sellinger, J. M. J. Fréchet, A. Amassian, M. K. Riede, M. D. McGehee, D. Neher and A. Salleo, *Nat. Mater.*, 2014, **13**, 63–68.

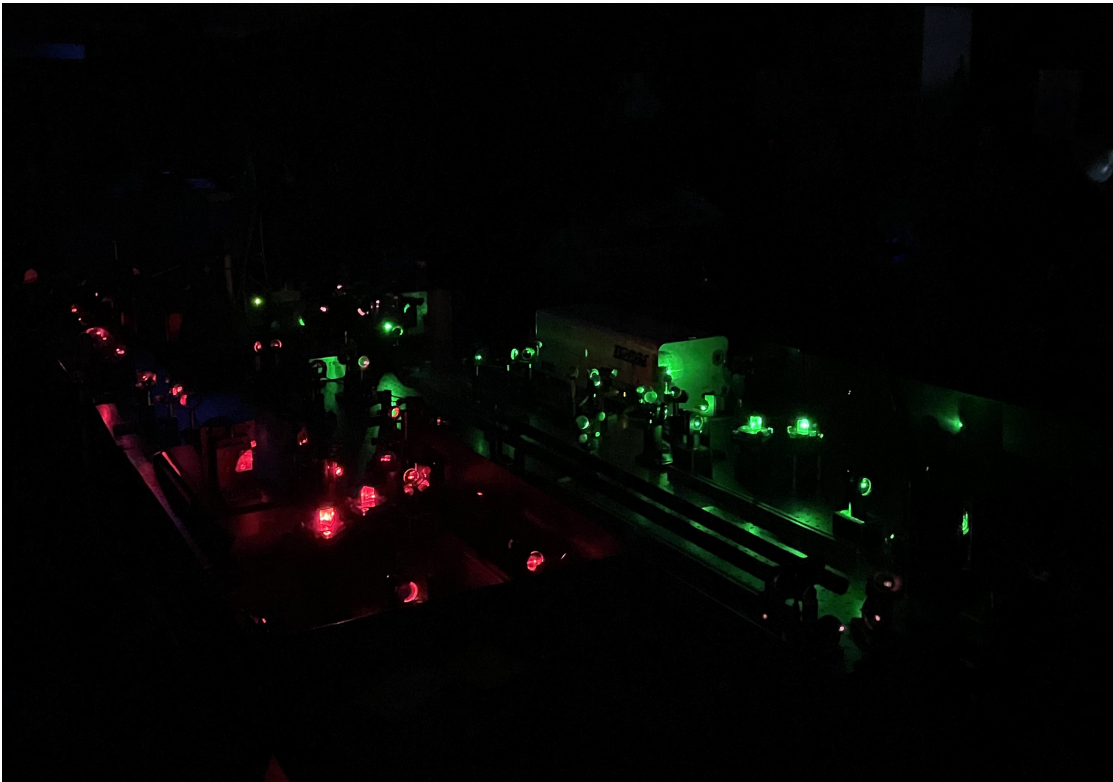
- (72) Z. Huang, D. Ji, S. Wang, A. Xia, F. Koberling, M. Patting and R. Erdmann, *J. Phys. Chem. A*, 2006, **110**, 45–50.
- (73) C. A. Guarín, J. P. Villabona-Monsalve, R. López-Arteaga and J. Peon, *J. Phys. Chem. B*, 2013, **117**, 7352–7362.
- (74) A. Devižis, J. De Jonghe-Risse, R. Hany, F. Nüesch, S. Jenatsch, V. Gulbinas and J. E. Moser, *J. Am. Chem. Soc.*, 2015, **137**, 8192–8198.
- (75) J. De Jonghe-Risse, J. Heier, F. Nüesch and J. E. Moser, *J. Mater. Chem. A*, 2015, **3**, 10935–10941.
- (76) G. M. Paternò, N. Barbero, S. Galliano, C. Barolo, G. Lanzani, F. Scotognella and R. Borrelli, *J. Mater. Chem. C*, 2018, **6**, 2778–2785.
- (77) S. Das, P. V. Kamat, B. De La Barre, K. G. Thomas, A. Ajayaghosh and M. V. George, *J. Phys. Chem.*, 1992, **96**, 10327–10330.
- (78) A. Rana, C. Sharma, D. D. Prabhu, M. Kumar, Y. Karuvath, S. Das, S. Chand and R. K. Singh, *AIP Adv.*, 2018, **8**, 045302.
- (79) E. Vauthey, *ChemPhysChem*, 2012, **13**, 2001–2011.
- (80) M. Kellogg, A. Akil, D. S. Muthiah Ravinson, L. Estergreen, S. E. Bradforth and M. E. Thompson, *Faraday Discuss.*, 2019, **216**, 379–394.
- (81) A. Weller, *Z. Phys. Chem.*, 1982, **133**, 93–98.
- (82) E. Sebastian and M. Hariharan, *ACS Energy Lett.*, 2022, **7**, 696–711.
- (83) A. F. Coleman, M. Chen, J. Zhou, J. Y. Shin, Y. Wu, R. M. Young and M. R. Wasielewski, *J. Phys. Chem. C*, 2020, **124**, 10408–10419.
- (84) N. E. Powers-Riggs, X. Zuo, R. M. Young and M. R. Wasielewski, *J. Am. Chem. Soc.*, 2019, **141**, 17512–17516.
- (85) A. N. Bartynski, M. Gruber, S. Das, S. Rangan, S. Mollinger, C. Trinh, S. E. Bradforth, K. Vandewal, A. Salleo, R. A. Bartynski, W. Bruetting and M. E. Thompson, *J. Am. Chem. Soc.*, 2015, **137**, 5397–5405.
- (86) M. A. Green, A. Ho-Baillie and H. J. Snaith, *Nat. Photonics*, 2014, **8**, 506–514.

- 
- (87) P. S. Whitfield, N. Herron, W. E. Guise, K. Page, Y. Q. Cheng, I. Milas and M. K. Crawford, *Sci. Rep.*, 2016, **6**, 35685.
- (88) D. Weber, *Z. Naturforsch.*, 1978, **33**, 1443–1445.
- (89) A. Kojima, K. Teshima, Y. Shirai and T. Miyasaka, *J. Am. Chem. Soc.*, 2009, **131**, 6050–6051.
- (90) J. H. Im, C. R. Lee, J. W. Lee, S. W. Park and N. G. Park, *Nanoscale*, 2011, **3**, 4088–4093.
- (91) H. S. Kim, C. R. Lee, J. H. Im, K. B. Lee, T. Moehl, A. Marchioro, S. J. Moon, R. Humphry-Baker, J. H. Yum, J. E. Moser, M. Grätzel and N. G. Park, *Sci. Rep.*, 2012, **2**, 1–7.
- (92) M. M. Lee, J. Teuscher, T. Miyasaka, T. N. Murakami and H. J. Snaith, *Science*, 2012, **338**, 643–647.
- (93) J. Jeong, M. Kim, J. Seo, H. Lu, P. Ahlawat, A. Mishra, Y. Yang, M. A. Hope, F. T. Eickemeyer, M. Kim, Y. J. Yoon, I. W. Choi, B. P. Darwich, S. J. Choi, Y. Jo, J. H. Lee, B. Walker, S. M. Zakeeruddin, L. Emsley, U. Rothlisberger, A. Hagfeldt, D. S. Kim, M. Grätzel and J. Y. Kim, *Nature*, 2021, **592**, 381–385.
- (94) D. Marongiu, M. Saba, F. Quochi, A. Mura and G. Bongiovanni, *J. Mater. Chem. C*, 2019, **7**, 12006–12018.
- (95) C. Wehrenfennig, G. E. Eperon, M. B. Johnston, H. J. Snaith and L. M. Herz, *Adv. Mater.*, 2014, **26**, 1584–1589.
- (96) L. Meng, J. You and Y. Yang, *Nat. Commun.*, 2018, **9**, 5265.
- (97) Y. Cheng and L. Ding, *Energy Environ. Sci.*, 2021, **14**, 3233–3255.
- (98) S. Zhang and G. Han, *Prog. Energy*, 2020, **2**, 022002.
- (99) J. Ye, H. Zheng, L. Zhu, G. Liu, X. Zhang, T. Hayat, X. Pan and S. Dai, *Sol. RRL*, 2017, **1**, 1–8.
- (100) R. Garai, R. K. Gupta, M. Hossain and P. K. Iyer, *J. Mater. Chem. A*, 2021, **9**, 26069–26076.
- (101) X. Li, J. M. Hoffman and M. G. Kanatzidis, *Chem. Rev.*, 2021, **121**, 2230–2291.

- (102) C. M. M. Soe, C. C. Stoumpos, M. Kepenekian, B. Traoré, H. Tsai, W. Nie, B. Wang, C. Katan, R. Seshadri, A. D. Mohite, J. Even, T. J. Marks and M. G. Kanatzidis, *J. Am. Chem. Soc.*, 2017, **139**, 16297–16309.
- (103) C. Liang, H. Gu, Y. Xia, Z. Wang, X. Liu, J. Xia, S. Zuo, Y. Hu, X. Gao, W. Hui, L. Chao, T. Niu, M. Fang, H. Lu, H. Dong, H. Yu, S. Chen, X. Ran, L. Song, B. Li, J. Zhang, Y. Peng, G. Shao, J. Wang, Y. Chen, G. Xing and W. Huang, *Nat. Energy*, 2021, **6**, 38–45.
- (104) S. Yang, Y. Wang, P. Liu, Y. B. Cheng, H. J. Zhao and H. G. Yang, *Nat. Energy*, 2016, **1**, 15016.
- (105) M. Shao, T. Bie, L. Yang, Y. Gao, X. Jin, F. He, N. Zheng, Y. Yu and X. Zhang, *Adv. Mater.*, 2022, **34**, 2107211.
- (106) G. Li, J. Song, J. Wu, Z. Song, X. Wang, W. Sun, L. Fan, J. Lin, M. Huang, Z. Lan and P. Gao, *ACS Energy Lett.*, 2021, **6**, 3614–3623.
- (107) C. Sun, Y. Jiang, M. Cui, L. Qiao, J. Wei, Y. Huang, L. Zhang, T. He, S. Li, H. Y. Hsu, C. Qin, R. Long and M. Yuan, *Nat. Commun.*, 2021, **12**, 2207.
- (108) F. Zhang, H. Lu, J. Tong, J. J. Berry, M. C. Beard and K. Zhu, *Energy Environ. Sci.*, 2020, **13**, 1154–1186.



## 2 Experimental methods



The purpose of this chapter is to give the reader an overview of the different ultrafast spectroscopic techniques used in this thesis. The first part introduces laser spectroscopy in general, before each experimental technique is presented with both the experimental details and the theoretical background being covered.

### 2.1 An introduction to laser spectroscopy

Spectroscopy, a term that will be used throughout this thesis, refers to the study of the absorption or emission of electromagnetic radiation by matter. In general, ultrafast spectroscopy is used as a blanket term to refer to the study of processes which occur on timescales ranging from attoseconds to nanoseconds. Depending on the time resolution and the energy of radiation required to excite the desired sample, a variety of different laser systems can be used.

As suggested by their name, lasers produce radiation via stimulated emission. There are three key components to a basic laser: the lasing medium, an excitation source and finally the optical cavity. The lasing medium, also called gain medium, is a material which emits radiation in all directions following excitation. The lasing medium is excited by the excitation source, typically a lamp or another laser, resulting in electrons being excited within the lasing medium. Once a population inversion has occurred, which is where a higher lying state is more populated than a lower energy state, spontaneous emission occurs. Neighbouring atoms within the lasing medium absorb the spontaneously emitted photons, resulting in stimulated emission. The result is an optical amplifier which when placed inside of an optical cavity results in a laser.

Lasers are either continuous wave (CW) or pulsed, the difference between them being that CW lasers produce an uninterrupted beam of radiation whilst pulsed lasers emit a train of laser pulses. To obtain pulsed lasers, either Q-switching or mode-locking is used. Q-switching is a technique whereby the laser radiation is kept inside the optical cavity until a sufficient population inversion is reached. Q-switched lasers generate high energy pulses, typically with a nanosecond pulse duration. Conversely, mode-

locking works by locking the phases of oscillating photons within the cavity to each other, resulting in constructive interference eventually yielding pulses with a shorter duration and a higher repetition rate than can be achieved with Q-switched lasers.<sup>1</sup>

Pulsed lasers operating at high intensities can cause damage to the amplifying medium. To overcome this, a technique called chirped pulse amplification (CPA) was developed. CPA refers to a technique whereby the laser pulse is stretched temporally before passing through the amplifying medium.<sup>2</sup> It is then directed through a compressor, resulting in a beam with a short pulse duration but high power. Stretching the pulse before amplification prevents damage to the amplifying medium. The advent of CPA lasers paved the way for new experiments as a result of the high power and short pulse duration that can be generated in comparison to conventional lasers.

## 2.2 Transient absorption spectroscopy

Transient absorption spectroscopy, shortened to TAS or TA, is a pump-probe technique which gives time resolved information on the transient species that are formed upon photoexcitation of a sample. As such, it is a powerful technique which can be used to study a variety of different systems and phenomena including, but by no means limited to, photosynthetic systems,<sup>3</sup> protein fluorescence<sup>4,5</sup> and semiconductor thin films.<sup>6</sup>

The premise of the technique is simple: first, the sample is excited by the pump beam, the wavelength of which can be tuned according to the needs of the experiment. Then, following this excitation, the perturbed sample is monitored by a low photon fluence white light beam called the probe, which allows one to measure the absorption of the sample after photoexcitation. By using a mechanical delay stage, the time delay between the pump and probe beam can be changed, which gives the time evolution of the measurement. Therefore, we can follow the generation and decay of photogenerated species within the sample. The temporal resolution of these measurements, limited by the pulse width of the pump beam, is around 150 fs for our experimental setup; the

time window of the measurement is 1.2 ns, and is limited by the length of the delay stage.

TAS is a differential technique, and so the signal measured,  $\Delta A$ , is given by the following equation:

$$\Delta A(\lambda, t) = A(\lambda, t)_{pump} - A(\lambda, t)_{nopump} \quad (2.1)$$

where  $A(\lambda, t)_{pump}$  is the absorbance of the probe in the presence of the pump, and  $A(\lambda, t)_{nopump}$  is the absorbance of the probe in the absence of the pump.

Processes which increase the amount of probe light reaching the detector appear as negative features in a TA spectrum, whilst signals that diminish the amount of probe light reaching the detector appear as positive features. A TA spectrum contains contributions that arise from different processes, which all combine to give the overall TA spectrum an example of which can be seen in **figure 2.1**.<sup>7</sup> These processes are:

- **Ground-state Bleaching (GSB):** This occurs when the pump beam is absorbed by the sample, thereby diminishing the population of the ground state. Therefore, the probe beam cannot be absorbed, and so more probe light reaches the detector. As a result, the GSB appears as a negative signal. As it arises from the absorption of the pump beam, the shape of the GSB typically mirrors that of the steady-state absorption spectrum.
- **Stimulated Emission (SE):** This occurs when the probe beam interacts with electrons in the excited state causing them to recombine with holes in the ground state, resulting in the emission of a photon. Because stimulated emission can only occur for optically allowed transitions, the shape and position of the SE in the TA spectrum is close to that of the steady state photoluminescence spectrum. Like the GSB, SE results in more photons reaching the detector, and so it appears as a negative signal.
- **Excited State Absorption (ESA):** After excitation by the pump, it is possible for

excitation to higher-lying excited states to occur which leads to parts of the probe being absorbed. The result is that fewer photons reach the detector, and so the ESA appears as a positive feature.

- **Product Absorption:** After photoexcitation by the pump beam has occurred, it is possible for reactions to take place that result in transient or long-lived molecular states. For example, triplet state formation, photoisomerisation and the formation of reduced/oxidised species can occur, and the products of these reactions can absorb part of the probe. As with the ESA, fewer photons reach the detector in this case, and so product absorption appears as a positive feature.

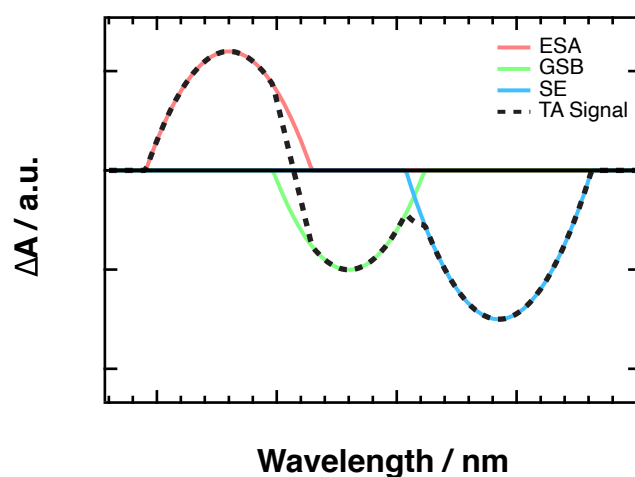


**Figure 2.1:** Contributions to the TA spectrum (dashed black line): ground-state bleaching (green), stimulated emission (blue) and excited state absorption (red).

### 2.2.1 Experimental setup

The TA setup was built in our lab by S. Pelet,<sup>8</sup> and subsequently developed over the years.

## Laser source

The laser source used for the TA setup is a chirped pulse amplification (CPA) Ti:Sapphire laser (CPA 2001, Clark MXR). The seed for the Ti:Sapphire is provided by an erbium-doped fibre, which provides a frequency-doubled output of 775 nm. This seed is stretched in time, in order to prevent energy damage. The Ti:Sapphire is pumped by the frequency doubled output of a Nd:YAG laser (532 nm, 7.2 W), itself being pumped by an arc lamp. The output of the Ti:Sapphire is then compressed, resulting in a fundamental wavelength of 778 nm with a pulse length of approximately 120 fs and an average peak power of 930  $\mu$ J at a repetition rate of 1 kHz. A diagram of the TA setup is shown in **figure 2.2**.

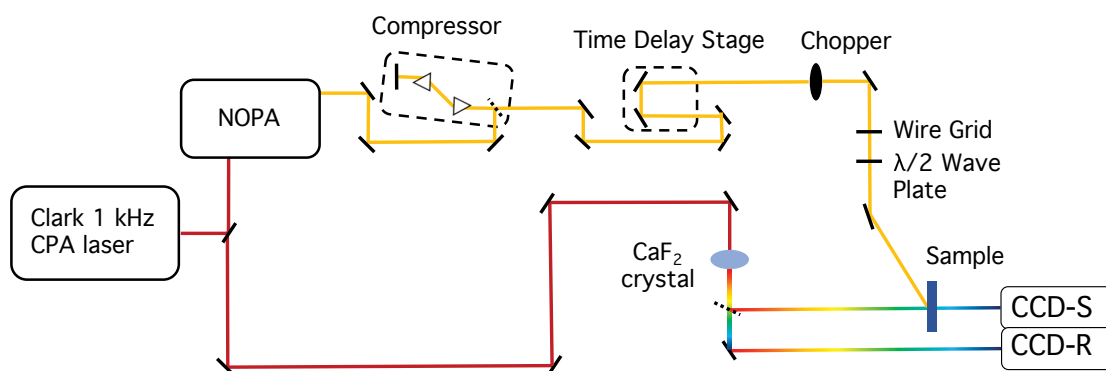


**Figure 2.2:** Schematic of the transient absorption spectroscopy setup.

## White light generation

The output of the laser is subsequently split into two beams, with one beam providing the pump and the other the probe.

The broadband white light probe is generated by passing the fundamental through a non-linear crystal (either a 4 mm thick sapphire window, or a 5 mm thick calcium fluoride ( $\text{CaF}_2$ ) plate). The advantage of using  $\text{CaF}_2$  is that it generates a broader white light, extending into the near-infrared (up to 1050 nm) and the UV, when compared to the sapphire crystal. However, it is more susceptible to damage and so a function

generator is used to oscillate the crystal to prevent damage.

The probe then passes through a polariser, in order to remove unwanted residuals, and suitable bandpass filters (305-700 nm) which remove excess components of the fundamental wavelength (778 nm).

### **Generating the pump**

The second part of the fundamental is used to generate the pump. Tuning the pump beam allows you to tune the excitation wavelength according to the absorption spectrum of the sample. The easiest method to pump the sample would be to simply use the fundamental at 778 nm; however, many systems do not absorb at this wavelength and so it is necessary to generate the pump wavelength which is typically done using one of two methods. Firstly, it is possible to pump samples using the second harmonic (389 nm) which is generated by passing the fundamental through a type-I  $\beta$ -barium borate (BBO) crystal.

For excitation at wavelengths other than 389 nm, a 2 stage non-collinear optical parametric amplifier (NOPA-Plus, Clark MXR) is used which allows for wavelengths between 450 and 1520 nm to be achieved. The incoming fundamental is split into two beams: the first provides the seed for the first stage, and is passed through a sapphire crystal in order to generate a white light continuum. The second part passes through a BBO crystal generating the second harmonic (389 nm). The 389 nm beam is then further split into two parts which constitute the pump beams for the two stages of the NOPA.

The first pump beam is overlapped with the white light seed in a second BBO crystal, generating an output which can be tuned by changing the time delay and the BBO tilt angle. This output is then used as the seed for the second stage, where it is spatially and temporally overlapped with the remaining 389 nm pump in order to amplify the output from the first stage. Due to the structure of the fundamental, it is difficult to achieve a good NOPA output in the wavelength ranges 700-900 nm. To overcome this,

a second white light generation stage, which is pumped by the near-infrared output of the first stage, is added allowing for a better output in this range to be achieved. To achieve NOPA outputs in the wavelength range 900-1500 nm, the idler is used as the output.

If the desired pump beam is in the visible region, the output of the NOPA can be compressed using a pair of SF10 prisms set at Brewster's angle to reduce reflective losses. These correct for group velocity dispersion; typically, pulse widths of around 50 fs can be achieved by careful optimisation of the distance between the two prisms. If the desired pump beam is in the infrared there is no need to compress it, and so the prisms can be bypassed.

A chopper set at 500 Hz (half the frequency of the fundamental) modulates the frequency of the pump beam, enabling the absorption with and without the pump to be acquired during the same measurement.

The polarisation of the pump relative to the probe can be adjusted, depending on whether one wants to study anisotropic effects or not. Typically, the pump and probe polarisation are set to magic angle so that effects due to anisotropy can be ignored.

### **Detection and data collection**

Having generated the pump and the probe, the probe beam is subsequently split into two, with one part going to the sample whilst the other passes directly to the reference camera. This is to account for shot-to-shot variations in the white light.

The signal and reference beams are detected by two spectrographs (Princeton Instruments, SpectraPro 2150) using 512 x 58 pixel back-thinned CCD cameras (Hamamatsu S70-30-0906). Depending on the wavelength window being monitored, two different gratings can be used: 500 nm blaze, suitable for analysis between 350 and 800 nm, and 800 nm blaze which operates from 800 - 1200 nm. For operation in the visible, 350 - 710 nm bandpass filters are used to discard the remainder of the fundamental, whilst 750 or 800 nm long-pass filters are used for detection in the near-IR.



The probe beams are detected shot-to-shot, and typically 3000 shots are averaged in order to obtain a good signal-to-noise ratio. Generally, if the signal of a sample is particularly weak, it is better to increase the number of scans rather than increase the number of shots. Dark counts are acquired before each measurement and subtracted from the transmitted light intensity for each camera. Data are acquired using an in-house developed LabVIEW program.

### Data treatment

Before the dataset can be plotted and analysed, it must first be treated in order to account for the chirp. The chirp arises due to group velocity dispersion, whereby different wavelengths of light travel at different speeds through dispersive media. Because the probe consists of a broadband white light, the red light travels faster than the blue, and so reaches the detector at a different time. To account for this, the dataset is fitted to extract the time zero for each wavelength and set them to the same time. Once corrected, the spectra and dynamics can be plotted.

### Global analysis

TA spectra can be difficult to interpret, due to there being multiple contributions to different peaks as well as features which overlap. Global analysis is a powerful tool that can aid in the interpretation and analysis of transient spectra. The basic idea of global fitting is that several different kinetic traces are fitted with the same multiexponential function in order to find the parameters resulting in the best fit. Examples of the bi- and tri-exponential functions used are shown below:

$$\Delta A(\lambda, t) = A_0 + A_1(\lambda) \cdot \exp\left(\frac{-t}{\tau_1}\right) + A_2(\lambda) \cdot \exp\left(\frac{-t}{\tau_2}\right) \quad (2.2)$$

$$\Delta A(\lambda, t) = A_0 + A_1(\lambda) \cdot \exp\left(\frac{-t}{\tau_1}\right) + A_2(\lambda) \cdot \exp\left(\frac{-t}{\tau_2}\right) + A_3(\lambda) \cdot \exp\left(\frac{-t}{\tau_3}\right) \quad (2.3)$$

In order to perform a global fit, the data must first be sampled with a suitable number of wavelengths extracted; typically, wavelengths every 5 nm are chosen and the purpose of this is to ensure a good result whilst minimising the amount of computational power. A suitable kinetic model is then applied (typically a bi- or tri-exponential function), with all of the traces forced to evolve with the same time constants. Once a suitable fit has been achieved, the amplitude coefficients for each wavelength can be extracted into a new data set, yielding the decay associated spectra (DAS).

## 2.3 Electroabsorption spectroscopy

Electro-modulated differential absorption (EDA or EA) and time-resolved electroabsorption spectroscopy (TREAS) are powerful spectroscopic techniques which can give insight into the charge transport in a system, amongst other phenomena. For example, they have been used to study carrier mobility in conjugated polymers,<sup>9</sup> dissociation of charge transfer states in bilayer organic solar cells<sup>10</sup> and the dynamics of photocarriers in perovskites.<sup>11</sup>

EDA measurements give the steady state electroabsorption spectrum of a sample, which is the absorption spectrum of the sample under an applied electric field. TREAS measurements, meanwhile, show how the electroabsorption spectrum evolves over time.

Both techniques are based on the Stark effect. This is an effect whereby electronic transitions within the system are influenced by the application of an electric field which causes a shift in the absorption spectrum of the sample.<sup>12</sup> The impact of the electric field on the frequency of the transition is given by the following equation:

$$\Delta\nu = -\Delta\mu \cdot E - \frac{1}{2}\Delta\alpha \cdot E^2 \quad (2.4)$$

where  $\Delta\mu$  corresponds to the change in the dipole moment,  $\Delta\alpha$  is the change in the polarisability of the electronic transition and  $E$  is the applied electric field.

The change in the absorbance of a sample upon the application of an electric field can be expressed mathematically as a function of the frequency of electronic transitions. The Taylor expansion of this yields the following expression:

$$A(\nu, E) = A(\nu, E = 0) + \frac{dA}{d\nu} d\nu + \frac{1}{2} \frac{d^2A}{d\nu^2} d\nu^2 + \dots \quad (2.5)$$

Like TAS, both EDA and TREAS are differential techniques, and so the electroabsorption of a sample is given by:

$$EA = A(\nu, E) - A(\nu, E = 0). \quad (2.6)$$

By utilising the expression given for the frequency of an electronic transition (**equation 2.4**), and by substituting **equation 2.5** into **equation 2.6** and considering only the first three terms of the Taylor expansion, the following mathematical expression for the electroabsorption signal is obtained<sup>13</sup>:

$$EA = -\frac{dA}{d\nu} \Delta\mu \cdot E + \frac{1}{2} \frac{d^2A}{d\nu^2} E^2 \cdot \Delta\mu^2 - \frac{1}{2} \frac{dA}{d\nu} E^2 \cdot \Delta\alpha \quad (2.7)$$

The first term in this expression,  $\frac{dA}{d\nu} \Delta\mu \cdot E$ , is linear with respect to the electric field and is therefore 0 in isotropic systems. As mentioned previously,  $\Delta\mu$  corresponds to the change in the dipole moment. Therefore, the second term in **equation 2.7** informs us that changes in the dipole moment of the system are associated with the second derivative of the absorption spectrum. The third and final term in the equation demonstrates that the change in the polarisability of the system is associated with the first derivative of the absorption spectrum.

Therefore, by comparing the electroabsorption spectrum of a sample to the first and second derivative of its absorption spectrum, it is possible to determine whether the electroabsorption signals arise from changes in the dipole moment or the polarisability of the system. However, it is often the case that the electroabsorption spectrum will be

caused by changes in both the dipole moment and the polarisability of the system. As a result, the electroabsorption signal will resemble a linear combination of the first and second derivatives of the absorption spectrum.

Experimentally, EDA measurements consist of only the white light probe illuminating the sample, whereas TREAS involves the addition of the pump beam which excites the sample. The electron-hole pairs generated upon photoexcitation generate their own local electric field as they traverse the sample towards opposing electrodes. This local field opposes that of the applied field, resulting in a lower effective electric field across the sample. This leads to the spectral evolution that is seen in the measurements.

### Experimental setup

The experimental setup for the EDA/TREAS experiments is, in the most part, identical to the TAS setup. Both experiments are run off the same Ti:Sapphire CPA laser as used for the TAS experiments. The pump beam, used for TREAS, is once again generated by passing the 778 nm fundamental through a NOPA, whereas the white light probe is generated by passing the remainder of the fundamental through a 4 mm sapphire crystal.

The one obvious experimental difference between TA and EDA/TREAS measurements is the application of an electric field in the latter. In order for the field to be applied, the thin film sample should be sandwiched between two electrodes. One of the electrodes should be transparent, and is usually either fluorine- or indium- doped tin oxide (FTO or ITO). The other electrode is metal (aluminium, gold etc.) which is evaporated on top of the film. As a result, the measurements are done in reflectance mode, with illumination coming from the glass side of the sample and the probe beam reflecting off of the metal electrode. Furthermore, as can be seen in **figure 2.3**, an insulating layer is required between the transparent conductive oxide and the active layer. The purpose of this insulating layer is to prevent the active layer from being oxidised or reduced at the electrodes.

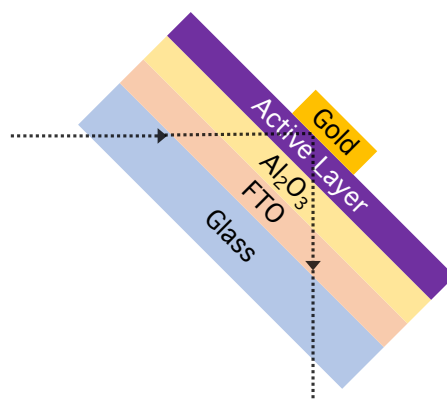


**Figure 2.3:** Cross section of a typical EDA/TREAS sample showing the different layers as well as the path of the white light probe.

The electric field across the sample is modulated at half the amplifier frequency (500 Hz) using square pulses generated by a function generator (Tektronix AFG 2001, from -10 to 10 V, 100  $\mu$ s duration), allowing for signal with and without the field to be acquired simultaneously. The current responses across the samples are recorded using a 50  $\Omega$  series load with a 400 MHz bandpass oscilloscope (Tektronix TDS 3044B). The signal and reference beam are once again dispersed into two separate spectrographs (SR163, Andor Instruments) and detected shot-to-shot at 1 kHz by 512 x 58 pixel back-thinned CCD cameras (Hamamatsu S07030-0906).

## 2.4 Time-of-flight

Time-of-flight (TOF) is an experimental technique that can be used to monitor charge transport in materials, allowing for the mobility of materials to be calculated.<sup>14</sup> It is of particular use in organic systems where the mobility is often too low to be found using other experimental techniques such as TREAS or time-resolved terahertz spectroscopy.<sup>15</sup>

Unlike the techniques seen previously, TOF experiments involve measuring photocurrent. Upon photoexcitation of the sample, electron-hole pairs are generated and are subsequently split into free charges by the applied electric field. This results in an

increase in the photocurrent. Once split, one of the charges is immediately collected by the nearby electrode, resulting in a partial decrease in the photocurrent. The other charge traverses the sample to be collected at the counter electrode.

The time taken for the charges to travel across the sample, which is experimentally seen as a decrease in the photocurrent, is called the transit time. This can be used in the following equation to calculate the mobility,  $\mu$ :

$$\mu = \frac{d^2}{E \cdot t_{tr}} \quad (2.8)$$

where  $d$  is the sample thickness,  $E$  the voltage applied across the sample and  $t_{tr}$  the transit time obtained from the TOF measurement.

As well as giving information on the mobility of the sample, the shape of the photocurrent curve can also give insight into the transport regime (dispersive vs non-dispersive).

The main difficulty with TOF measurements is being able to fabricate a suitable sample, consisting of the active layer sandwiched between two electrodes. The difficulty in sample preparation comes from the active layer thickness - typically it should be on the order of microns. This is necessary as it results in a homogeneous layer of charges being created upon photoexcitation, as the penetration depth of the light is far smaller than the overall sample thickness.

### Experimental setup

The excitation source was provided by a Nd:YAG Q-switched laser (Continuum Powerlite-7030) with a frequency-tripled output (355 nm) and a repetition rate of 0.2-20 Hz. This output was used to pump a broadband optical parametric oscillator (OPO-355, GWU) allowing for the excitation wavelength to be tuned. For TOF measurements, the laser was operated in a single shot mode. A 24 V series battery was used to apply a voltage across the sample during the measurement.

Typically, measurements were averaged over 10 shots in order to minimise the impact of oscillations, and between each measurement the voltage was switched off allowing the carriers to return to equilibrium. The photocurrent response from the sample was reported using an oscilloscope (DPO 7104, Tektronix, 1 M $\Omega$ ). A capacitor and a variable resistance box were placed in parallel to the battery in order to adjust the RC constant of the circuit. A diagram of the circuit can be seen in **figure 2.4**.

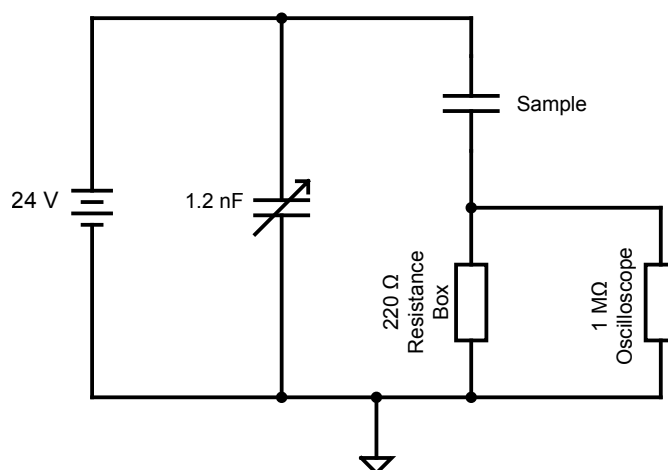


**Figure 2.4:** Scheme representing the circuit used for TOF measurements. The values of the variable capacitor and resistance box represent typical values used during TOF measurements, although they could be altered to adjust the RC constant of the circuit.





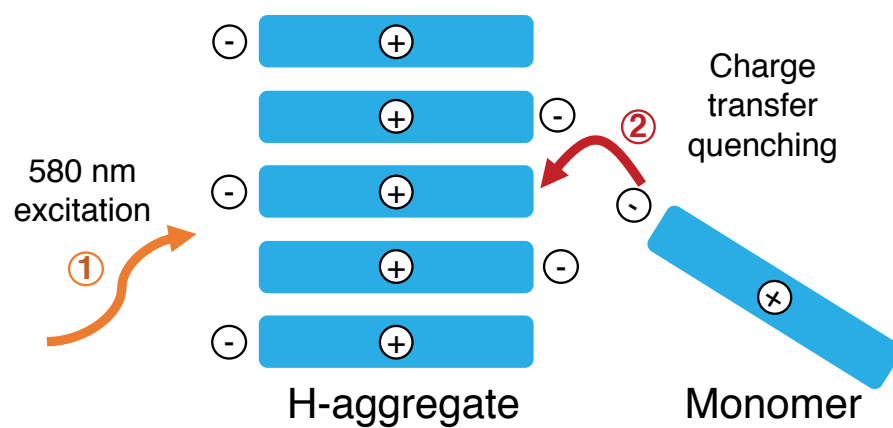


## References

- (1) R. A. M. Yusoff, A. A. A. Jafry, N. Kasim, N. F. Zulkipli, M. Yasin and S. W. Harun, *Results in Optics*, 2020, **1**, 100032.
- (2) D. Strickland and G. Mourou, *Opt. Commun.*, 1985, **56**, 219–221.
- (3) D. Kosumi, S. Maruta, T. Horibe, R. Fujii, M. Sugisaki, R. J. Cogdell and H. Hashimoto, *Angew. Chem., Int. Ed. Engl.*, 2011, **50**, 1097–1100.
- (4) E. Fron, C. Flors, G. Schweitzer, S. Habuchi, H. Mizuno, R. Ando, F. C. De Schryver, A. Miyawaki and J. Hofkens, *J. Am. Chem. Soc.*, 2007, **129**, 4870–4871.
- (5) C. C. Hsieh, P. T. Chou, C. W. Shih, W. T. Chuang, M. W. Chung, J. Lee and T. Joo, *J. Am. Chem. Soc.*, 2011, **133**, 2932–2943.
- (6) K. E. Knowles, M. D. Koch and J. L. Shelton, *J. Mater. Chem. C*, 2018, **6**, 11853–11867.
- (7) R. Berera, R. van Grondelle and J. T. Kennis, *Photosynth. Res.*, 2009, **101**, 105–118.
- (8) S. Pelet, Ph.D. Thesis, EPFL, 2002.
- (9) A. Devižis, A. Serbenta, K. Meerholz, D. Hertel and V. Gulbinas, *Phys. Rev. Lett.*, 2009, **103**, 1–4.
- (10) A. Devižis, J. De Jonghe-Risse, R. Hany, F. Nüesch, S. Jenatsch, V. Gulbinas and J. E. Moser, *J. Am. Chem. Soc.*, 2015, **137**, 8192–8198.
- (11) A. A. Paraecattil, J. De Jonghe-Risse, V. Pranculis, J. Teuscher and J. E. Moser, *J. Phys. Chem. C*, 2016, **120**, 19595–19602.
- (12) J. Stark, *Nature*, 1913, **92**, 401.

- (13) U. B. Cappel, S. M. Feldt, J. Schöneboom, A. Hagfeldt and G. Boschloo, *J. Am. Chem. Soc.*, 2010, **132**, 9096–9101.
- (14) B. Ebenhoch, S. A. Thomson, K. Genevičius, G. Juška and I. D. Samuel, *Org. Electron.*, 2015, **22**, 62–68.
- (15) E. A. Alharbi, A. Krishna, T. P. Baumeler, M. Dankl, G. C. Fish, F. Eickemeyer, O. Ouellette, P. Ahlawat, V. Škorjanc, E. John, B. Yang, L. Pfeifer, C. E. Avalos, L. Pan, M. Mensi, P. A. Schouwink, J. E. Moser, A. Hagfeldt, U. Rothlisberger, S. M. Zakeeruddin and M. Grätzel, *ACS Energy Lett.*, 2021, **6**, 3650–3660.

### 3 Mechanism of ultrafast intrinsic charge generation in pentamethine cyanine dyes



This chapter is based on the publication “Critical role of H-aggregation for high-efficiency photoinduced charge generation in pristine pentamethine cyanine salts”.<sup>1</sup> Transient absorption spectroscopy is used to unravel the intrinsic charge generation mechanism in a neat pentamethine cyanine dye, providing the first direct proof of high efficiency intrinsic charge generation. Following this, the impact of the counterion on the charge generation process is assessed; finally, electroabsorption spectroscopy and time-of-flight were employed to determine the impact of the counterion size on charge transport within the dyes.

The contributions from collaborating co-authors is gratefully acknowledged. J. M. Moreno-Naranjo aided with time-of-flight measurements. A. Billion and D. Kratzert synthesised and performed x-ray crystallography and Hirshfeld analysis on the Cy5-[Al(pftb)<sub>4</sub>] and Cy5-[Al(pfad)<sub>4</sub>] dyes. E. Hack performed ellipsometry measurements and Linfeng Pan acquired the SEM images.

### 3.1 Introduction

Cyanine dyes are a class of material that have a long history in the field of organic photovoltaics.<sup>2</sup> The first evidence of photoconductivity in cyanine thin films was presented in 1965. Since this period, they have been used extensively in organic photovoltaics, typically in combination with fullerene-based acceptors such as C<sub>60</sub>. One beneficial property of cyanine dyes is their high extinction coefficient (typically exceeding 10<sup>5</sup> L mol<sup>-1</sup> cm<sup>-1</sup>),<sup>3</sup> which allows them to be successfully used in bilayer architecture devices. The active layer can be thin enough to circumvent issues that typically thwart the performance, such as exciton recombination before diffusion to the donor/acceptor interface has occurred.<sup>4,5</sup> This makes them ideal systems for studying ultrafast charge transfer processes, as the morphology is far simpler than in bulk heterojunction devices.

As mentioned in the introduction, cyanine dyes comprise of a positively charged chromophore paired with a counterion which can be easily exchanged using ion ex-

change techniques.<sup>6</sup> This allows for a wide variety of counterions to be employed, including weakly coordinating anions (WCAs).<sup>7</sup> By changing the counterion, it is possible to impact the thin film properties as well as the device performance.<sup>8,9</sup>

In the past, studies focused on exploring the ultrafast processes in cyanine dyes have tended to concentrate on the fundamental photophysics of cyanine dyes in solution, such as its triplet state characteristics<sup>10</sup> and the dynamics of higher-lying excited states.<sup>11</sup> Meanwhile, in the OPV field, the majority of studies pertaining to ultrafast processes in cyanine-based OPVs have been focused on cyanine/C<sub>60</sub> bilayers.<sup>12</sup> More recently, however, evidence has shown that photocurrent generation can occur in a neat cyanine thin film in spite of the absence of a donor/acceptor interface.<sup>13</sup> Furthermore, the charges that are generated exhibit a long carrier lifetime as a result of reduced recombination, thus providing potential material design concepts for future photodiodes. Cyanine dyes have already been used in different photodiode designs because of their narrow-band absorption, ability to form J-aggregates and the possibility of tuning their absorption spectra for high absorption in the near-infrared.<sup>14–18</sup>

Previously, intrinsic photogeneration of charges has been seen in single layer SubNc and SubPc devices, where the charge generation was attributed to the high dielectric constant resulting in efficient screening thus allowing free carrier generation.<sup>19,20</sup> However, their performance is still limited, and so cyanine dyes could be used as a suitable alternative for single layer photodiodes.

## 3.2 Results and discussion

### 3.2.1 A comparison between solution and thin film

Initial thoughts on the charge generation process in neat pentamethine cyanine dyes focused on the role of H-aggregates, and in particular the impact they could have on the charge carrier lifetime. Therefore, it was first necessary to determine which spectral features arise due to aggregation. The first cyanine dye studied was 1,3,3-trimethyl-2-[5-(1,3,3-trimethyl-1,3-dihydro-indol-2-ylidene)-penta-1,3-dienyl]-3H-indolium hexafluorophosphate, which will from now on be referred to as Cy5-P. A solution and thin-film sample of Cy5-P were compared in order to determine the spectral characteristics arising due to aggregation of the Cy5 chromophore, the structure of which is shown in **figure 3.1**.

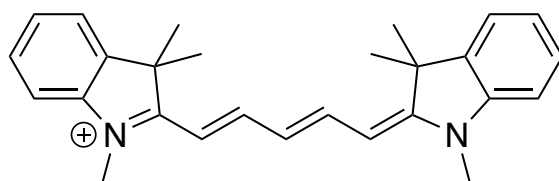


**Figure 3.1:** Structure of the Cy5 chromophore.

The normalised absorption spectra of the Cy5-P solution and thin film can be seen in **figure 3.2**. The sharp peak at around 640 nm in the solution spectrum corresponds to the Cy5 monomer (0,0) transition, whilst the shoulder peaks at wavelengths < 600 nm can be assigned to vibronic transitions.

In comparison, the absorption spectrum of the thin film shows two distinct peaks. The first of these, at 680 nm, corresponds to the Cy5 monomer and is red shifted as expected. The second peak, at 620 nm, is assigned to the absorption of the Cy5 dimer; this peak is broadened in the blue region due to higher order H-aggregates present in the film.<sup>21</sup> When comparing the steady state absorption spectrum with the absorption coefficient, as measured using ellipsometry, it is evident that there is little difference

(figure B.1). This allows us to conclude that reflectance and interference only represent minor contributions to the absorption spectrum.

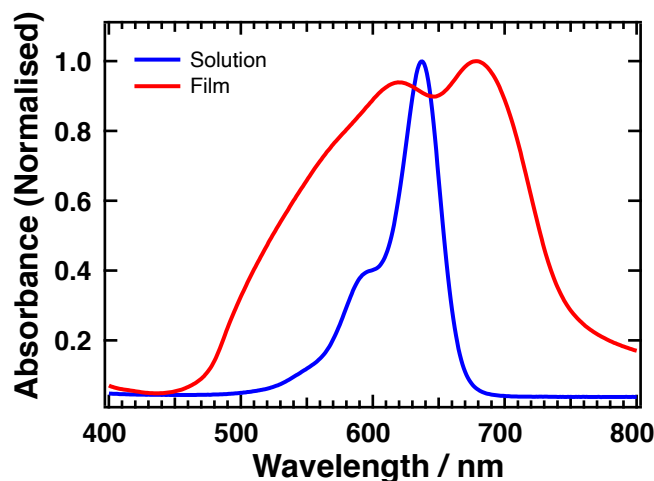


**Figure 3.2:** Absorption spectra of Cy5-P in acetonitrile (blue) and as a thin film (red).

Following on from the steady state absorption spectra, transient absorption (TA) spectra were measured for both the solution (**figure 3.3 a**) and the thin film (**figure 3.3 b**) with both samples being excited at 580 nm.

In the TA spectrum of the solution, four main features are present: two positive features at 450 and 500 nm, alongside two negative features at 540 – 615 nm and 650 nm. The two positive peaks can be assigned to the same species, as they show the same temporal dependence. Furthermore, they also exhibit no fluence dependence (**figure 3.3 c** and **figure B.2**), and so can be assigned to  $S_1 \rightarrow S_n$  transitions. This excited state absorption (ESA) feature is also similar to those that have been seen previously.<sup>22</sup> Previous studies have also shown the presence of another positive feature, appearing further into the red region, corresponding to trans-cis photoisomerisation occurring on a nanosecond timescale.<sup>23</sup> This is not present in these spectra, however, due to the shorter time window of the measurements. The broad negative band between 540 and 615 nm is assigned to the ground state bleaching (GSB), due to its resemblance to the steady state absorption spectrum. Finally, the feature at 650 nm is assigned to the

stimulated emission (SE).

Focusing now on the TA spectrum of the thin film, only three features are present. The two negative features, at 550 - 670 nm and 680 - 720 nm, can be assigned to the GSB of the H-dimer and a combination of the GSB and SE, respectively. The positive feature, unlike in the solution spectrum, consists of a single peak at 470 nm which also undergoes a red-shift over time (from 470 nm at 0.1 ps to 495 nm at 1000 ps). Furthermore, the kinetics of this feature are also different to that of the ESA feature seen in the solution spectrum.

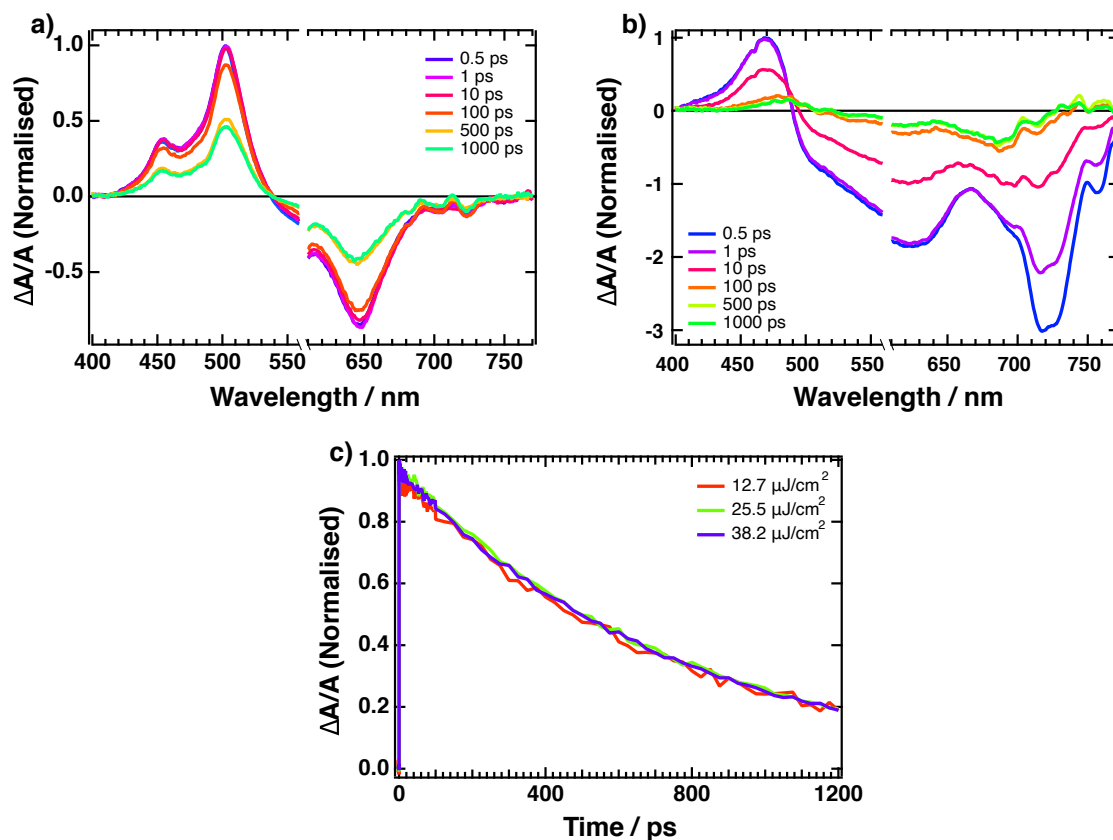


**Figure 3.3:** Transient absorption spectra of Cy5-P (a) in solution and (b) as a thin film. Samples were excited at 580 nm, and are normalised for ease of comparison. c) Kinetic traces, taken at 500 nm, of Cy5-P in solution measured at different fluences.



### 3.2.2 The search for oxidised species

Considering that the previously proposed mechanism for intrinsic charge generation in Cy5-P involved the generation of redox species, it was postulated that the single positive feature in the TA spectrum of the Cy5-P thin film could arise as a result of absorption from oxidised Cy5 chromophores.

In order to confirm this hypothesis, nitrosyl tetrafluoroborate ( $\text{NOBF}_4$ ) was used to oxidise Cy5-P in solution before spincoating to yield a thin film. The absorption spectrum of the film, shown in **figure 3.4**, shows a single peak at 470 nm which corresponds to the positive feature seen in the TA spectrum. After de-doping for several hours, the absorption spectrum of the Cy5 monomer reappears. Seeing as the film was spincoated from a 1:2.5 mol/mol solution of Cy5-P: $\text{NOBF}_4$  in acetonitrile, the large amount of salt present inhibits higher order Cy5 H-aggregates from forming, thus explaining the lack of peak broadening of the H-dimer peak after de-doping in air.

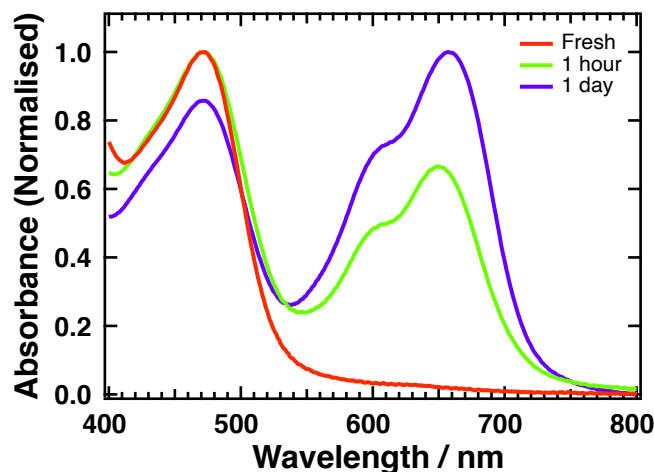


**Figure 3.4:** Absorption spectra of a thin film of Cy5-P: $\text{NOBF}_4$  1:2.5 mol/mol blend ratio at different times after sample preparation.

Therefore, due to its similarity to the peak present in the TA spectrum, we are tempted to assign this feature in the TA spectrum to oxidised monomer species ( $\text{Cy5}^+$ )

formed upon photoexcitation. However, previous studies on electrochemically reduced pentamethine cyanine dyes revealed similar spectra for the neutral and dicationic radicals and so we are unable to completely exclude the possibility of the positive feature arising from reduced cyanine chromophores ( $\text{Cy5}^-$ ).<sup>24</sup> Neutral cyanine radicals are unstable and promptly dimerise, which would explain why we are unable to see them in steady state measurements.

### 3.2.3 Impact of interchromophore distance

Having established the presence of redox cyanine chromophores upon photoexcitation, the next step was to explore the impact of the interchromophore distance on the charge generation process. To achieve this, polymethylmethacrylate (PMMA) was added to Cy5-P in various molar ratios and the steady state absorption spectra of the resulting films were measured.

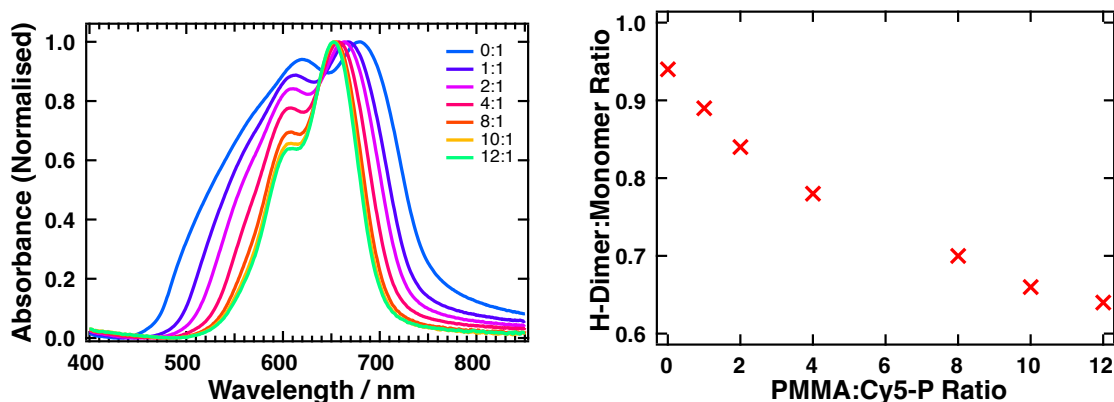


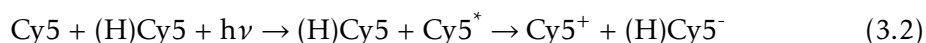
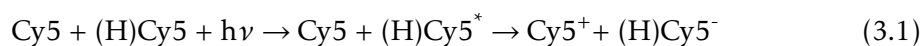
**Figure 3.5:** Normalised absorption spectra of varying ratios of PMMA:Cy5-P (left). Ratio of H-dimer:monomer peak height as a function of the PMMA:Cy5-P blend ratio (right).

As the proportion of PMMA increases (**figure 3.5**), there are three changes that occur to the absorption spectrum of the Cy5-P. Firstly, there is a blue shift in the Cy5 monomer peak. Secondly, there is a decrease in the H-dimer peak height. Finally, there is also a decrease in the broadening of the Cy5 H-dimer peak. These three changes are caused by a decrease in the degree of aggregation within the film.

From the TA spectra shown in **figure 3.6 a** and **figure B.3**, it is evident that as the proportion of PMMA in the PMMA: Cy5-P blend increases from 0:1 to 12:1 the positive feature transforms from one to two peaks, which corresponds to the singlet excited state absorption as observed previously in solution. This confirms that the single positive peak in the TA spectrum of a thin film of neat Cy5-P occurs when the chromophores are closely packed allowing for a charge transfer process to take place resulting in the generation of redox species. Global analysis was carried out, with the data being fitted with a bi-exponential function (**figure B.4**), yielding the decay associated spectra seen in **figures 3.6 b-e**. The first component, in red, corresponds to the decay of the excited state absorption, whilst the second component in blue can be assigned to the decay of the oxidised/reduced species following hole transfer from the aggregate excited state to a monomer in the ground state. As the proportion of PMMA increased, there is an increase in both of the time constants, and the rate constants for the different blends display a linear dependence with increasing proportion of PMMA (**figure 3.6 f**).

Since the charge transfer kinetics are very sensitive to the intermolecular distance between the donor and acceptor, these results allow us to confirm our hypothesis that the positive feature corresponds to photoinduced charge separation within the films. Furthermore, it is evident from the decay associated spectra that the charge transfer continues to occur in spite of the fact that the degree of aggregation is radically changed.

These results led us to propose two possible mechanisms for the intrinsic charge generation in Cy5-P, both of which involve H-aggregates. The first mechanism, shown in **equation 3.1**, involves direct excitation of H-aggregates into higher energy exciton bands, from which reductive quenching by the monomer species occurs.



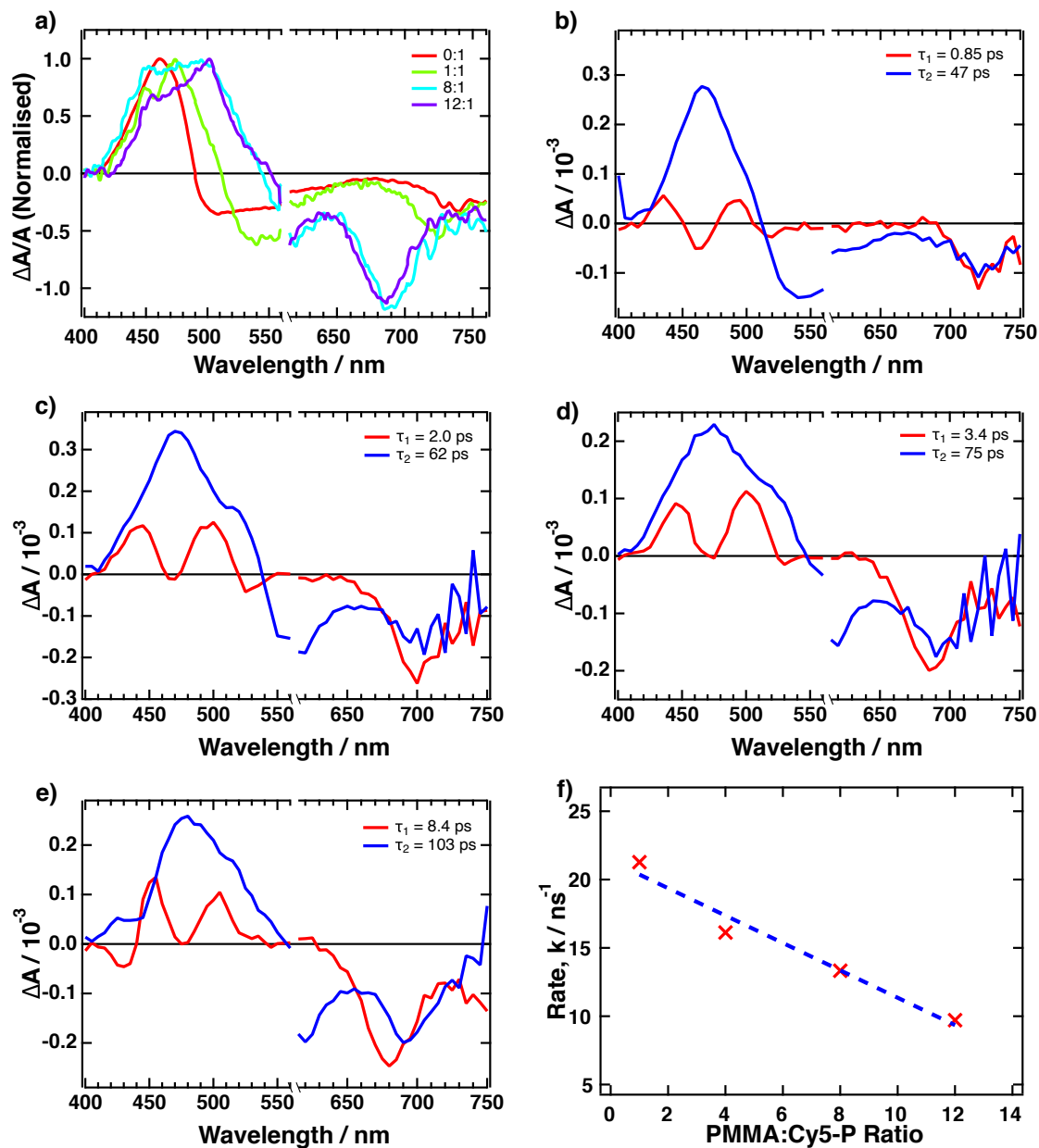


**Figure 3.6:** a) Normalised TA spectra for 0:1, 1:1, 8:1 and 12:1 blends of PMMA:Cy5-P taken at a time of 1 ps. Samples were excited at 580 nm with a fluence of  $30 \mu\text{J cm}^{-2}$ . (b)-(e) Global fits for different PMMA:Cy5-P blends (1:1, 4:1, 8:1 and 12:1). (f) Plot showing the rate of electron transfer as a function of PMMA:Cy5-P blend ratio.

The other possibility is that the charge transfer can proceed via electron transfer from the photoexcited monomer species (**equation 3.2**). Both of these symmetry-breaking charge separation mechanisms involve H-aggregates and result in the formation of the redox species that we see as the positive feature at 470 nm in the TA spectrum. H-aggregates play a vital role in the charge generation process, as they ensure the necessary symmetry-breaking and the thermodynamic driving force to yield the charge separated pair. Upon the formation of H-aggregates, the anions are situated outside of the positively charged stack, giving rise to a local electric field which lowers the energy levels of the H-aggregates with respect to those of the Cy5 monomers.

After undergoing charge separation onto well separated sites, the positively charged hole is shielded from recombination by the negatively charged anions which surround the aggregates. One would expect this to lead to an increase in the charge carrier lifetime, as reported previously.<sup>13</sup> However, this long charge carrier lifetime is not seen in these measurements as a result of a much larger concentration of charge carriers produced at the laser excitation intensity, resulting in increased bimolecular charge recombination.

### 3.2.4 Changing the counterion

Having determined the presence of aggregate oxidised species within the photoexcited film and elucidated the charge transfer process, the impact of the counterion on the charge generation process was subsequently investigated.

Alongside the original hexafluorophosphate anion (Cy5-P), three other counterions were studied in combination with the same cationic chromophore: chloride (Cy5-Cl), tetrakis(nonafluoro-tert-butoxy)aluminate (Cy5-[Al(pftb)<sub>4</sub>]) and tetrakis(perfluoro-1-adamantoxy)aluminate (Cy5-[Al(pfad)<sub>4</sub>]). The structure of the four counterions are shown in **figure 3.7**, and their volume increases from 0.029 nm<sup>3</sup> for the chloride counterion up to 1.194 nm<sup>3</sup> for the largest [Al(pfad)<sub>4</sub>] counterion.

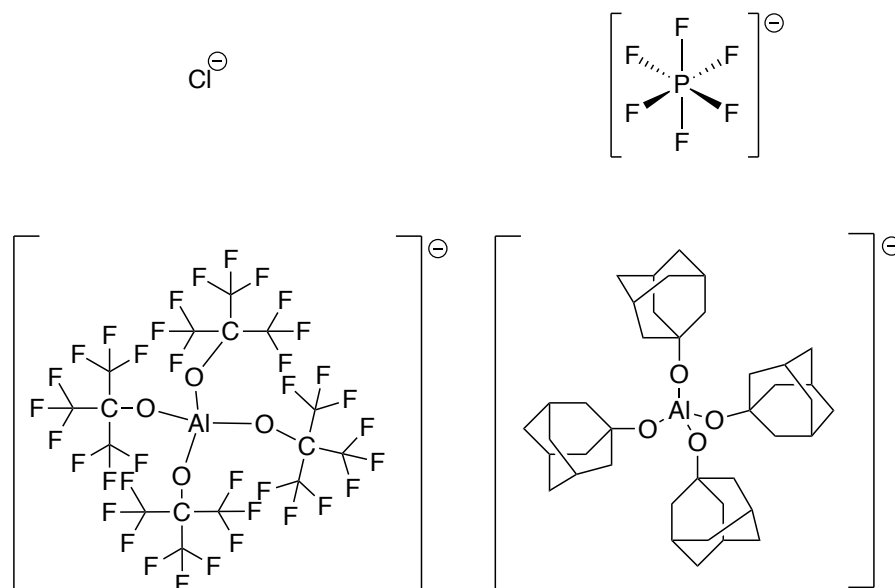


**Figure 3.7:** Structures of the different counterions:  $\text{Cl}^-$ ,  $\text{PF}_6^-$ ,  $[\text{Al}(\text{pftb})_4]^-$  (left) and  $[\text{Al}(\text{pfad})_4]^-$  (right).

Hirshfeld analysis was conducted on the crystal structures of the different Cy5 dyes in order to generate potential surfaces of the dyes.<sup>25</sup> These were in turn used to generate the fingerprint plots shown in **figure B.5**.<sup>26</sup>

Fingerprint plots show the different distances of inter- and intra-molecular contacts, as well as the distribution of the distances. From these plots, it is evident that as the anion size increases the mean inter-chromophore distance increases. In addition, the dominating H-H cation-cation intermolecular contacts in Cy5-P (accounting for 51.7% of the intermolecular interactions) are replaced by other inter-molecular interactions as the anion size increases, evidenced by the H-H cation-cation intermolecular contacts only accounting for 13.6% of the contacts in the largest Cy5- $[\text{Al}(\text{pfad})_4]$  dye.

This increase in inter-chromophore distance results in a decrease in the degree of aggregation within the film. This is evident from the steady state absorption spectra (**figure 3.8 a**), where we see a blue shift in the Cy5 monomer peak, as well as a decrease in the ratio of the H-dimer:monomer peak height and a reduced full width at half maximum (FWHM) upon an increase in anion size.

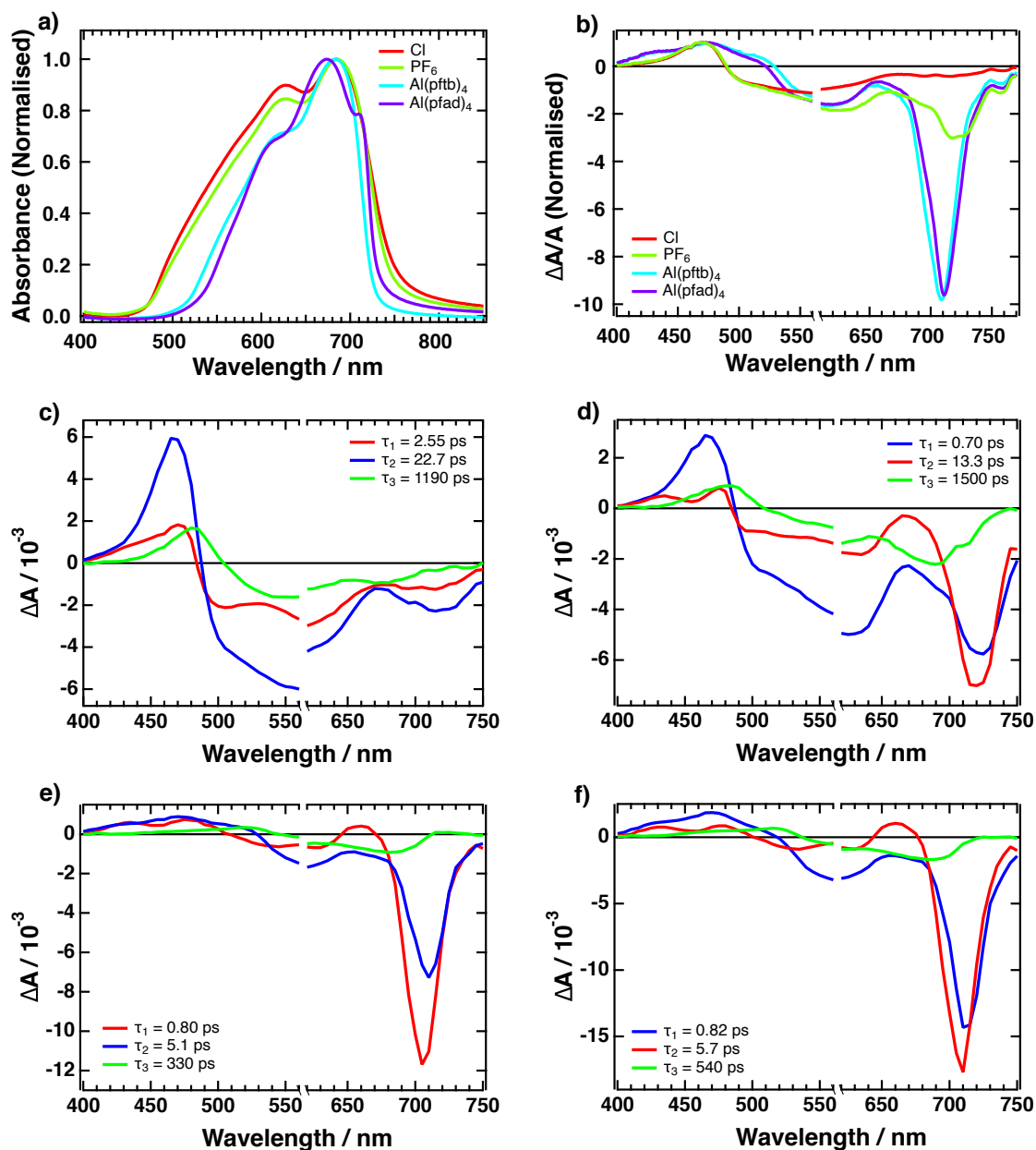


**Figure 3.8:** (a) Normalised absorption spectra and (b) normalised transient absorption spectra of Cy5 thin films incorporating different counterions. (c)-(f) Global fits for Cy5 thin films incorporating different counterions (Cl<sup>-</sup>, PF<sub>6</sub><sup>-</sup>, [Al(pftb)<sub>4</sub>]<sup>-</sup> and [Al(pfad)<sub>4</sub>]<sup>-</sup>).

The anion size also has a notable impact upon the TA spectra (**figure 3.8 b**). With increasing anion size, there is an increase in the relative intensity of the stimulated emission which is caused by a decrease in energetic disorder thus leading to a decrease in self quenching.<sup>27</sup> Such an increase is also seen in the steady state photoluminescence spectra (**figure B.6**). Furthermore, as the anion size increases, there is a slight shift in the positive feature at 470 nm, and a second peak begins to be resolved. This can be explained by a diminishing contribution of the H-aggregates, and reflects the results obtained for the PMMA:Cy5 blends. The fabricated thin films were reproducible, with the absorption spectra being identical between batches. Therefore, we can conclude that any differences in the photophysics between the dyes incorporating the different counterions are due to differences in aggregation, and not due to any structural defects that may occur during film formation.

Global analysis was once again conducted on the TA spectra, with the data being fitted with a tri-exponential function (**figure B.7**) yielding the decay associated spectra shown in **figures 3.8 c-f**; these spectra allowed us to estimate the quantum yield for the charge separation process in each of the dyes. A tri-exponential function was used as there are three components which contribute to the TA spectrum. As before, the first two components correspond to the decay of the excited state absorption (in red) and the decay of the oxidised/reduced Cy5 chromophore (in blue). The final component, in green, can be assigned to the recombination of the separated charges. In order to estimate the quantum yield of the charge separation process, the area beneath the positive feature of the curve for the red and blue components,  $A_r$  and  $A_b$ , was found and divided by the extinction coefficients of the Cy5 chromophore and the oxidised chromophore, respectively. This gives the following expression for the quantum yield:

$$\text{Quantum Yield (\%)} = \frac{\frac{A_b}{\epsilon_{ox}}}{\frac{A_r}{\epsilon_{ch}} + \frac{A_b}{\epsilon_{ox}}} \quad (3.3)$$

where  $\epsilon_{ch}$  and  $\epsilon_{ox}$  are the extinction coefficients of the Cy5 chromophore and its oxidised chromophore, respectively. The extinction coefficient of the Cy5 chromophore was taken as  $2.1 \times 10^5 \text{ L mol}^{-1} \text{ cm}^{-1}$ . The extinction coefficient of the oxidised species



was estimated from the oxidation experiments with  $\text{NOBF}_4$ , where it was found that the extinction coefficient was  $\sim 52\%$  of that of the Cy5-P dye in the ground state. This gives an extinction coefficient of  $\sim 1.1 \times 10^5 \text{ L mol}^{-1} \text{ cm}^{-1}$  for the purpose of the quantum yield calculation.

The quantum yield of the charge separation process was found to be 83% and 86% for the Cy5-Cl and Cy5-P systems, respectively. The yield then decreases to 71% and 78% for the two aluminium-based analogues Cy5-[Al(pftb)<sub>4</sub>] and Cy5-[Al(pfad)<sub>4</sub>]. This decrease in yield for the larger counterions further confirms that the interchromophore distance, and as a consequence the degree of aggregation, plays a key role in the intrinsic charge generation process. In the films with the larger counterions, the counterions are sufficiently large to ensure that higher order H-aggregates do not readily form which leads to a reduction in electron transfer from photo-excited monomer chromophores to the aggregates.

### 3.2.5 Charge transport

The final part of this chapter focuses on the impact of anion size on charge transport within neat pentamethine cyanine dyes. In order to achieve this, electroabsorption and time-resolved electroabsorption spectroscopy (TREAS) were used.

The electroabsorption spectra of the Cy5 dyes incorporating the different counterions all display similar shapes (**figure 3.9**), although there is a clear red shift in the positive feature from 475 nm to 550 nm as the anions increase in size from  $\text{Cl}^-$  to  $[\text{Al}(\text{pfad})_4]^-$ . As the shape of the electroabsorption spectrum is directly related to the derivative of the absorption spectrum, this red shift arises from a decrease in higher order H-aggregates upon increasing anion size.

The electroabsorption spectra were fitted with a linear combination of the zeroth, first and second derivative of the absorption spectrum of each dye. The accuracy of the fit is determined by the number of transitions behind each absorption band. The fits (**figure B.8**) for the Cy5-Cl and Cy5-P dyes are reasonably accurate. However, the fits

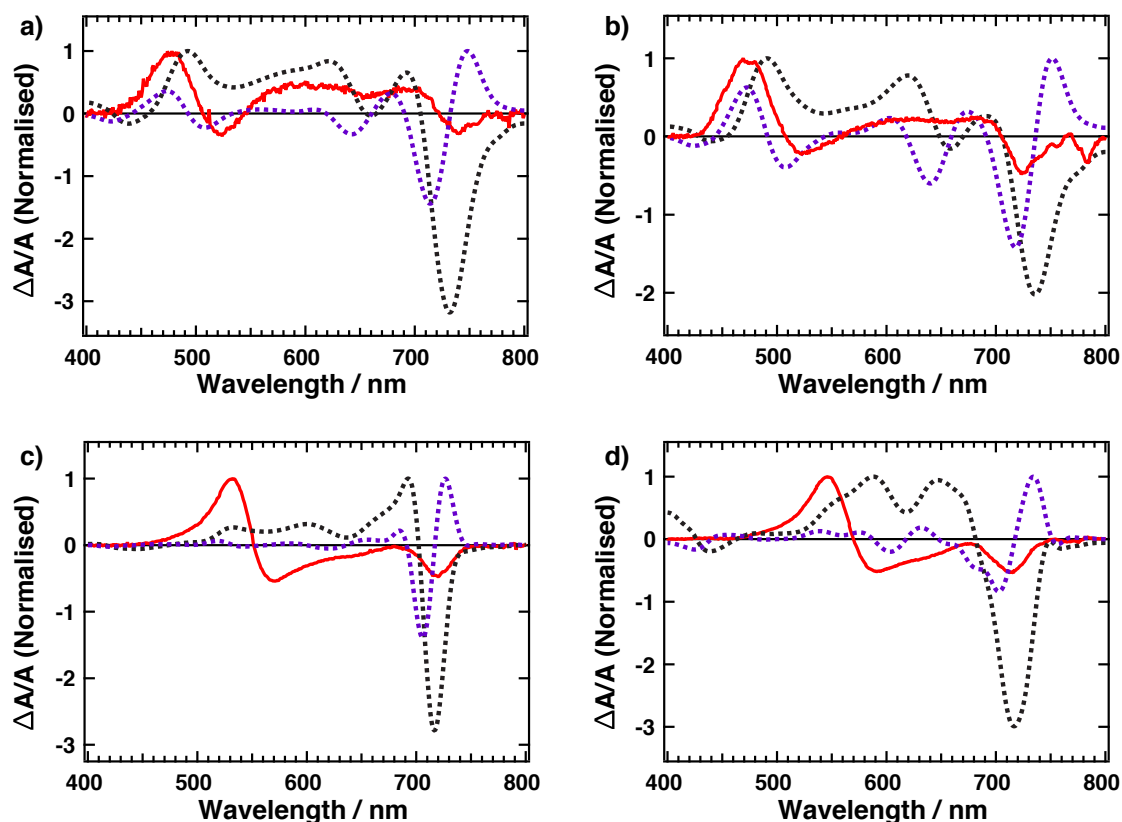


**Figure 3.9:** Electroabsorption spectra (red) alongside the first and second derivatives of the absorbance spectra (dashed black and purple lines, respectively) of Cy5 thin films incorporating different counterions: (a)  $\text{Cl}^-$ , (b)  $\text{PF}_6^-$ , (c)  $[\text{Al}(\text{pftb})_4]^-$  and (d)  $[\text{Al}(\text{pfad})_4]^-$ .

for the Al-based analogues are inaccurate, which implies that in the two films incorporating the larger anions there is inhomogeneity in the polarisability and the permanent dipoles on a short length scale (tens of nm) and that the film is locally disordered. Furthermore, any aggregates that are present in these films do not exhibit uniform properties.<sup>28</sup>

The results from the TREAS measurements, which were carried out to determine the mobility in each dye, proved inconclusive. This is because of the poor carrier mobility in the cyanine dyes resulting in there being minimal evolution in the electroabsorption spectra over the time window of the measurement (approximately 1.2 ns). This issue could possibly be overcome by decreasing the layer thickness or increasing the voltage;

however, as the films were already very thin (20-50 nm) and high voltages leave the samples susceptible to short-circuits, neither of these solutions were feasible in this scenario. Therefore, time-of-flight was used instead.

Due to issues with sample preparation for the Cy5-[Al(pfad)<sub>4</sub>] dye, only the mobility of the Cy5-Cl, Cy5-P and Cy5-[Al(pftb)<sub>4</sub>] dyes were investigated. The samples, consisting of a glass/FTO/Al<sub>2</sub>O<sub>3</sub>/Cy5-X/Al structure, were excited at 630 nm with an applied voltage of 8 V yielding a photocurrent curve for each sample (**figure B.9**). By constructing asymptotes on the graphs, it was possible to estimate the transit time, whereby the intersection of the asymptotes corresponds to the transit time.<sup>29</sup> This was used, alongside the sample thickness determined by cross-sectional scanning electron microscopy (SEM) (**figure 3.10** and **figure B.10**), to calculate the carrier mobility of each dye:

$$\mu = \frac{d^2}{E \cdot t_{tr}} \quad (3.4)$$

where  $d$  is the sample thickness,  $E$  the voltage applied across the sample and  $t_{tr}$  the transit time.

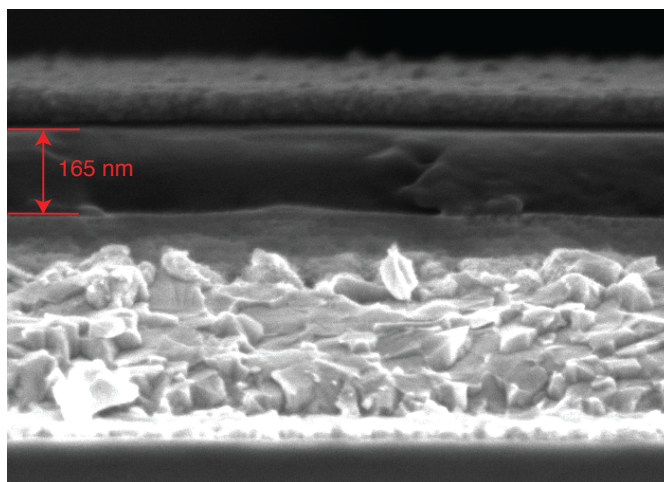


**Figure 3.10:** Cross-sectional SEM image of a Cy5-[Al(pftb)<sub>4</sub>] TOF sample, with the Cy5-[Al(pftb)<sub>4</sub>] layer marked in red.

As evident from **Table 3.1**, the mobility values are reasonably similar irrespective of counterion size, and are similar to those found in other organic salt photovoltaic systems.<sup>2</sup> This is an interesting result as one would expect there to be a decrease in mobility with increasing anion size as a result of the chromophores being further apart, thus reducing the rate of charge hopping.

**Table 3.1:** Transit times and mobility values for different Cy5-X salts

Anion	Transit Time / $\mu\text{s}$	Mobility / $10^{-6} \text{ cm}^2 \text{ V}^{-1} \text{ s}^{-1}$	Thickness / nm
$\text{Cl}^-$	$2.47 \pm 0.04$	$6.12 \pm 0.09$	110
$\text{PF}_6^-$	$2.75 \pm 0.13$	$3.69 \pm 0.18$	90
$\text{Al(pftb)}_4^-$	$5.92 \pm 0.30$	$5.75 \pm 0.29$	165

However, whilst the average interchromophore distance increases with increasing anion size and the percentage of interacting cation-cation surfaces is reduced by a factor of 4 (from 51.7 to 13.6%), the sections of cation that allow charge transfer remain intact. As a result, even with the largest anions, it is not possible to completely break the interaction paths across the entire film. Therefore, we can conclude that the carrier mobility of the dyes with the larger anions are similar to that of the dyes incorporating smaller counterions, as the larger inter-chromophore distance is mitigated by the decrease in the degree of aggregation and subsequent minimisation of charge trapping by H-aggregates. Due to limitations with sample preparation, it was not possible to conclusively determine the transport regime (dispersive vs. non-dispersive) as it was difficult to get a sufficiently thick active layer. This also results in a certain amount of uncertainty with regard to the mobility values found. However, whilst the absolute values may not be correct, we believe that the mobility values of the three cyanine dyes tested are similar and so the conclusions drawn remain valid.

### 3.3 Conclusion

Here it has been shown, using transient absorption spectroscopy, that photogeneration of oxidised Cy5 monomer species can occur in cyanine dyes incorporating small counterions such as chloride or hexafluorophosphate. This has allowed us to confirm the charge generation mechanism in these materials, providing the first direct proof of high efficiency intrinsic charge generation in organic salt semiconductors. There are two possible mechanisms: the first proceeds via photoexcitation of monomer species followed by electron transfer to ground state aggregated chromophores, whilst the second involves direct excitation of H-aggregates followed by reductive quenching by the monomer species. The charge transfer process in these dyes can occur with a yield of up to 86%. The involvement of H-aggregates is vital, as they ensure the necessary symmetry breaking and provide the thermodynamic driving force for the charge transfer process. The impact of the counterion size on the charge transfer process was then determined, with two large aluminium based counterions,  $[\text{Al}(\text{pftb})_4]^-$  and  $[\text{Al}(\text{pfad})_4]^-$ , being studied alongside the chloride and hexafluorophosphate anions. Both steady state and transient absorption measurements demonstrated that monomer oxidised species were present to a lesser extent in the samples containing the two larger anions as well as in measurements where the cyanine dye was diluted in PMMA. These results allowed us to conclude that in pentamethine cyanine dyes, where the dye is sufficiently large, higher order H-aggregates are not present in high concentration due to the spatial separation of the Cy5 chromophores, thus diminishing the process of charge generation. However, despite this increase in spatial separation, time-of-flight measurements showed that the carrier mobility remains similar irrespective of the counterion used. This is because the increased interchromophore distance, which one would expect to lead to a reduction in the charge carrier mobility, is counterbalanced by the decrease in charge trapping due to the suppression of H-aggregates.

### 3.4 Sample preparation and experimental methods

The cyanine dyes 1,3,3-trimethyl-2-[5-(1,3,3-trimethyl-1,3-dihydro-indol-2-ylidene)-penta-1,3-dienyl]-3H-indolium chloride and its hexafluorophosphate analogue were purchased from FEW chemicals, Germany. The tetrakis(nonafluorotertbutoxy)aluminate and tetrakis(perfluoro-1-adamantoxy)aluminate analogues were synthesised and provided by the group of Prof. Ingo Krossing (University of Freiburg, Germany).

Solutions of Cy5-Cl and Cy5-P were prepared by dissolving the dye in acetonitrile (8 mg/mL), whilst the two Al-based analogues were prepared by dissolving the dyes in ethanol (8 mg/mL).

Thin films for TAS were prepared by spincoating the prepared solutions of Cy5-X dyes onto cleaned glass substrates at 6000 rpm for 60 s inside a glovebox.

Samples for EDA and TREAS were prepared on FTO-patterned glass. Spincoating aluminium sec-butoxide (0.25 M) in 2-methoxyethanol, burning at 500 °C for 1 hour, and repeating 3 times yielded a 30 nm thick Al<sub>2</sub>O<sub>3</sub> insulating layer. The cyanine dyes were then deposited as mentioned above, followed by thermal deposition of an aluminium top electrode.

Samples for time-of-flight were also prepared on FTO patterned glass substrates with 6 layers of alumina prepared as above. The cyanine dyes were deposited by spincoating the Cy5-X solutions at 2000 rpm for 60 s.

Thin film thickness was determined using both ellipsometry (J.A. Woollam M2000-VI) and cross-sectional SEM (Zeiss Merlin).



## References

- (1) G. C. Fish, J. M. Moreno-Naranjo, A. Billion, D. Kratzert, E. Hack, I. Krossing, F. Nüesch and J. E. Moser, *Phys. Chem. Chem. Phys.*, 2021, **23**, 23886–23895.
- (2) M. Bates and R. R. Lunt, *Sustain. Energy Fuels*, 2017, **1**, 955–968.
- (3) R. Hany, B. Fan, F. A. De Castro, J. Heier, W. Kylberg and F. Nüesch, *Prog. Photovolt: Res. Appl.*, 2011, **19**, 851–857.
- (4) B. Siegmund, M. T. Sajjad, J. Widmer, D. Ray, C. Koerner, M. Riede, K. Leo, I. D. Samuel and K. Vandewal, *Adv. Mater.*, 2017, **29**, 3–7.
- (5) J. J. M. Halls, C. A. Walsh, N. C. Greenham, E. A. Marseglia, R. H. Friend, S. C. Moratti and A. B. Holmes, *Nature*, 1995, **376**, 498–500.
- (6) D. Gesevičius, A. Neels, S. Jenatsch, E. Hack, L. Viani, S. Athanasopoulos, F. Nüesch and J. Heier, *Adv. Sci.*, 2018, **5**, 1700496.
- (7) D. Gesevičius, A. Neels, S. Yakunin, E. Hack, M. V. Kovalenko, F. Nüesch and J. Heier, *ChemPhysChem*, 2018, **19**, 3356–3363.
- (8) F. Nüesch, A. Faes, L. Zuppiroli, F. Meng, K. Chen and H. Tian, *J. Mater. Sci.*, 2005, **40**, 1353–1357.
- (9) O. Malinkiewicz, T. Grancha, A. Molina-Ontoria, A. Soriano, H. Brine and H. J. Bolink, *Adv. Energy Mater.*, 2013, **3**, 472–477.
- (10) Z. Huang, D. Ji, S. Wang, A. Xia, F. Koberling, M. Patting and R. Erdmann, *J. Phys. Chem. A*, 2006, **110**, 45–50.
- (11) C. A. Guarín, J. P. Villabona-Monsalve, R. López-Arteaga and J. Peon, *J. Phys. Chem. B*, 2013, **117**, 7352–7362.

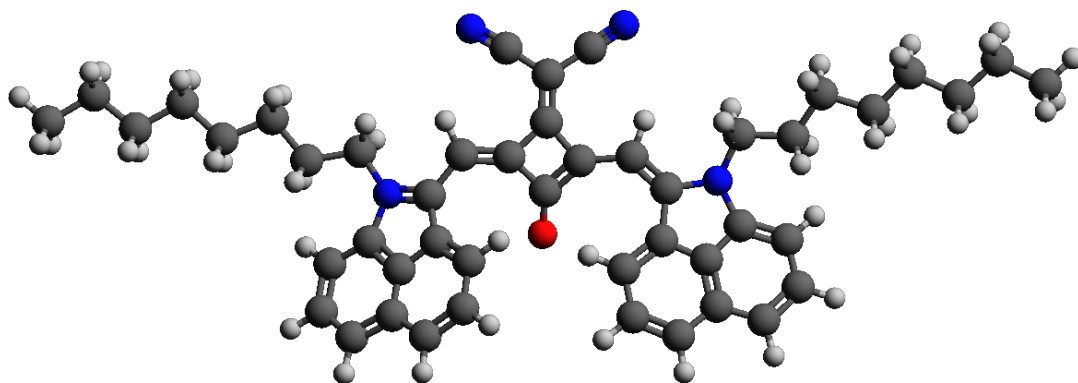
- (12) A. Devižis, J. De Jonghe-Risse, R. Hany, F. Nüesch, S. Jenatsch, V. Gulbinas and J. E. Moser, *J. Am. Chem. Soc.*, 2015, **137**, 8192–8198.
- (13) L. Wang, S. Jenatsch, B. Ruhstaller, C. Hinderling, D. Gesevičius, R. Hany and F. Nüesch, *Adv. Funct. Mater.*, 2018, **28**, 1705724.
- (14) M. Young, J. Suddard-Bangsund, T. J. Patrick, N. Pajares, C. J. Traverse, M. C. Barr, S. Y. Lunt and R. R. Lunt, *Adv. Opt. Mater.*, 2016, **4**, 1028–1033.
- (15) Y. Yang, S. Omi, R. Goto, M. Yahiro, M. Era, H. Watanabe and Y. Oki, *Org. Electron.*, 2011, **12**, 405–410.
- (16) T. P. Osedach, A. Iacchetti, R. R. Lunt, T. L. Andrew, P. R. Brown, G. M. Akselrod and V. Bulović, *Appl. Phys. Lett.*, 2012, **101**, 113303.
- (17) Y. Yang, T. Nakamichi, H. Yoshioka, M. Yahiro, M. Era, H. Watanabe, Y. Cui, Y. Oki and G. Qian, *J. Mater. Chem. C*, 2013, **1**, 1739–1744.
- (18) S. B. Anantharaman, K. Strassel, M. Diethelm, A. Gubicza, E. Hack, R. Hany, F. A. Nüesch and J. Heier, *J. Mater. Chem. C*, 2019, **7**, 14639–14650.
- (19) H. T. Chandran, T. W. Ng, Y. Foo, H. W. Li, J. Qing, X. K. Liu, C. Y. Chan, F. L. Wong, J. A. Zapien, S. W. Tsang, M. F. Lo and C. S. Lee, *Adv. Mater.*, 2017, **29**, 1606909.
- (20) W. Li, D. Li, G. Dong, L. Duan, J. Sun, D. Zhang and L. Wang, *Laser Photonics Rev.*, 2016, **10**, 473–480.
- (21) E. N. Kaliteevskaya, V. P. Krutyakova, T. K. Razumova and A. A. Starovoitov, *Opt. Spectrosc.*, 2016, **120**, 482–491.
- (22) S. Chatterjee, B. Sauerwein, X. Yang, G. B. Schuster, P. D. Davis, P. Gottschalk and M. E. Kurz, *J. Am. Chem. Soc.*, 1990, **112**, 6329–6338.
- (23) Z. Huang, D. Ji, S. Wang, A. Xia, F. Koberling, M. Patting and R. Erdmann, *J. Phys. Chem. A*, 2006, **110**, 45–50.
- (24) J. R. Lenhard and A. D. Cameron, *J. Phys. Chem.*, 1993, **97**, 4916–4925.
- (25) M. A. Spackman and D. Jayatilaka, *CrystEngComm*, 2009, **11**, 19–32.
- (26) M. A. Spackman and J. J. McKinnon, *CrystEngComm*, 2002, **4**, 378–392.



- (27) D. Oelkrug, H. J. Egelhaaf, J. Gierschner and A. Tompert, *Synth. Met.*, 1996, **76**, 249–253.
- (28) A. Chowdhury, S. Wachsmann-Hogiu, P. R. Bangal, I. Raheem and L. A. Peteanu, *J. Phys. Chem. B*, 2001, **105**, 12196–12201.
- (29) N. A. Mica, S. A. Thomson and I. D. Samuel, *Org. Electron.*, 2018, **63**, 415–420.



## 4 Charge separation processes in squaraine dyes and spiro-OMeTAD



In the previous chapter, intrinsic photoinduced charge generation proceeding via a symmetry-breaking process was evidenced in neat cyanine dye thin films. The first part of this chapter focuses on whether such a symmetry-breaking charge separation (SB-CS) process could occur in other materials such as neat squaraine dye thin films. Steady state and ultrafast transient absorption techniques were used to probe the impact of sample preparation and aggregation on the photogenerated species in neat squaraine dye thin films and to determine if redox species were generated after photoexcitation. Following this, the transient spectra of squaraine/C<sub>60</sub> bilayers were recorded to conclusively determine that intrinsic charge generation is not possible in the neat squaraine dyes studied.

The second part of this chapter is focused on the photochemistry of spiro-OMeTAD, a material which has been used extensively in solid state DSSCs as well as perovskite photovoltaics. TAS was used to determine that oxidised spiro-OMeTAD is formed upon photoexcitation, even in the absence of metal-TFSI additives, as a result of a SB-CS process.

## 4.1 Introduction

Squaraine dyes were first synthesised in 1965<sup>1</sup> as a result of a condensation reaction between pyrrole and squaric acid, and their general structure consists of an electron deficient aromatic squaric acid core with two aromatic electron donating groups at opposite sides of the 4-membered ring.<sup>2</sup> This gives them a donor-acceptor-donor form thus yielding a zwitterionic structure. This structure results in squaraine dyes having a strong absorption in the visible to near infrared region (with extinction coefficients typically exceeding 10<sup>5</sup> L mol<sup>-1</sup>cm<sup>-1</sup>).<sup>3</sup>

Like cyanine dyes, it is also possible to tune the optical properties of squaraine dyes enabling them to be used to good effect in organic solar cells<sup>4</sup> and as light sensitisers in DSSCs.<sup>5,6</sup> The two aromatic groups can be altered and it is also possible to modify the squaric core via nucleophilic substitution of a dicyanomethylene group, resulting

in dicyanomethylene squaraine (DCSQ) dyes (**figure 4.1**). Here, the addition of the dicyanomethylene group leads to a red shift in the absorption spectrum of the dye, due to it being locked in the *cis* conformation.<sup>7</sup>

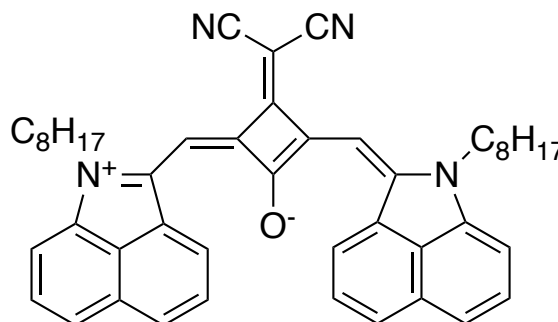


**Figure 4.1:** Structure of the DCSQ1 dye which is locked in the *cis* conformation.

Outside of the field of photovoltaics, squaraine dyes have also been utilised in light-emitting diodes,<sup>8,9</sup> for bio-imaging<sup>10</sup> and as short-wave infrared (SWIR) upconverters.<sup>11</sup> There is a demand for organic based SWIR devices for a variety of applications, as they are a more economical option when compared to the current indium gallium arsenide (InGaAs) photodetectors.<sup>12</sup>

With respect to studying the photophysics of squaraine dyes, previous studies have focused on investigating fluorescence lifetimes in squaraine polymer films,<sup>13</sup> studying the role of squaraine dyes in singlet oxygen production and removal<sup>14</sup> and exploring the excited state photophysics of squaraine dyes.<sup>15,16</sup> If intrinsic charge generation were to be possible in neat squaraine thin films, it would have important design implications for future SWIR photodiodes and OPV applications.

The second part of this chapter is focused on the organic hole transporting material 2,2',7,7'-tetrakis (N,N-di(4-methoxyphenylamine))-9,9'-spirobifluorene, more commonly known as spiro-OMeTAD. Initially used as a hole transporting material (HTM) in solid state DSSCs,<sup>17</sup> it has since been exploited in perovskite solar cells where its inclusion led to improved device efficiency and stability.<sup>18,19</sup> To alleviate the issue of poor hole mobility, lithium bis(trifluoromethanesulfonyl)imide (LiTFSI) is often added

alongside 4-(*tert*-butyl pyridine), tBP, to improve device efficiency via p-doping. However, the increase in efficiency is accompanied with a decrease in device stability as the additives lead to degradation of the perovskite layer.<sup>20</sup>

In spite of their almost universal inclusion in high efficiency perovskite solar cells,<sup>21,22</sup> the role of additives/dopants on the spiro-OMeTAD HTM is not fully understood; furthermore, surprisingly little work has been undertaken to explore the photophysics of the spiro-OMeTAD itself. It is thought that the lithium cations promote p-doping of the spiro-OMeTAD by oxygen, ensuring a high conductivity via trap-filling,<sup>23,24</sup> whilst tBP aides in the morphological control of the spiro-OMeTAD layer.<sup>25–27</sup> Due to their impact on the stability, it is necessary to find other additive materials which can have a similar p-doping effect whilst having less of a detrimental impact on the device stability.<sup>28–30</sup>

## 4.2 Results and discussion

The squaraine dye studied in this chapter, DCSQ1, is a dicyanomethylene substituted squaraine dye and its structure is shown in **figure 4.1**. The first results presented here are focused on characterising thin films of DCSQ1 using steady state absorption in order to determine their morphology, as well as factors which impact the morphology as this could play a key role in any potential intrinsic charge generation process.

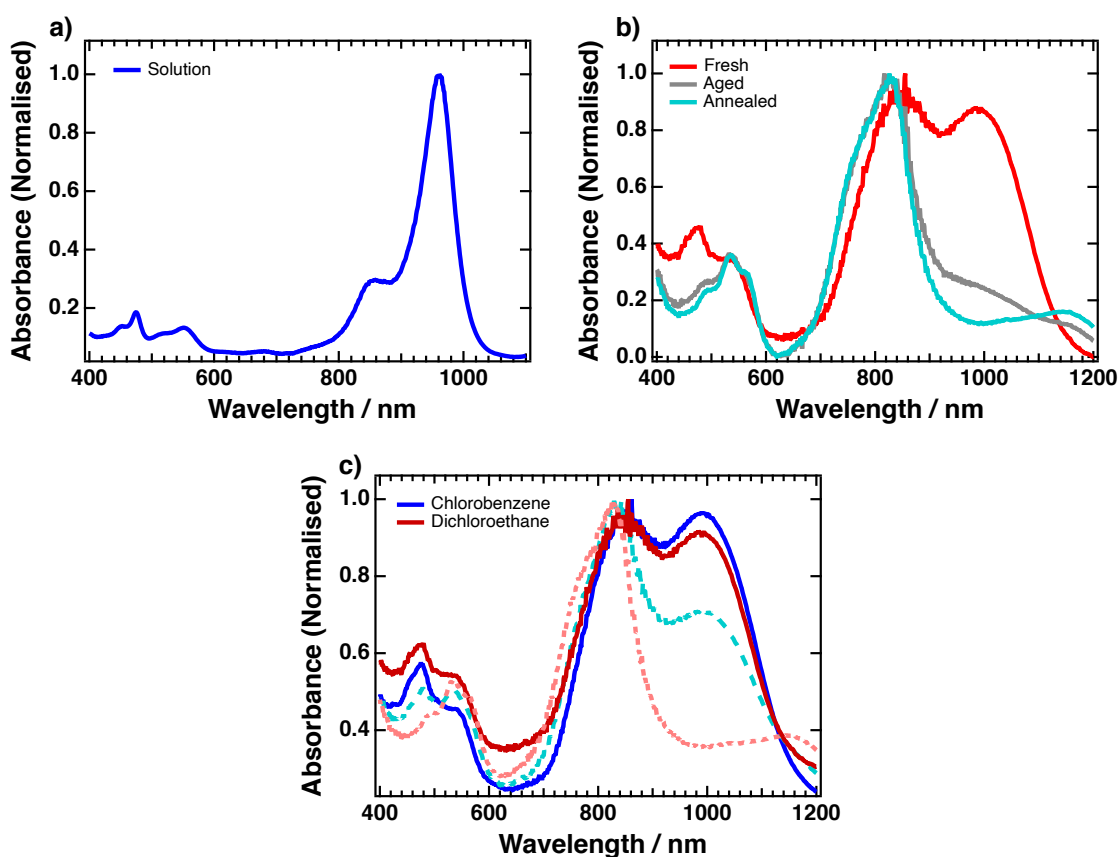


**Figure 4.2:** Absorption spectrum of DCSQ1 (a) in solution and (b) as a fresh thin film, after ageing and after annealing. Thin films were spincast from solutions of chlorobenzene. (c) Comparison of solvent choice on the absorption spectrum. Films were spincast from solutions of chlorobenzene and dichloroethane with (dashed line) and without (solid line) annealing.

The solution spectrum of DCSQ1 (**figure 4.2 a**) shows a main peak at 960 nm which can be assigned to the (0,0) transition. The shoulder, appearing at 855 nm, corresponds to a vibronic transition and is characteristic of squaraine dyes in solution.<sup>31</sup> Furthermore, the small peaks appearing between 450 and 600 nm can be assigned to higher order HOMO  $\rightarrow$  LUMO+1 transitions.<sup>11</sup> In comparison, the absorption spectrum of the neat DCSQ1 thin film has two main peaks at 995 and 845 nm which can be assigned to the DCSQ1 monomer and H-aggregates, respectively.<sup>32</sup> Once again the smaller peaks between 400 and 600 nm can be assigned to higher order transitions.

Annealing the film at 70 °C for 15 minutes resulted in a decrease in the amplitude of the DCSQ1 monomer peak relative to that of the H-aggregate peak; a similar effect is also seen when the film was left in ambient air, with the amplitude of the monomer peak steadily decreasing over a period of tens of hours. This allows us to conclude that H-aggregates are the thermodynamically stable form of DCSQ1.

As well as annealing, other aspects of sample preparation can be used to alter the degree of H-aggregation within the film. For example, by changing the solvent from dichloroethane (DCE) to chlorobenzene (CB) it is possible to further increase the population of H-aggregates relative to the monomer (**figure 4.2 c**).

#### 4.2.1 Understanding the transient absorption spectrum

Having acquired the steady state absorption spectra and understood the impact of solvent choice and annealing/ageing on the degree of aggregation within the film, TAS was conducted on the DCSQ1 thin film sample. As previously mentioned in the "Experimental methods" section, it is possible for the detectors to be operating either in the visible (400 - 770 nm) or the near-infrared (850 - 1050 nm). To change between the two measurement regions, the grating for the detectors along with the bandpass filters need to be changed; the result is that by combining two TAS measurements it was possible to obtain the complete TA spectrum of the DCSQ1 thin film from 400 - 1050 nm which is shown in **figure 4.3**.



The TA spectrum has three main features: two negative features, the first centred at 550 nm and the second ranging from 850 to over 1050 nm, alongside a broad positive feature from 570 to 750 nm. Due to its resemblance to the steady state absorption spectrum, the broad negative band from 850 to over 1050 nm can be assigned to the ground state bleaching of the monomer. This feature would also be expected to overlap with bleaching from the H-aggregates, with the overall GSB extending down to 750 nm. The other negative peak, centred at 550 nm, corresponds to bleaching occurring as a result of  $S_0 \rightarrow S_2$  transitions. Given that this squaraine dye is a potential candidate for intrinsic charge generation, we postulated that the broad positive feature could correspond to the formation of oxidised chromophore species, similar to what was seen in the TA spectrum of the Cy5 thin films.

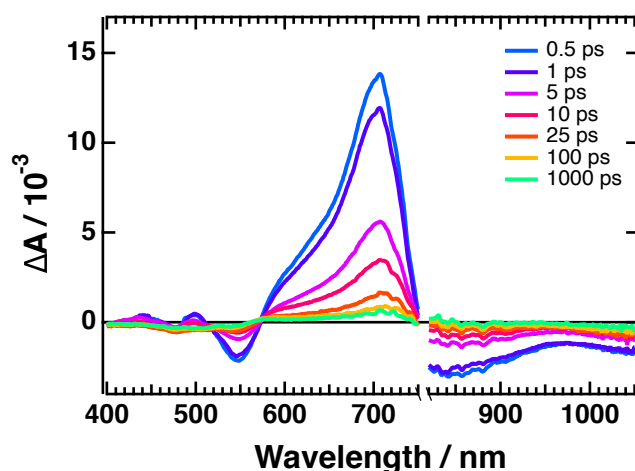


**Figure 4.3:** Transient absorption spectrum of a neat pristine DCSQ1 thin film spincoated from DCE. The sample was excited at 780 nm with a fluence of  $3 \mu\text{J cm}^{-2}$ .

In order to determine whether the positive feature corresponded to oxidised DCSQ1 species, oxidation experiments were once again carried out using nitrosyl tetrafluoroborate ( $\text{NOBF}_4$ ) and bromine vapour. Unfortunately the  $\text{NOBF}_4$  was unable to oxidise the DCSQ1 dye in solution (**figure B.11**). On the other hand, the absorption spectrum of the film following exposure to bromine vapour (**figure 4.4**) shows a broad positive feature between 600 and 800 nm, which could correspond to oxidised DCSQ1. However, given the typically harsh nature of the oxidation process using bromine vapour,

this feature could also correspond to the absorption of fragments of DCSQ1 following destruction by the oxidation process. Therefore, both of these oxidation experiments proved inconclusive.

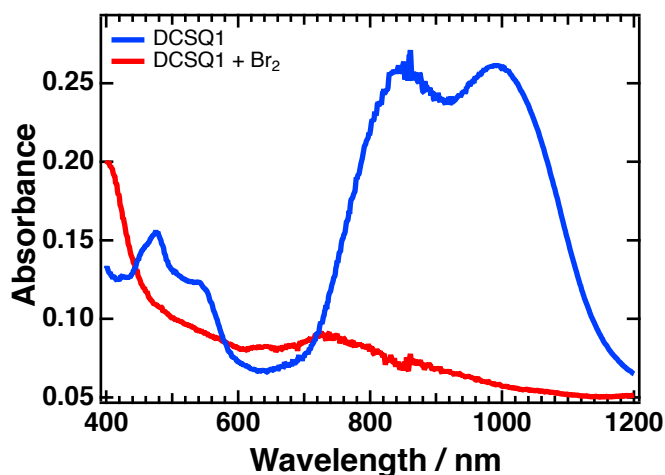


**Figure 4.4:** Absorption spectrum of a DCSQ1 thin film before (blue) and after (red) exposure to bromine vapour.

#### 4.2.2 Investigating the impact of aggregation

To assess the impact of aggregation on the TA spectrum of DCSQ1, polymethylmethacrylate (PMMA) was once again added in various blend ratios to DCSQ1 in solution and thin films were fabricated. Interestingly, unlike what was seen with the Cy5 dyes, the addition of PMMA had no effect on the degree of aggregation - the ratio of the monomer and the H-aggregate peak remained more-or-less constant and all that was observed was a dilution effect (**figure 4.5** and **figure B.12**).

This could be caused by the DCSQ1 dye having a strong affinity for forming the more thermodynamically stable H-aggregates, as shown by its tendency to form H-aggregates upon annealing or ageing. Therefore, the addition of PMMA is not able to disrupt the H-aggregates which form in the film. As a result, the TA spectra of the resultant PMMA:DCSQ1 thin films are practically identical (**figure B.13**).

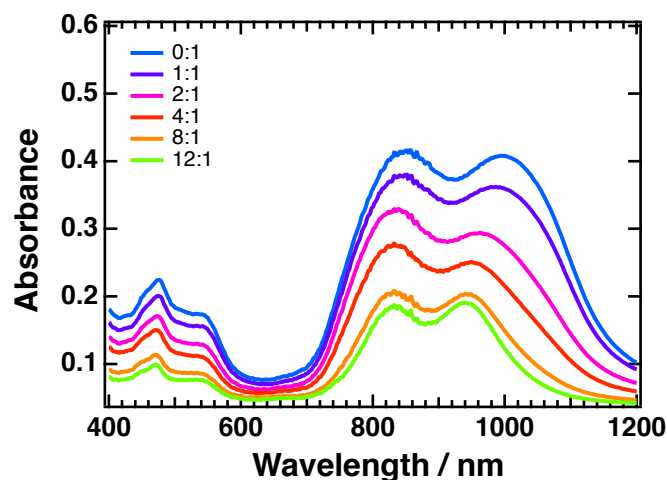


**Figure 4.5:** Absorption spectrum of thin films of various ratios of PMMA:DCSQ1.

Having seen the impact that annealing has on the degree of aggregation in **figure 4.2 c**, this was instead used as a method to determine whether the degree of H-aggregation leads to differences in the TA spectra. Pristine and annealed films, spincoated from a solution of DCSQ1 in DCE, were prepared and were excited at both 780 nm and 1000 nm. The purpose of this was to see if there were any differences when selectively exciting the monomers vs the H-aggregates.

From **figure 4.6**, it is clear that in the pristine film there is little difference between exciting at 780 and 1000 nm. Furthermore, when compared to the annealed film, the TA spectra have the same shape, with the only difference between them being a blue shift in the positive feature in the annealed TA spectra. This shift can be explained by the difference in the absorption spectra of the two films (**figure 4.2 b**), thus causing a change in the ground state bleaching, and therefore a shift in the isosbestic point which arises due to the overlap of the GSB and the ESA. Given that the driving force for the charge generation process in cyanine dyes was determined, in part, to be as a result of symmetry-breaking charge separation, the fact that the degree of H-aggregation appears to have little impact on the TA spectrum gives another strong indication that intrinsic charge generation does not occur in DCSQ1.

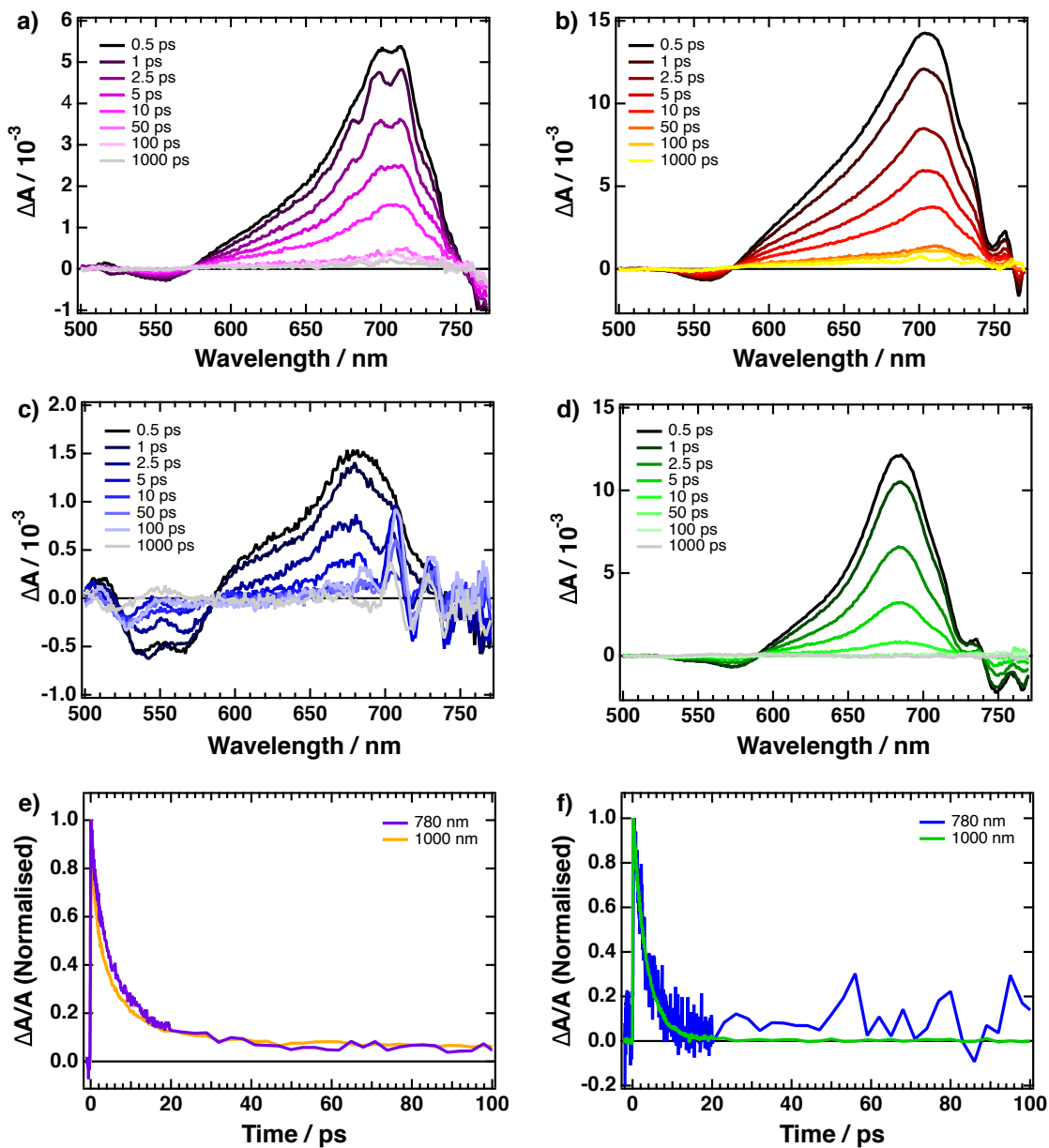


**Figure 4.6:** TA spectra of thin films of (a) pristine DCSQ1 excited at 780 nm, (b) pristine DCSQ1 excited at 1000 nm, (c) annealed DCSQ1 excited at 780 nm and (d) annealed DCSQ1 excited at 1000 nm. Kinetic traces of the ESA feature of (e) pristine DCSQ1 and (f) annealed DCSQ1.

### 4.2.3 Bilayers with C<sub>60</sub>

To conclusively determine whether intrinsic charge generation could occur in neat DCSQ1 thin films via the generation of redox species, DCSQ1/C<sub>60</sub> bilayers were fabricated. The reasoning behind these experiments was that there should be electron transfer occurring from the photoexcited DCSQ1 donor to the C<sub>60</sub> acceptor which would result in the formation of oxidised DCSQ1 chromophores. Therefore, the spectral signatures obtained in TA measurements of DCSQ1/C<sub>60</sub> bilayers could be compared to those obtained for neat DCSQ1 allowing one to determine whether intrinsic charge generation is occurring within the DCSQ1 dye.

Bilayers were fabricated with both the DCSQ1 on top of the glass (glass/DCSQ1/C<sub>60</sub> sample structure) and C<sub>60</sub> on top of the glass (glass/C<sub>60</sub>/DCSQ1). Both of these samples gave the same absorption spectra which can be seen in **figure 4.7**, along with the TA spectra of the glass/C<sub>60</sub>/DCSQ1 bilayer and the neat C<sub>60</sub> film. As expected, when exciting at 780 nm the TA spectrum of C<sub>60</sub> is almost flat and so it is possible to conclude that features arising from C<sub>60</sub> excitation will not contribute to the TA spectrum of the bilayer.

The TA spectrum of the bilayer has four main features - two negative features at 700 nm and 850 - 1050 nm alongside two positive features at 600 and 725 nm. As before, the broad negative feature above 850 nm can be assigned to the ground state bleaching. The positive feature, which spans from 725 to 850 nm appears to be made of two separate components, each with different kinetics; furthermore, the two features at 600 and 700 nm display the same kinetic dependence as the feature at 725 nm (**figure 4.7 d**). This indicates that a single process is responsible for the three features at 600, 700 and 725 nm whilst a separate process is responsible for the second part of the positive peak, centred at 820 nm. The three features at 600, 700 and 725 nm arise due to a photoinduced Stark effect; following photoexcitation, charge transfer excitons (CTEs) are formed at the interface between the DCSQ1 and the C<sub>60</sub>. These CTEs generate a photoinduced electric field which gives rise to the transient Stark effect. Furthermore, they also lead to the formation of oxidised DCSQ1, the absorption of which is responsible

for the positive feature centred at 820 nm.

Interestingly, such a TA spectrum was only seen in the glass/C<sub>60</sub>/DCSQ1 sample - the inverted structure gave the same TA spectrum as the neat DCSQ1 film. When spincoated on top of the C<sub>60</sub>, the DCSQ1 partially washes away the C<sub>60</sub> resulting in a 'melt' morphology (more similar to that of a bulk heterojunction) as opposed to the strict bilayer morphology achieved in the reverse structure. The more intimate mixing of DCSQ1 and C<sub>60</sub> domains present in the 'melt' morphology means that bulk Frenkel excitons formed in the DCSQ1 can more easily undergo diffusion and charge transfer to the C<sub>60</sub>, yielding the oxidised DCSQ1.

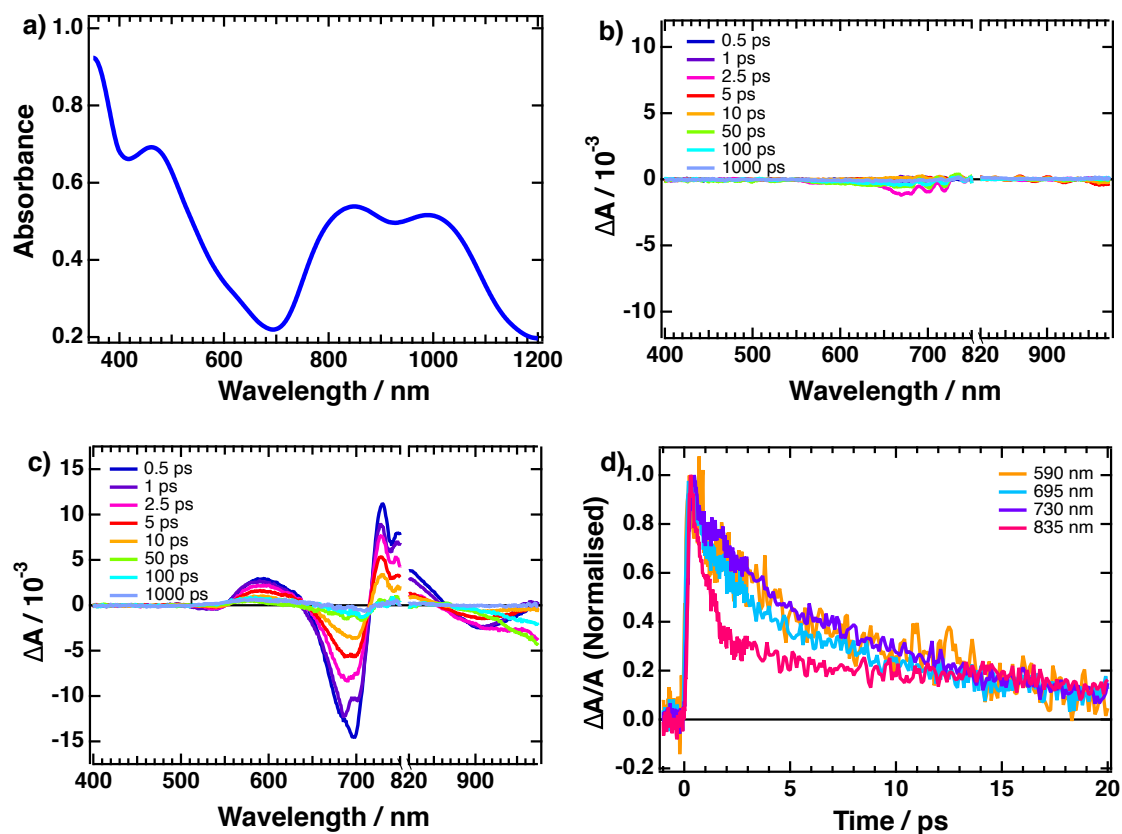


**Figure 4.7:** (a) Absorption spectrum of the DCSQ1/C<sub>60</sub> bilayer. Transient absorption spectra of (b) C<sub>60</sub> and (c) the DCSQ1/C<sub>60</sub> bilayer. Samples were excited at 780 nm with a fluence of 3  $\mu\text{J cm}^{-2}$ . (d) Kinetic traces extracted from the TA spectrum of the DCSQ1/C<sub>60</sub> bilayer.

#### 4.2.4 A comparison with the cyanine system

Returning now to the TA spectrum of the neat DCSQ1 thin film, it is evident from the lack of a positive peak at 750 - 850 nm, which would correspond to oxidised DCSQ1 species, that there is no intrinsic charge generation process occurring within the DCSQ1 thin films and so this feature can be assigned to excited state absorption.

Curiously, this is in contrast to the Cy5 thin films, where intrinsic charge generation was evident. There were two contributions to the driving force for this process: firstly, the presence of H-aggregates provides the necessary symmetry-breaking for the charge separation to occur and, importantly, it is possible for the monomers to be in contact with the H-aggregates ensuring sufficient orbital overlap between them. Secondly, the H-aggregates form a cation stack with the anions on the outside, resulting in the formation of local electric fields which lead to energy level shifts thus making charge transfer more favourable.

Given the neutral nature of the DCSQ1 dye, it is not possible for the formation of intrinsic electric fields to occur; as a result, there is a more homogeneous energy landscape in the DCSQ1 dye when compared to that of the Cy5 dyes. Therefore, it is unlikely that sufficient shifts in the HOMO and LUMO energy levels of nearby DCSQ1 chromophores could occur that would provide a thermodynamic driving force for the charge separation process.

Furthermore, given that H-aggregate formation is thermodynamically favourable, it is likely that there would be phase separation between the H-aggregates and the DCSQ1 monomers. Such a phase separation would result in sufficient spatial separation between the monomers and aggregates ensuring that a SB-CS process could not occur. In the Cy5 films, it is likely that there is greater mixing between the Cy5 monomer and H-dimer domains, ensuring that SB-CS can take place.

#### 4.2.5 Spiro-OMeTAD redox photochemistry

So far we have seen two different organic systems relevant to the field of organic photovoltaics and optoelectronics which differ in their ability to undergo intrinsic charge generation. This section focuses on spiro-OMeTAD (**figure 4.8**) which, as mentioned in the introduction to this chapter, is not a dye but rather a material frequently used as a HTM in perovskite solar cells as well as in solid-state DSSCs and OPVs.

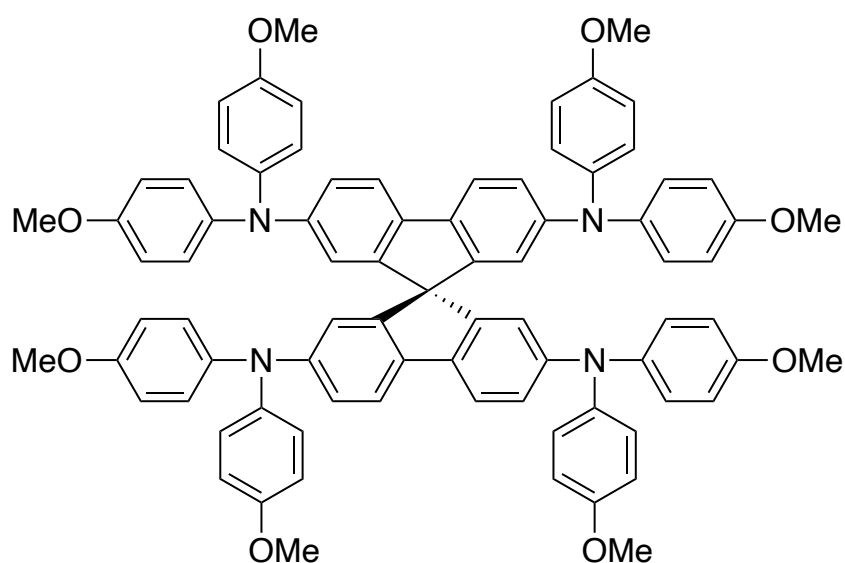


**Figure 4.8:** Structure of spiro-OMeTAD.

During the preparation of spiro-OMeTAD thin films, it was seen that if the solution was exposed to light for 20 minutes whilst still in an argon atmosphere, a colour change occurred. The steady state absorption spectra of two spiro-OMeTAD solutions, with one being exposed to light and the other not, are shown in **figure 4.9**. Despite sample preparation taking place in the absence of oxygen, it is evident that a photooxidation process takes place resulting in the solution changing colour from colourless to light-red

To explain the mechanism of anaerobic photooxidation of spiro-OMeTAD, TA was used and the resulting spectra of thin films of neat spiro-OMeTAD and with  $\text{La}(\text{TFSI})_3$



added are shown in **figure 4.10**. Metal-TFSI salts are commonly used additives in spiro-OMeTAD to improve device efficiency; here,  $\text{La}(\text{TFSI})_3$  was used in place of  $\text{LiTFSI}$  due to it enhancing the device stability whilst maintaining a high efficiency.

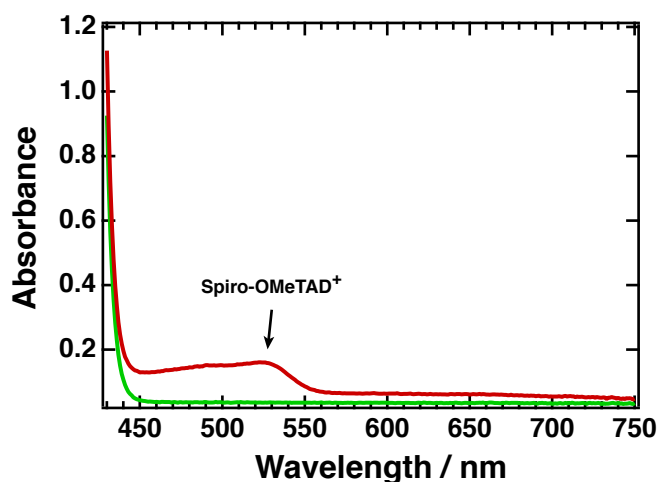


**Figure 4.9:** Absorption spectra of spiro-OMeTAD in chlorobenzene before (green) and after (red) exposure to light. The solution was prepared in the absence of oxygen.

The two TA spectra are remarkably similar, both displaying a broad positive feature between 460 and 650 nm. This positive feature is thought to possibly be a combination of the excited state absorption and product absorption resulting from the generation of photooxidised spiro-OMeTAD. Global analysis was therefore used to disentangle the various spectral components which contribute to the overall spectral shape, as well as give the lifetimes of the photogenerated species.

A bi-exponential function was used to fit the TA data, giving the decay associated spectra. Of the two absorption bands present, the one centred at 525 nm can be assigned to the decay of the oxidised spiro-OMeTAD<sup>+</sup>, whilst the red shifted band corresponds to the decay of the excited state absorption. The time constants extracted from the global analysis procedure indicate that in the neat spiro-OMeTAD film, the excited state absorption features give way to the product absorption of the oxidised spiro-OMeTAD on the picosecond timescale; the absence of an oxidant in the system implies that the spiro-OMeTAD<sup>+</sup> must be generated via an intrinsic charge separation

process.

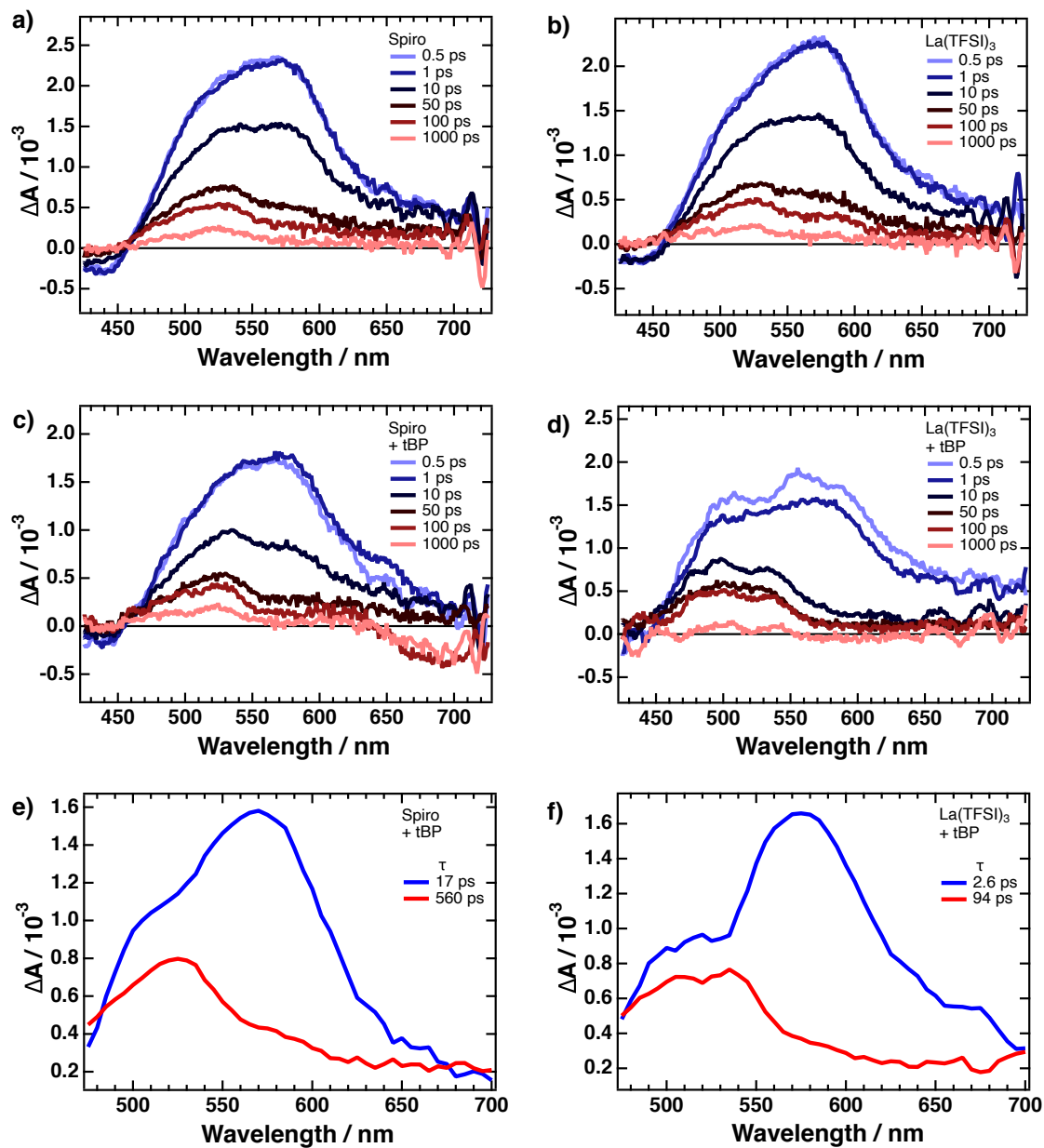


**Figure 4.10:** TA spectra of (a) neat spiro-OMeTAD, (b) with  $\text{La}(\text{TFSI})_3$  added, (c) with tBP added and (d) with  $\text{La}(\text{TFSI})_3$  and tBP added. Samples were excited at 389 nm with a fluence of  $12.5 \mu\text{J cm}^{-2}$ . Decay associated spectra obtained by fitting the TA data of spiro-OMeTAD (e) with tBP added and (f) with tBP and  $\text{La}(\text{TFSI})_3$  added. The spectra were fitted with a bi-exponential function.

As was the case with the cyanine thin films, the spiro-OMeTAD can undergo a photoinduced SB-CS process resulting in the generation of redox spiro-OMeTAD species as shown in the following equation:



It is expected that the reduced spiro-OMeTAD<sup>-</sup> absorbs further in the UV, and so the product absorption feature arising from its generation is outside the window of these TA measurements. The generation of oxidised spiro-OMeTAD occurs in 17 ps, and is unaffected by the addition of tBP. The oxidised spiro-OMeTAD decays with a time constant of 560 ps and, due to the fluence independence of this feature (**figure 4.11**), we can conclude that the oxidised species undergoes geminate recombination with the as-of yet spectrally unseen reduced species.

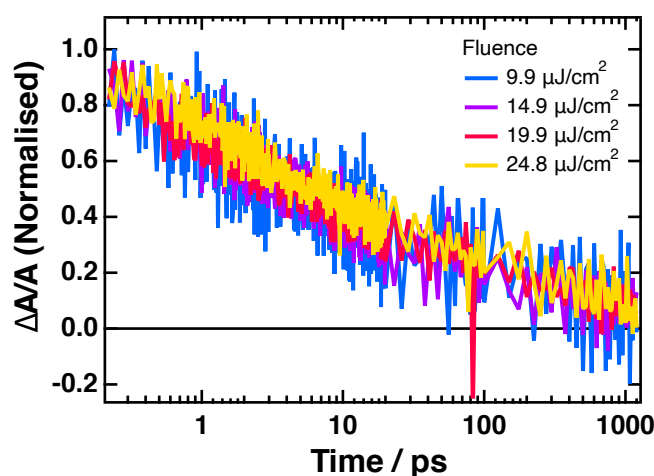


**Figure 4.11:** Kinetic traces extracted at 510 nm, showing the fluence dependence of the oxidised spiro-OMeTAD feature.

The thermodynamic driving force for the SB-CS could arise from intermolecular interactions within the thin film which could lead to small shifts in the HOMO and LUMO energy levels - this is shown in **figure 4.12**, where the molecule with the shifted energy levels is denoted as spiro'.

Upon addition of  $\text{La}(\text{TFSI})_3$  to the spiro-OMeTAD, there is little difference in the TA spectrum and kinetics, as mentioned previously. However, when tBP is added alongside the  $\text{La}(\text{TFSI})_3$ , the time constant for the generation of oxidised spiro-OMeTAD<sup>+</sup> reduces to 2.6 ps. This reduction implies that there is a larger thermodynamic driving force for SB-CS; this can be explained by the fact that the metal can form complexes with tBP which enhances the energy level shift of spiro', thus resulting in an increased driving force and therefore a faster rate of charge separation. A similar catalytic effect is seen when other  $\text{M}^{3+}(\text{TFSI})_3$  salts are added, alongside tBP, to the spiro-OMeTAD (figure B.14).

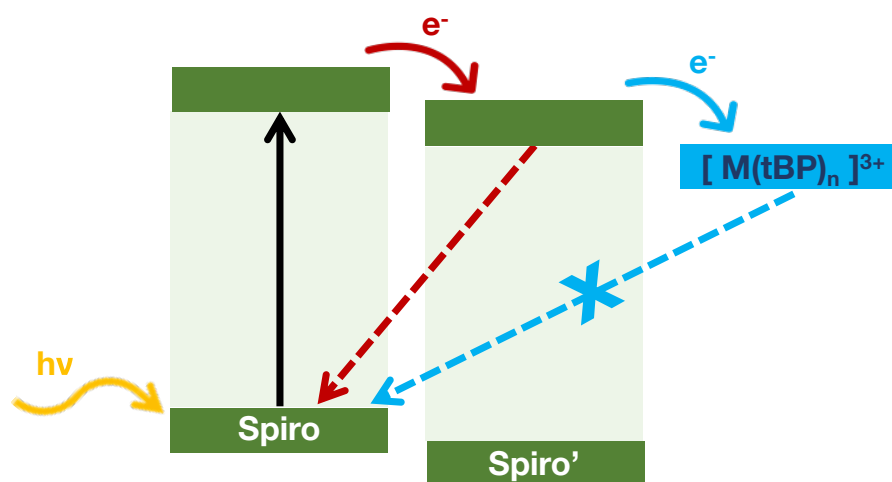


**Figure 4.12:** Scheme showing the symmetry-breaking charge separation process in spiro-OMeTAD. The curved blue arrow shows the scavenging of reduced spiro-OMeTAD by the trivalent lanthanide ions.

The high efficiency of the perovskite devices is maintained as the trivalent metal ions are able to scavenge the reduced spiro-OMeTAD anions (shown by the blue arrow in figure 4.12) resulting in efficient p-doping of the spiro-OMeTAD layer and thus leading to an increase in the hole conductivity. Meanwhile, the enhanced stability comes as a result of reduced ion migration when compared to  $\text{Li}^+$ .

### 4.3 Conclusion

In this chapter we have seen that intrinsic charge generation is not possible in the dicyanomethylene substituted squaraine dye DCSQ1. Transient absorption measurements on DCSQ1/C<sub>60</sub> bilayers gave information on the spectral signatures expected from oxidised DCSQ1, which were absent in the TA spectra of both pristine and annealed films of neat DCSQ1.

The absence of oxidised DCSQ1 in the transient spectra demonstrates that intrinsic charge generation is not possible, in contrast to what was seen in neat cyanine dye thin films. This difference can be explained by the neutral nature of the DCSQ1 dye resulting in a more homogeneous energy landscape ensuring that there are insufficient shifts in the HOMO and LUMO energy level of the DCSQ1 to make charge separation favourable.

In addition, given that the formation of H-dimers and higher order aggregates is strongly thermodynamically favoured, it is possible that there is a phase separation between the H-aggregates and the DCSQ1 monomers, resulting in too much spatial separation for a symmetry-breaking charge separation process to occur.

The second part of the chapter focused on spiro-OMeTAD, where transient absorption spectroscopy was used to demonstrate the formation of oxidised spiro-OMeTAD<sup>+</sup> via a symmetry-breaking charge transfer process. When La(TFSI)<sub>3</sub> was added to spiro-OMeTAD, the oxidised spiro-OMeTAD<sup>+</sup> was generated faster (in 2.6 ps vs 17 ps for neat spiro-OMeTAD) which could be explained by the La<sup>3+</sup> acting as a catalyst for the photoinduced symmetry-breaking charge separation. Such an effect was also seen with other M<sup>3+</sup>(TFSI)<sub>3</sub> salts.

## 4.4 Sample preparation

### Squaraine Experiments

The squaraine dye DCSQ1 was provided by the group of Prof. Frank Nüesch (EMPA, Switzerland). DCSQ1 solutions were prepared by dissolving the dye in either chlorobenzene or 1,2-dichloroethane with a concentration of 5 mg per mL. These solutions were then spincoated onto clean glass substrates inside a glovebox to give thin films for steady state absorption and TA measurements. Annealed films were prepared by annealing at 60 °C for 20 minutes. Aged films were prepared by leaving the film in ambient air for tens of hours.

C<sub>60</sub>/DCSQ1 bilayers were prepared via thermal deposition (Denton Benchtop Turbo) of C<sub>60</sub> (100 nm thickness) onto cleaned glass substrates followed by the spin-casting of DCSQ1.

### Spiro-OMeTAD Experiments

La(TFSI)<sub>3</sub> and Y(TFSI)<sub>3</sub> salts were provided by the group of Prof. Nam-Gyu Park (Sungkyunkwan University, South Korea), whilst the spiro-OMeTAD and LiTFSI were purchased from Sigma Aldrich. All chemicals were used as received.

Spiro-OMeTAD stock solutions were prepared by dissolving 72.3 mg of spiro-OMeTAD in chlorobenzene. Depending on the measurements, tBP (28.8 µL) and/or metal-TFSI solutions (17.5 µL) were added to the spiro-OMeTAD stock solutions. Metal-TFSI solutions were prepared by dissolving LiTFSI (520 mg/mL), Y(TFSI)<sub>3</sub> (561 mg/mL) or La(TFSI)<sub>3</sub> (591 mg/mL) in acetonitrile.

Prepared solutions were spincoated onto cleaned glass substrates at 3000 rpm for 20 s inside a glovebox.



## References

- (1) A. Treibs and K. Jacob, *Angew. Chem., Int. Ed. Engl.*, 1965, **4**, 2547.
- (2) K. Ilina, W. M. MacCuaig, M. Laramie, J. N. Jeouty, L. R. McNally and M. Henary, *Bioconjugate Chem.*, 2020, **31**, 194–213.
- (3) B. Oswald, F. Lehmann, L. Simon, E. Terpetschnig and O. S. Wolfbeis, *Anal. Biochem.*, 2000, **280**, 272–277.
- (4) J. D. Zimmerman, B. E. Lassiter, X. Xiao, K. Sun, A. Dolocan, R. Gearba, D. A. Vanden Bout, K. J. Stevenson, P. Wickramasinghe, M. E. Thompson and S. R. Forrest, *ACS Nano*, 2013, **7**, 9268–9275.
- (5) J. H. Delcamp, Y. Shi, J. H. Yum, T. Sajoto, E. Dell’Orto, S. Barlow, M. K. Nazeeruddin, S. R. Marder and M. Grätzel, *Eur. J. Chem.*, 2013, **19**, 1819–1827.
- (6) F. M. Jradi, X. Kang, D. Oneil, G. Pajares, Y. A. Getmanenko, P. Szymanski, T. C. Parker, M. A. El-Sayed and S. R. Marder, *Chem. Mater.*, 2015, **27**, 2480–2487.
- (7) B. Jin, X. Zhang, W. Zheng, X. Liu, J. Zhou, N. Zhang, F. Wang and D. Shang-guan, *Anal. Chem.*, 2014, **86**, 7063–7070.
- (8) S. Ferrara, S. H. Mejias, M. Liutkus, G. Renno, F. Stella, I. Kociolek, J. P. Fuenzalida-Werner, C. Barolo, P. B. Coto, A. L. Cortajarena and R. D. Costa, *Advanced Functional Materials*, 2022, **32**, 2111381.
- (9) B. Stender, S. F. Völker, C. Lambert and J. Pflaum, *Adv. Mater.*, 2013, **25**, 2943–2947.
- (10) J. J. Gassensmith, J. M. Baumes and B. D. Smith, *Chem. Commun.*, 2009, 6329–6338.

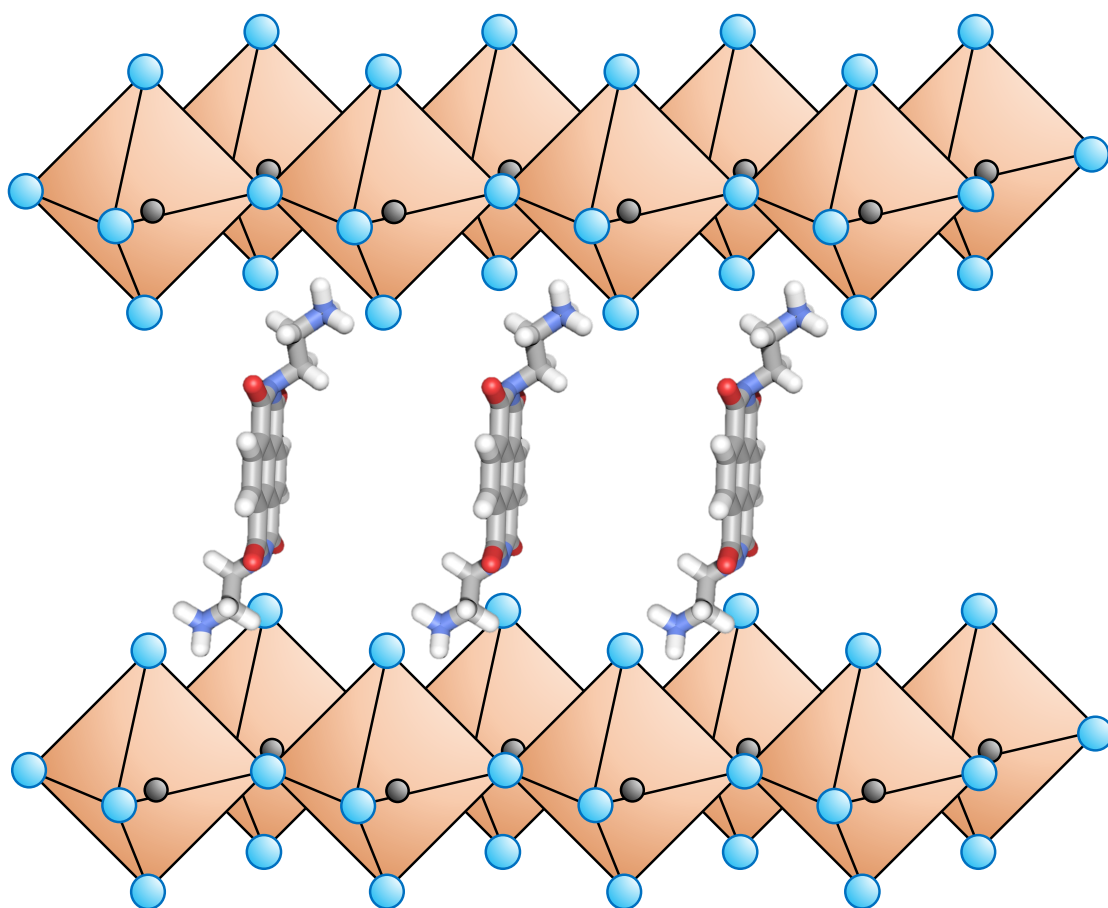
- (11) K. Strassel, W. H. Hu, S. Osbild, D. Padula, D. Rentsch, S. Yakunin, Y. Shynkarenko, M. Kovalenko, F. Nüesch, R. Hany and M. Bauer, *Sci. Technol. Adv. Mater.*, 2021, **22**, 194–204.
- (12) R. H. Wilson, K. P. Nadeau, F. B. Jaworski, B. J. Tromberg and A. J. Durkin, *J. Biomed. Opt.*, 2015, **20**, 030901.
- (13) G. W. Scott and K. Tran, *J. Phys. Chem.*, 1994, **98**, 11563–11569.
- (14) P. Salice, J. Arnbjerg, B. W. Pedersen, R. Toftegaard, L. Beverina, G. A. Pagani and P. R. Ogilby, *J. Phys. Chem. A*, 2010, **114**, 2518–2525.
- (15) S. Das, P. V. Kamat, B. De La Barre, K. G. Thomas, A. Ajayaghosh and M. V. George, *J. Phys. Chem.*, 1992, **96**, 10327–10330.
- (16) G. M. Paternò, N. Barbero, S. Galliano, C. Barolo, G. Lanzani, F. Scotognella and R. Borrelli, *J. Mater. Chem. C*, 2018, **6**, 2778–2785.
- (17) U. Bach, D. Lupo, J.-E. Moser, F. Weissörtel, J. Salbeck, H. Spreitzer and M. Grätzel, *Nature*, 1998, **395**, 585–585.
- (18) M. M. Lee, J. Teuscher, T. Miyasaka, T. N. Murakami and H. J. Snaith, *Science*, 2012, **338**, 643–647.
- (19) H. S. Kim, C. R. Lee, J. H. Im, K. B. Lee, T. Moehl, A. Marchioro, S. J. Moon, R. Humphry-Baker, J. H. Yum, J. E. Moser, M. Grätzel and N. G. Park, *Sci. Rep.*, 2012, **2**, 1–7.
- (20) S. Wang, Z. Huang, X. Wang, Y. Li, M. Günther, S. Valenzuela, P. Parikh, A. Cabrereros, W. Xiong and Y. S. Meng, *J. Am. Chem. Soc.*, 2018, **140**, 16720–16730.
- (21) J. Jeong, M. Kim, J. Seo, H. Lu, P. Ahlawat, A. Mishra, Y. Yang, M. A. Hope, F. T. Eickemeyer, M. Kim, Y. J. Yoon, I. W. Choi, B. P. Darwich, S. J. Choi, Y. Jo, J. H. Lee, B. Walker, S. M. Zakeeruddin, L. Emsley, U. Rothlisberger, A. Hagfeldt, D. S. Kim, M. Grätzel and J. Y. Kim, *Nature*, 2021, **592**, 381–385.
- (22) G. Kim, H. Min, K. Su Lee, D. Yoon Lee, S. Me Yoon and S. Il Seok, *Science*, 2020, **370**, 108–112.
- (23) U. B. Cappel, T. Daeneke and U. Bach, *Nano Lett.*, 2012, **12**, 4925–4931.



- 
- (24) S. Wang, W. Yuan and Y. S. Meng, *ACS Appl. Mater. Interfaces*, 2015, **7**, 24791–24798.
  - (25) S. Wang, M. Sina, P. Parikh, T. Uekert, B. Shahbazian, A. Devaraj and Y. S. Meng, *Nano Lett.*, 2016, **16**, 5594–5600.
  - (26) S. N. Habisreutinger, N. K. Noel, H. J. Snaith and R. J. Nicholas, *Adv. Energy Mater.*, 2017, **7**, 1–8.
  - (27) E. J. Juarez-Perez, M. R. Leyden, S. Wang, L. K. Ono, Z. Hawash and Y. Qi, *Chem. Mater.*, 2016, **28**, 5702–5709.
  - (28) B. Tan, S. R. Raga, A. S. Chesman, S. O. F  rer, F. Zheng, D. P. McMeekin, L. Jiang, W. Mao, X. Lin, X. Wen, J. Lu, Y. B. Cheng and U. Bach, *Adv. Energy Mater.*, 2019, **9**, 1901519.
  - (29) X. Wang, J. Wu, Y. Yang, X. Liu, Q. Guo, Z. Song, G. Li, Z. Lan and M. Huang, *J. Mater. Chem. A*, 2019, **7**, 13256–13264.
  - (30) J. Y. Seo, S. Akin, M. Zalibera, M. A. Preciado, H. S. Kim, S. M. Zakeeruddin, J. V. Mili   and M. Gr  tzel, *Adv. Func. Mater.*, 2021, **31**, 2102124.
  - (31) C. Gude and W. Rettig, *J. Phys. Chem. A*, 2000, **104**, 8050–8057.
  - (32) S. Spencer, H. Hu, Q. Li, H.-Y. Ahn, M. Qaddoura, S. Yao, A. Ioannidis, K. Belfield and C. J. Collison, *Prog. Photovolt: Res. Appl.*, 2015, **20**, 6–11.



## 5 Photophysics of 2D perovskites



The latter part of the previous chapter introduced perovskite solar cells, in particular exploring the mechanism of anaerobic photooxidation of spiro-OMeTAD. This chapter examines the formation of charge transfer excitons (CTEs) in 2D perovskites and determines the impact of spacer size and layer orientation on CTE formation. Ultra-fast transient absorption spectroscopy (TAS) is used to provide evidence of the photoinduced Stark effect which is subsequently quantified using electroabsorption spectroscopy. Following this, the possibility of charge transfer between the perovskite layer and the spacer material is examined.

This chapter is based on the following publications: “Investigating the Impact of Spacer Size and Layer Orientation on Charge Transfer Excitons in 2D Perovskites” and “Naphthalenediimide/Formamidinium-Based Low-Dimensional Perovskites”.<sup>1</sup> The contribution of collaborators is gratefully acknowledged. Algirdas Dučinskas and Masaud Almalki provided the perovskite thin film samples and Xia Meng acquired the SEM images.

## 5.1 Introduction

The field of lead halide perovskites (LHPs) has exploded over the past decade with them quickly becoming one of the most sought after materials for optoelectronic applications. Despite efficiencies north of 25% being achieved for single junction perovskite solar cells,<sup>2</sup> they are still plagued with poor stability (both intrinsic and extrinsic), in particular with respect to humidity.<sup>3,4</sup>

One strategy to overcome this issue is through the use of hybrid two-dimensional (2D) perovskites, where the A-site cation is replaced with a larger organic cation such as phenethylammonium (PEA).<sup>5,6</sup> The large cation prevents the formation of the typical  $ABX_3$  3D crystalline structure, instead yielding a layered structure consisting of planes of  $PbI_6$  octahedra separated by an organic spacer, S.

Often categorised by the crystallographic planes of their parent 3D structure, the  $\langle 100 \rangle$  orientation is the most common for 2D perovskites. This category can be further

sub-divided, based on the spacer, into Ruddlesden-Popper (RP) and Dion-Jacobsen (DJ) phases. RP perovskites, formed with a monovalent spacer, have the chemical formula  $S_2A_{n-1}B_nX_{3n+1}$  and have a staggered structure, whereas DJ perovskites ( $SA_{n-1}B_nX_{3n+1}$ ) are formed with a divalent organic spacer with no lateral displacement between the  $PbI_6$  layers.<sup>7,8</sup>

The optoelectronic properties of 2D perovskites can be tuned, to a degree, by changing the number of  $PbI_6$  layers between the organic spacers as well as by changing the spacer itself. For example, the optical band gap and the exciton binding energy can be easily modified.<sup>9-11</sup> Despite the improvement in device stability, the efficiency of 2D devices is well below that of 3D perovskites, primarily due to a wider optical bandgap and larger exciton binding energy when compared to their 3D counterparts. Furthermore, it is possible for the organic spacer cations to act as barriers to charge extraction. One strategy to overcome this would be via the use of a spacer material through which charge transfer from the perovskite layer could occur.

Despite a wide array of spacer materials being implemented in 2D perovskites including aromatic,<sup>12</sup> polycyclic aromatic<sup>13</sup> and aliphatic molecules,<sup>14</sup> the impact of changing the spacer on the photophysics of the system is often overlooked. At the current time, photophysical studies have utilised a wide variety of ultrafast techniques to explore different phenomena including the use of time-domain terahertz spectroscopy to investigate hot carrier cooling and charge carrier evolution,<sup>15,16</sup> as well as electroabsorption to study the quantum confined Stark effect in 2D perovskites of varying layers.<sup>17</sup>

There is, however, still uncertainty surrounding the role of the layer orientation (RP vs DJ) and spacer size on the formation of photoexcited species. Shedding light on this would provide new information regarding the choice of spacer in 2D perovskites, whilst the possibility of charge transfer between the  $PbI_6$  and organic spacer could stimulate new research avenues in other optoelectronic applications.<sup>1</sup>

## 5.2 Results and discussion

### 5.2.1 Impact of interlayer distance

In order to determine the impact of the interlayer distance on the photophysics in 2D perovskites, two samples were fabricated incorporating different spacer materials: 1,4-phenylenedimethylammonium (PDMA) and 1,4-phenylenediethylammonium (PDEA).

The structure of these two cations are shown in **figure 5.1**. As both are divalent, they form DJ perovskites with the formulae (PDMA)PbI<sub>4</sub> and (PDEA)PbI<sub>4</sub>. For clarity, the two perovskite samples will from now on be referred to by the spacer material.

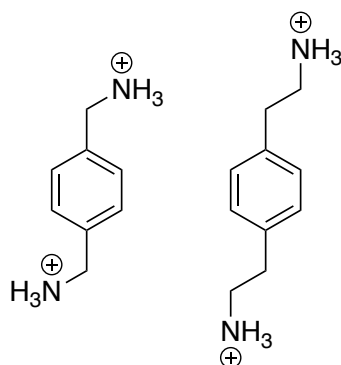


**Figure 5.1:** Structure of the PDMA (left) and PDEA (right) organic spacers.

Firstly, the phase purity of the 2D perovskite thin films was assessed using steady state absorption spectroscopy. From **figure 5.2 a**, it is evident that there is a single sharp peak present at 495 nm for the PDEA sample and 510 nm for the PDMA sample. This feature is characteristic of 2D perovskites and can be assigned to the excitonic band. An absence of additional peaks/features further in the red region (from 550 - 600 nm) indicates that the samples exhibit a pure  $n = 1$  2D perovskite structure, with no higher order phases present. It is important to establish this, as it means that features present in the subsequent transient absorption and electroabsorption measurements only arise from the  $n = 1$  layer and thus there are no contributions from higher order phases.

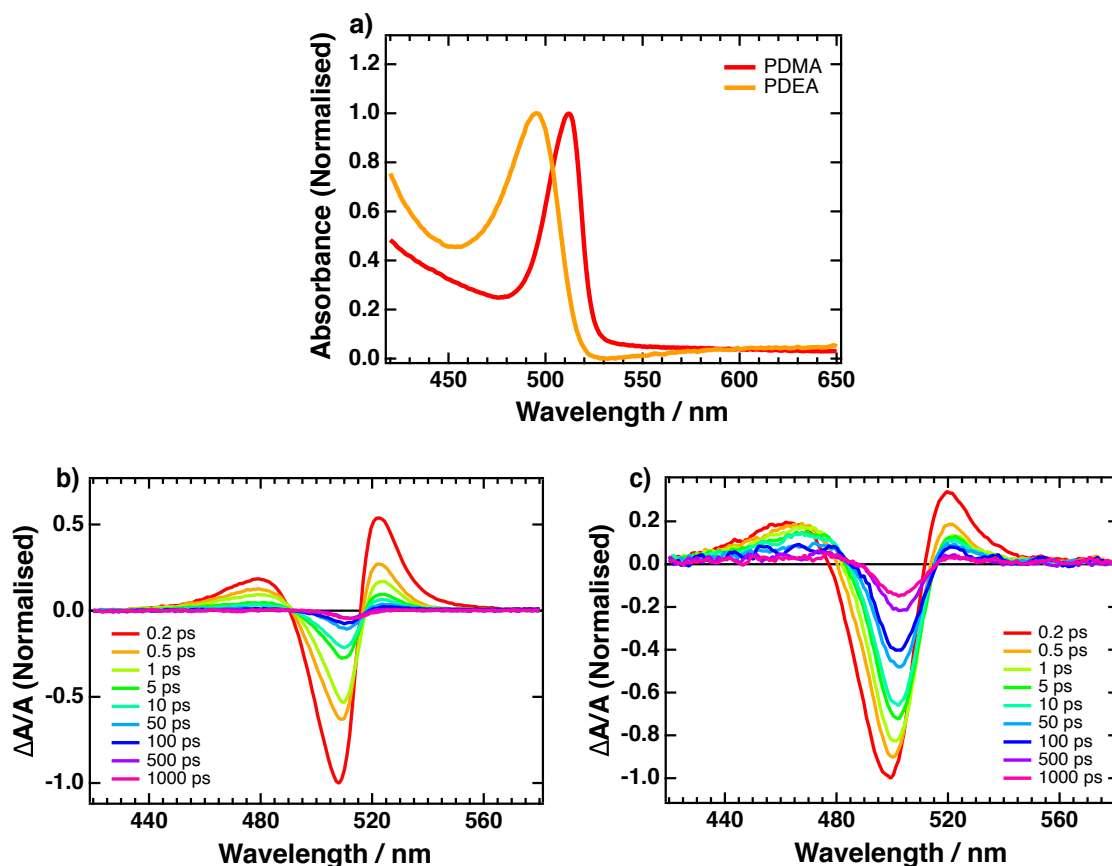


**Figure 5.2:** a) Steady state absorption spectra of (PDMA)PbI<sub>4</sub> (red) and (PDEA)PbI<sub>4</sub> (orange). Transient absorption spectra of (b) (PDMA)PbI<sub>4</sub> and (c) (PDEA)PbI<sub>4</sub>. Samples were excited at 390 nm with a fluence of  $2.5 \mu\text{J cm}^{-2}$ .

Transient absorption spectra of both the PDMA and PDEA samples, exciting at 390 nm, were then recorded and are shown in **figures 5.2 b** and **c**. The spectra of both samples are similar in shape, each presenting a negative feature flanked by two positive absorption features. First focusing on the PDMA TA spectrum, it is tempting to assign the negative feature (at 508 nm) to the bleaching of the ground state, given its similarity to the steady state absorption spectrum that was presented earlier. However, it is evident that the peak exhibits a red shift over time, from 508 to 513 nm over the 1 ns duration of the measurement, which is indicative of there being more than one contribution to this feature with each contribution having a different lifetime.

A second contribution to the negative peak could arise due to the photoinduced Stark

effect - such an effect could also explain the origin of the two positive features either side of the negative peak. By examining the kinetics of the three features (taken at 479, 508 and 522 nm, **figure 5.3**), it is evident that they all exhibit identical initial decays, implying that a single process contributes to each of them; this provides more evidence that a photoinduced Stark effect could be present in the system.

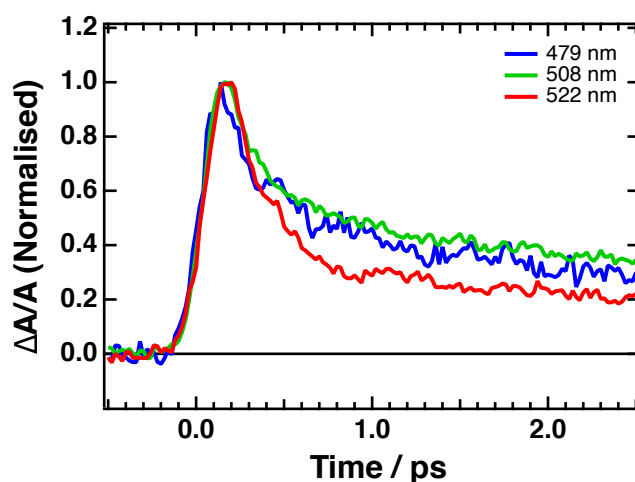


**Figure 5.3:** Kinetic traces for the three features in the PDMA TA spectrum (at 479, 508 and 522 nm), normalised to show the similarity of the early time dynamics of the three features.

As mentioned in **chapter 2**, the Stark effect arises when an electric field induces a shift in the absorption spectrum of the sample. The signal obtained from such a field induced shift is given by the following equation<sup>18</sup>:

$$\text{Signal} = -\frac{dA}{d\nu}\mu \cdot E + \frac{1}{2}\frac{d^2A}{d\nu^2}E^2 \cdot \Delta\mu^2 - \frac{1}{2}\frac{dA}{d\nu}E^2 \cdot \Delta\alpha \quad (5.1)$$

The first term is linear with respect to the electric field, and so is 0 and does not contribute to the electroabsorption signal in isotropic systems. The second term indicates that changes in the dipole moment,  $\mu$ , are associated with the second derivative of the absorption spectrum, whilst the third term indicates that the first derivative of the absorption spectrum is associated with changes in the polarisability. In the case



of the photoinduced Stark effect, the electric field,  $E$ , is generated intrinsically within the sample upon photoexcitation, and so these signals can be seen in TA measurements even when no external field is applied.

Through comparing the shape of the PDMA TA spectrum to the first and second derivative of its absorption spectrum (**figure B.15**) it is evident that the TA spectrum closely resembles that of the second derivative of the absorption spectrum. Therefore, it is possible to conclude that the photoinduced Stark effect predominantly arises from changes in the dipole moment. The electric field which is induced upon photoexcitation arises as a result of the formation of charge transfer excitons (CTEs). CTEs form following photoexcitation as it is possible for the charges to tunnel through the spacer resulting in a CTE being formed across the organic spacer.

Due to its similarity to the PDMA spectrum, the features in the PDEA TA spectrum can be assigned in the same manner. When comparing the PDMA and PDEA TA spectra, it is evident that the intensity of the photoinduced Stark effect feature, relative to that of the negative bleaching feature, is different in each case. The relative intensity of the Stark effect is lower in the PDEA system compared to the PDMA system; this can be explained by the longer alkyl chain length of the PDEA spacer resulting in an increase in the inter-layer separation and thus a reduction in the local electric field generated upon the formation of CTEs.<sup>19</sup> As the amplitude of the photoinduced Stark effect is dependent on the electric field strength, the reduction in the local electric field results in a reduction in the photoinduced Stark effect feature.

The formation of CTEs, for both systems, occurs within the instrument response of our setup (and so is less than 200 fs). Furthermore, global analysis of the TA data fitting with a tri-exponential function (**figure B.16**), yielding the decay associated spectra shown in **figure 5.4**, revealed that the lifetime of the CTEs is linked to the spacer size. It was found that CTEs in the PDMA system had a lifetime of 240 fs compared to 350 fs for those in the PDEA system. This difference can potentially be explained by the smaller PDMA spacer resulting in less spatial separation of the electron and hole thus increasing the rate of charge recombination. However, this cannot be conclusively de-

terminated, because as well as undergoing recombination, the CTEs can also separate into free charges. The two other components in the decay associated spectra can be assigned to the ground state bleaching and stimulated emission, both of which also contribute to the negative feature in the TA spectra.

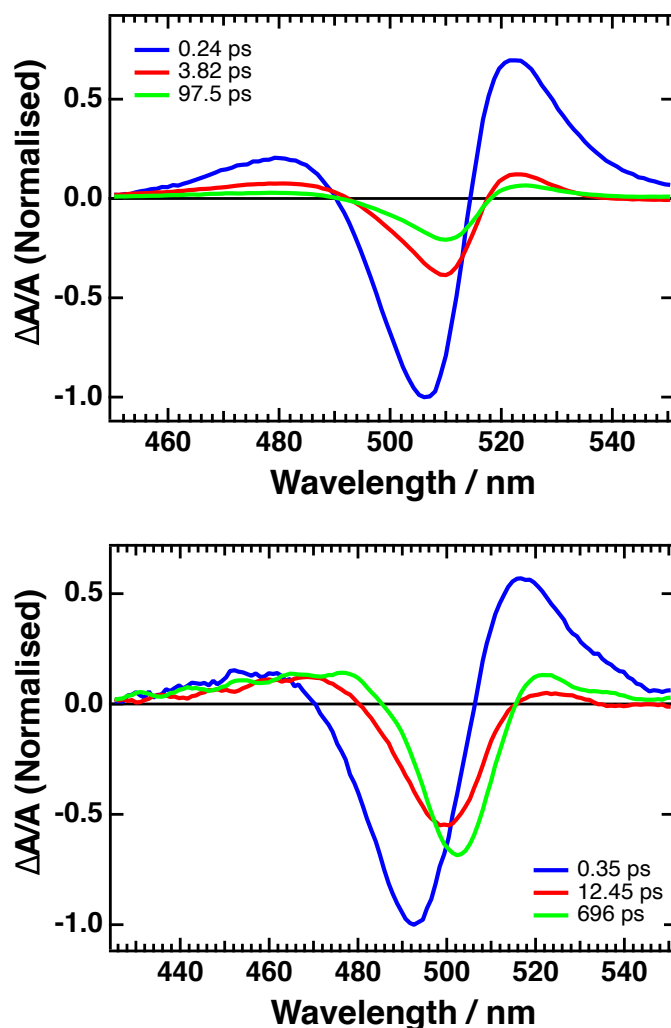


**Figure 5.4:** Decay associated spectra (DAS) following global analysis on the TA spectra of (PDMA)PbI<sub>4</sub> (top) and (PDEA)PbI<sub>4</sub> (bottom).

Following this, the electroabsorption (EA) spectra of the two samples were recorded and, as is evident from **figure 5.5**, the spectra have the same shape as the TA spectra; this further confirms the hypothesis that there is a photoinduced Stark effect present in the TA spectra as a result of CTE formation. However, the principle motivation

for conducting the EA measurements was to estimate the photoinduced electric field strength. This can be done by comparing the signal obtained in the TA measurements to that obtained from the voltage dependent EA measurements. This then allows one to estimate the voltage of the photoinduced field, and from this the electric field strength can be estimated.

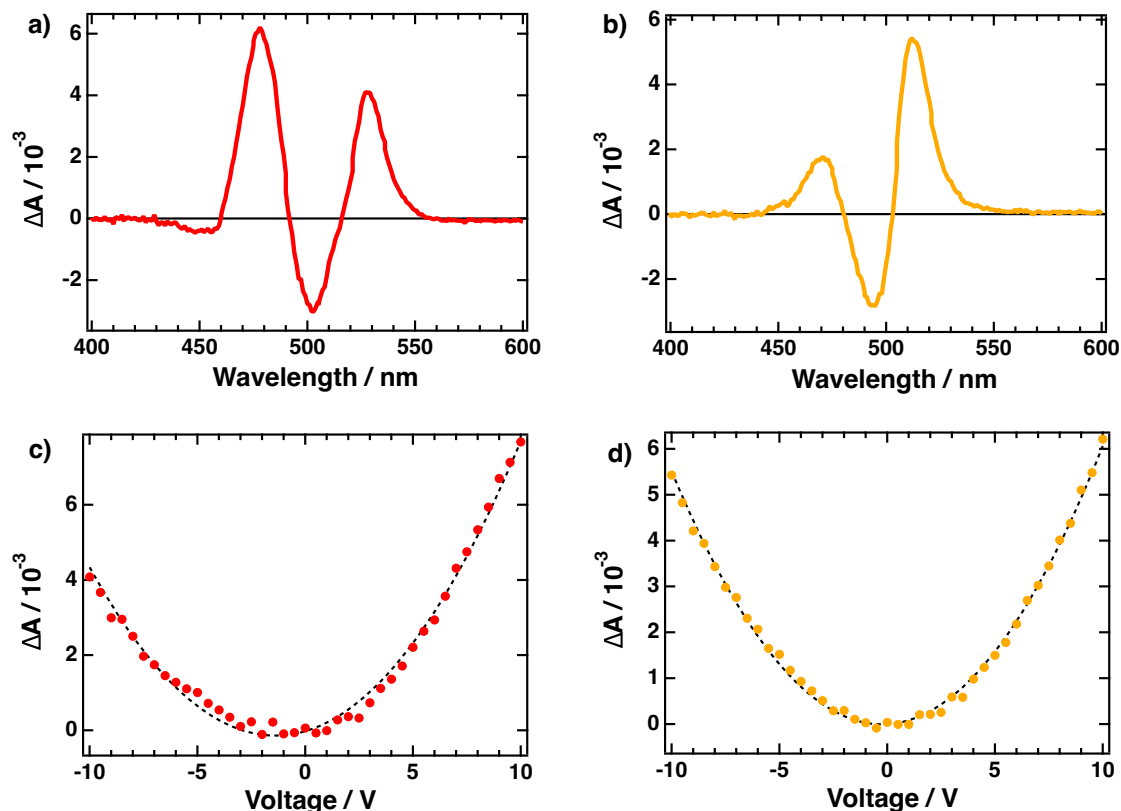


**Figure 5.5:** Electroabsorption spectra of (a) (PDMA)PbI<sub>4</sub> and (b) (PDEA)PbI<sub>4</sub>. Spectra were recorded at an applied voltage of -10 V. Graphs demonstrating the voltage dependence of the (c) (PDMA)PbI<sub>4</sub> and (d) (PDEA)PbI<sub>4</sub> samples taken at 526 nm and 512 nm, respectively.

As the samples for EA measurements had a glass/FTO/Al<sub>2</sub>O<sub>3</sub>/perovskite/gold structure, in order to know the exact voltage applied across the perovskite layer it is necessary to calculate the voltage drop across the aluminium oxide layer. Experimentally, this layer was required to ensure that the perovskite was not oxidised or reduced at the interface with FTO. Assuming that both the FTO and perovskite layers act as

capacitors, the following equation can be used to calculate the voltage drop across the perovskite layer<sup>20</sup>:

$$\Delta U_i = U_{app} \cdot \frac{d_i}{\varepsilon_i} \cdot \frac{1}{\sum \frac{d_i}{\varepsilon_i}} \quad (5.2)$$

where  $U_{app}$  is the applied potential,  $d_i$  the thickness of the layer  $i$  (obtained via cross-sectional SEM, **figure B.17**) and  $\varepsilon_i$  the relative permittivity of the material. The relative permittivity was taken to be 9 for  $\text{Al}_2\text{O}_3$ <sup>21</sup> and 25 for the perovskite materials.<sup>22,23</sup>

As the second positive peak in the TA spectra only contains contributions from the photoinduced Stark effect these were used to estimate the photoinduced voltage. For the PDMA sample, the signal obtained in the TA measurement would correspond to an applied potential of 2.1 V and a photoinduced electric field of  $10.2 \times 10^4 \text{ V cm}^{-1}$ . In comparison, the photoinduced electric field in the PDEA sample was estimated to be  $0.35 \times 10^4 \text{ V cm}^{-1}$ , a difference which can be rationalised by the larger spacer size resulting in an increased electron-hole distance within the CTE.

Temperature dependent steady state absorption and TA measurements were then carried out on the two different perovskite samples (**figure 5.6**). Looking at the steady state absorption spectra of the PDMA sample, it is evident that as the temperature decreases there is a decrease in the broadening of the excitonic band, an effect which has been seen previously.<sup>24</sup> The same effect is seen in the PDEA sample, but to a lesser extent. In the TA spectra, with decreasing temperature there is a blue shift in the peaks at 520 and 500 nm as well as an increase in intensity which is more apparent in the PDMA sample when compared to the PDEA sample.

The blue-shift is caused by a narrowing of the excitonic peak in the absorption spectra as the temperature decreases, which also explains why the shift is smaller in the PDEA TA spectrum as the narrowing in the absorption at lower temperatures is less prominent. Furthermore, the increase in TA signal intensity, as the temperature decreases, can be rationalised by an increase in the transient Stark effect.

This increase in intensity with decreasing temperature can be rationalised by an in-

crease in the transient Stark effect arising from crystal contraction resulting in a decrease in the interlayer spacing. This leads to an increase in the strength of the photoinduced electric field thus causing the signal increase in both the PDMA and PDEA TA spectra.

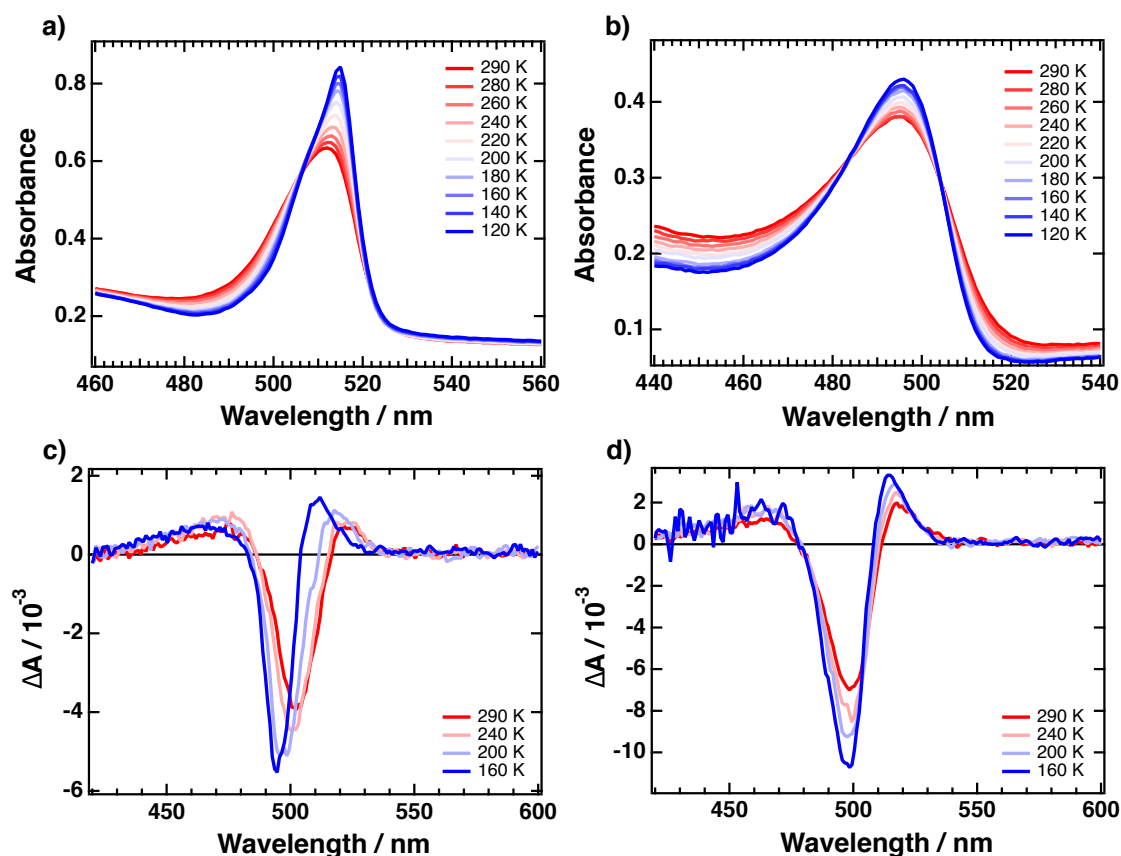


**Figure 5.6:** Temperature dependent steady state absorption spectra (top) and transient absorption spectra (bottom) of (PDMA)PbI<sub>4</sub> (a and c) and (PDEA)PbI<sub>4</sub> (b and d). For the TA spectra, the samples were excited at 390 nm with a fluence of  $6.25 \mu\text{J cm}^{-2}$  and the transient traces shown were taken at 0.5 ps after photoexcitation.

Further assessment of the TA spectra reveals that the intrinsic electric field increases by 97% in PDMA as the temperature decreases from 290 to 160 K, implying a decrease in the interlayer distance of the same percentage. Similarly, an increase of 67% is seen in the intrinsic field of the PDEA sample. Unfortunately, due to limitations of the setup it is not possible to determine the impact of temperature on CTE formation, as they are generated on a shorter timescale than the resolution of the TA setup. However,

it is possible to determine that there is an increase in the CTE lifetime with decreasing temperature, an observation that can be explained by a reduction in electron-phonon coupling at lower temperatures and thus a retardation of the CTE recombination.

### 5.2.2 Comparing Dion-Jacobsen and Ruddlesden-Popper perovskites

Having studied the impact of spacer size on CTE formation, this section compares DJ and RP 2D perovskites to determine what impact, if any, the layer orientation has on the photophysics. In order to form a RP perovskite, the monovalent organic spacer phenylethylammonium (PEA) was used (**figure 5.7**) resulting in a 2D perovskite with the formula  $(\text{PEA})_2\text{PbI}_4$ .

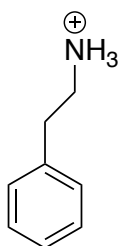


**Figure 5.7:** Structure of PEA.

As before, the steady state absorption spectrum allows us to determine that the sample is an  $n = 1$  phase pure sample (**figure 5.8 a**). Furthermore, the TA spectrum exhibits the now characteristic photoinduced Stark effect feature arising from the formation of CTEs. The lifetime of the CTEs is longer than in the PDMA system (500 fs vs 240 fs), a difference that can once again be explained by the larger interlayer distance.

At room temperature, the layer orientation appears to have little impact on the steady state absorption and TA spectra. This, however, changes at low temperatures where a new feature appears in the PEA TA spectrum (at 485 nm in the spectrum at 160 K) which is not seen in the DJ samples (**figure 5.8 c**). This feature can be explained by fitting the transient spectrum with a linear combination of the first and second derivative of the steady state absorption spectrum (**figure B.18**). Interestingly, there is

a 30% increase in the contribution of the first derivative component to the fit at 160 K when compared to the room temperature measurement.

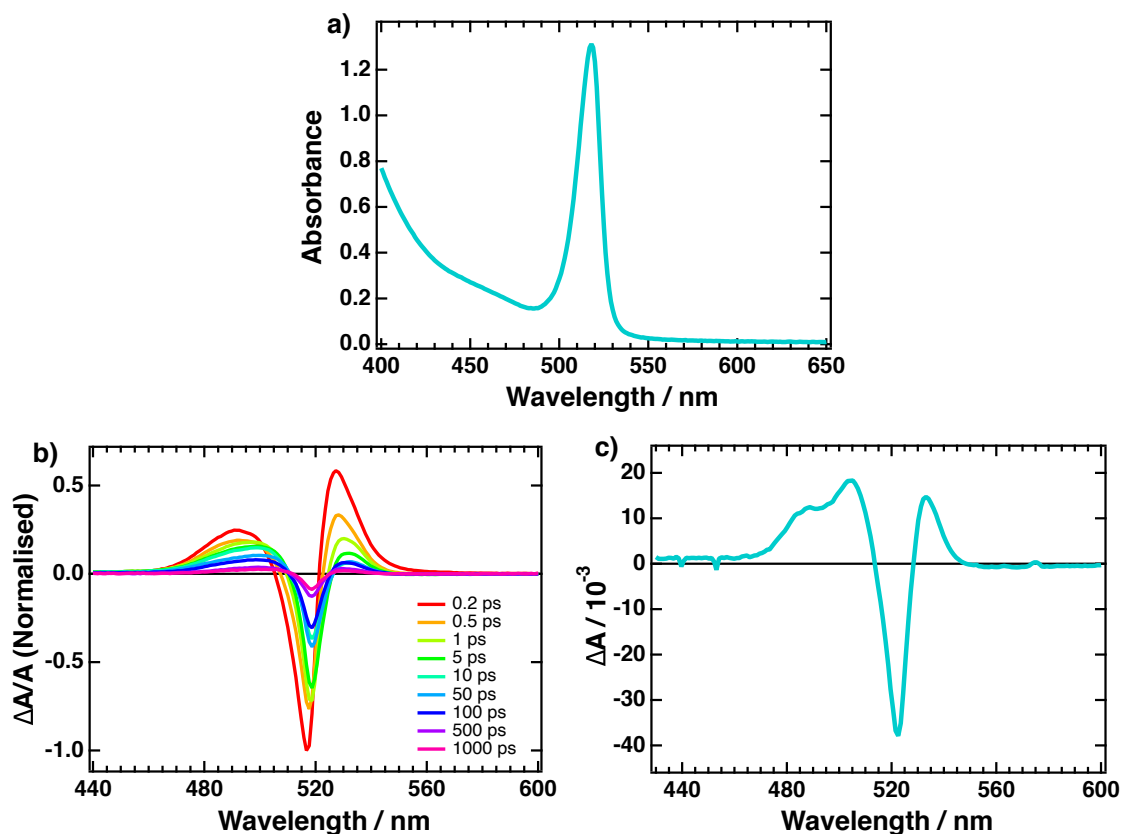


**Figure 5.8:** (a) Absorption spectrum of (PEA)<sub>2</sub>PbI<sub>4</sub>. (b) TA spectrum of (PEA)<sub>2</sub>PbI<sub>4</sub> at room temperature exciting at 390 nm with a fluence of 2.5  $\mu\text{J cm}^{-2}$ . (c) TA spectrum of (PEA)<sub>2</sub>PbI<sub>4</sub> at 160 K taken at 0.5 ps. The sample was excited at 390 nm with a fluence of 2.5  $\mu\text{J cm}^{-2}$ .

This increase in the contribution from the first derivative indicates that, with decreasing temperature, there is a contribution to the TA spectrum arising from the quantum confined Stark effect (QCSE) which is absent in DJ perovskites. Furthermore, the QCSE contribution also explains the red shift in the negative peak seen with decreasing temperature.<sup>17,25</sup>

### 5.2.3 Evidencing charge transfer to electroactive spacers

The final part of this chapter is focused on the possibility of charge transfer between the lead halide perovskite slabs and the organic spacer material. An electroactive naphthalenediimide-based organic spacer, 2,2'-(1,3,6,8-tetraoxo-1,3,6,8-tetrahydrobenzo[*lmn*][3,8]-phenanthroline-2,7-diyl)bis(ethylammonium) (NDIEA, **figure 5.9**), was employed as the organic spacer in a formamidinium lead halide (FAPbI<sub>3</sub>) based Dion-Jacobsen 2D perovskite with the formula (NDIEA)FA<sub>n-1</sub>Pb<sub>n</sub>I<sub>3n+1</sub> where *n* is the number of perovskite layers.

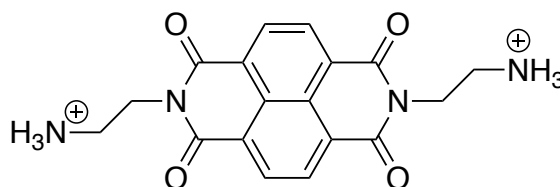


**Figure 5.9:** Structure of NDIEA.

This study will focus on the *n* = 1 and *n* = 2 phases, which were shown to stabilise the photoactive  $\alpha$ -FAPbI<sub>3</sub> phase. The stability of this phase, relative to the room-temperature stable  $\delta$ -FAPbI<sub>3</sub> phase,<sup>26,27</sup> is an issue that has led to MA-based 2D perovskites being preferred and thus more widely studied, despite the higher thermal stability of FA-based 2D perovskites.<sup>28–30</sup>

TA was used to see if charge transfer could occur between the perovskite and the NDIEA spacer; such an electron transfer process would be beneficial for improving charge extraction in 2D perovskites. Four different thin film samples were measured: two perovskite samples incorporating the NDIEA spacer (with *n* = 1 and *n* = 2), a neat (NDIEA)I<sub>2</sub> reference and finally a PDMA-based 2D perovskite reference.

Firstly, the (NDIEA)I<sub>2</sub> reference TA spectrum was recorded by exciting at 390 nm. The resulting spectrum, shown in **figure 5.10**, exhibits a broad positive feature centred at around 500 nm which can be assigned to the NDIEA radical anion formed upon photoexcitation.<sup>31,32</sup> Following this, the TA spectrum of the (NDIEA)PbI<sub>4</sub> was measured



exciting at 510 nm. This wavelength was chosen in order to selectively excite the perovskite and avoid excitation of the NDIEA. A positive feature is seen between 450 and 550 nm, and it appears within the first 500 fs. Due to its similarity to the peak seen in the NDIEA reference sample, it is likely that this feature once again corresponds to the radical NDIEA anion formed as a result of electron transfer from the perovskite to the NDIEA spacer.

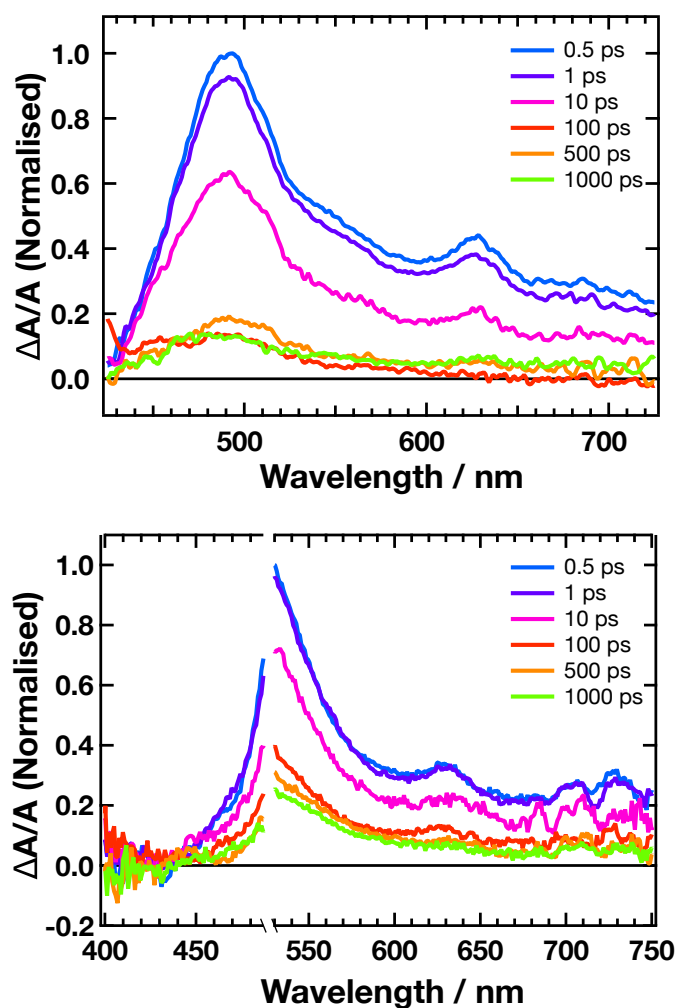


**Figure 5.10:** TA spectra of (NDIEA)I<sub>2</sub> (top) and (NDIEA)PbI<sub>4</sub> (bottom). (NDIEA)I<sub>2</sub> was excited at 390 nm whilst (NDIEA)PbI<sub>4</sub> was excited at 510 nm. Both samples were excited with a fluence of 16  $\mu\text{J cm}^{-2}$ .

However, it is possible that the feature could be a transient Stark effect feature arising from CTE formation, as seen earlier in this chapter, with the bleaching being covered by the pump. In order to eliminate this as a possibility, the (NDIEA)PbI<sub>4</sub> sample was also excited at 450 nm and the resulting TA spectra yielded the same positive feature centred around 500 nm (**figure 5.11**).

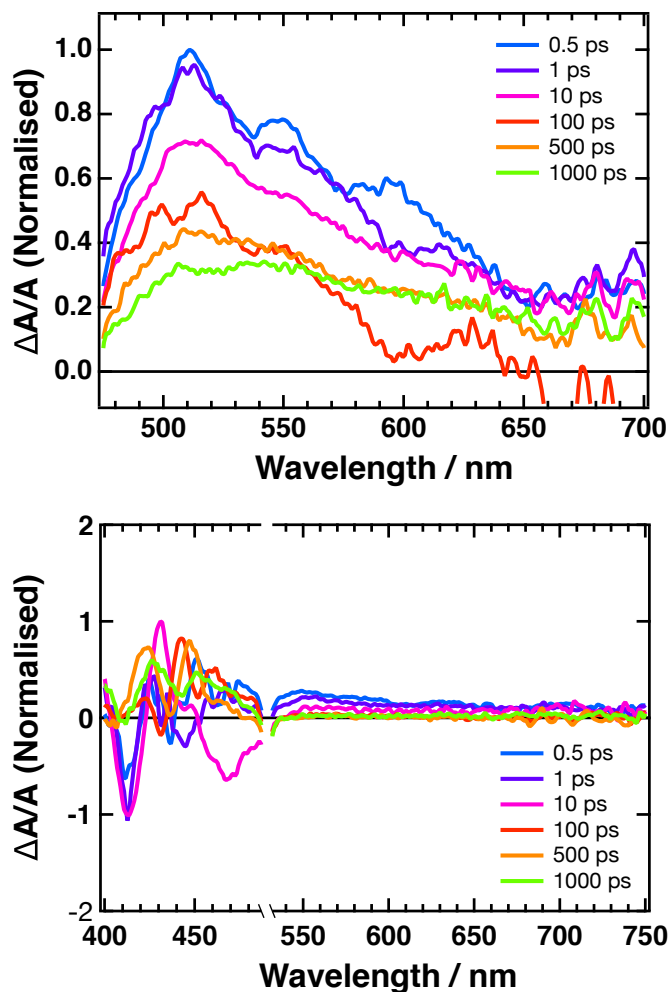


**Figure 5.11:** TA spectra of (NDIEA)PbI<sub>4</sub> (top) and (NDIEA)I<sub>2</sub> (bottom). The (NDIEA)PbI<sub>4</sub> sample was excited at 450 nm whilst the (NDIEA)I<sub>2</sub> was excited at 510 nm.

To finally confirm that the positive feature was due to electron transfer between the perovskite and the NDIEA spacer, the TA spectrum of the NDIEA reference was measured with an excitation wavelength of 510 nm. As seen in **figure 5.11**, there are no

appreciable features present in the spectrum, as expected, due to NDIEA not absorbing at the excitation wavelength. Therefore, this allows us to conclude that electron transfer takes place between the perovskite and the NDI-based spacer in less than 500 fs.

TA measurements on the (NDIEA)FAPb<sub>2</sub>I<sub>7</sub> (*n* = 2) sample also exhibited the same broad positive feature arising from the formation of NDIEA radical anions following electron transfer from the perovskite to the NDIEA spacer (**figure B.19**). A bleaching feature between 625 and 750 nm is also present in this sample, which is characteristic of the 3D perovskite phase.<sup>33</sup> Such an electron transfer process does not take place in the PDMA-based system, thus demonstrating that the choice of spacer plays an important role in whether charge transfer is possible between the perovskite and the organic spacer.

### 5.3 Conclusion

In this chapter, different ultrafast spectroscopic techniques, namely TA and EA, have been employed together to explore CTEs in 2D perovskites, as well as to determine the possibility of electron transfer from the lead halide layer to electroactive organic spacers.

The first part of this chapter focused on the impact of the spacer size on the photo-physics of 2D perovskites. A clear photoinduced Stark effect feature was seen in the DJ 2D perovskite samples arising due to the formation of CTEs within 200 fs after photoexcitation. By comparing the TA spectra of (PDMA)PbI<sub>4</sub> and (PDEA)PbI<sub>4</sub>, it was possible to determine that the strength of the photoinduced Stark effect is dependent upon the size of the organic spacer used, with larger spacers resulting in a smaller transient Stark effect; the lifetime of CTEs was also found to be dependent on spacer size, with larger spacers resulting in a longer CTE lifetime. Furthermore, a combination of EA and TA were used to estimate the strength of the photoinduced electric field which was found to be  $10.2 \times 10^4 \text{ V cm}^{-1}$  for (PDMA)PbI<sub>4</sub>. The photoinduced electric field strength was found to decrease for larger spacers. Temperature dependent TA measurements revealed that there was an increase in the Stark effect as the temperature decreases, as a result of crystal contraction.

The second part of this chapter compared RP perovskites to the aforementioned DJ perovskites. Once again, CTE formation was evident in the TA spectrum of the (PEA)<sub>2</sub>PbI<sub>4</sub> sample. However, the key difference came at low temperature where an additional peak appeared in the TA spectrum of the (PEA)<sub>2</sub>PbI<sub>4</sub> sample which was attributed to a contribution from the quantum confined Stark effect visualised as an increase in the first derivative contribution to the TA spectrum.

Finally, the last part of this chapter focused on whether charge transfer could be evidenced between the perovskite and an electroactive NDI-based spacer. By selectively exciting the perovskite, it was possible to show that NDIEA radical anions were formed within the first 500 fs as a result of electron transfer from the perovskite to the NDIEA

spacer.

These results demonstrate that changing the spacer can have a significant impact on the photophysics of 2D perovskites, in particular the formation of CTEs, which is a fact that could be exploited in the future to further their application in the field of optoelectronics.

## 5.4 Sample preparation

PDMA and PDEA precursor solutions were prepared by dissolving either (PDMA)I<sub>2</sub> or (PDEA)I<sub>2</sub>, alongside PbI<sub>2</sub> in a 1:1 ratio, in a 4:1 volumetric ratio of DMSO and DMF. The PEA precursor solution was prepared by dissolving (PEA)I and PbI<sub>2</sub> in a 2:1 ratio in the same DMSO:DMF solvent mixture. The three solutions were then heated to 60 °C and spincoated onto cleaned glass substrates at 1000 rpm for 10 s followed by a fast spin at 4000 rpm for 20 s, before undergoing annealing at 150 °C for 10 minutes yielding the 2D perovskite thin films.

Electroabsorption samples were fabricated by first depositing Al<sub>2</sub>O<sub>3</sub> (30 nm) via atomic layer deposition onto clean FTO patterned glass substrates, before spin coating the same precursor solutions as above. Finally, a gold electrode was deposited by thermal evaporation.

The (NDIEA)FA<sub>n-1</sub>Pb<sub>n</sub>I<sub>3n+1</sub> precursor solution was prepared by dissolving stoichiometric quantities of (NDIEA)I<sub>2</sub>, FAI and PbI<sub>2</sub> in a 4:1 volumetric ratio of DMF and DMSO. The solution was then spincoated onto cleaned glass substrates following the same procedure as above, before also being annealed at 150 °C for 15 minutes.

Thin film thickness was determined using cross-sectional SEM (Zeiss Merlin).



## References

- (1) A. Mishra, P. Ahlawat, G. C. Fish, F. Jahanbakhshi, M. Mladenović, M. Almalki, M. A. Ruiz-Preciado, M. C. Gelvéz-Rueda, D. J. Kubicki, P. A. Schouwink, V. Dufoulon, T. Schneeberger, A. Aslanzadeh, F. C. Grozema, S. M. Zakeeruddin, J. E. Moser, U. Rothlisberger, L. Emsley, J. V. Milić and M. Grätzel, *Chem. Mater.*, 2021, **33**, 6412–6420.
- (2) J. Jeong, M. Kim, J. Seo, H. Lu, P. Ahlawat, A. Mishra, Y. Yang, M. A. Hope, F. T. Eickemeyer, M. Kim, Y. J. Yoon, I. W. Choi, B. P. Darwich, S. J. Choi, Y. Jo, J. H. Lee, B. Walker, S. M. Zakeeruddin, L. Emsley, U. Rothlisberger, A. Hagfeldt, D. S. Kim, M. Grätzel and J. Y. Kim, *Nature*, 2021, **592**, 381–385.
- (3) G. Niu, W. Li, F. Meng, L. Wang, H. Dong and Y. Qiu, *J. Mater. Chem. A*, 2014, **2**, 705–710.
- (4) J. M. Frost, K. T. Butler, F. Brivio, C. H. Hendon, M. Van Schilfgaarde and A. Walsh, *Nano Lett.*, 2014, **14**, 2584–2590.
- (5) J. Ye, H. Zheng, L. Zhu, G. Liu, X. Zhang, T. Hayat, X. Pan and S. Dai, *Sol. RRL*, 2017, **1**, 1–8.
- (6) R. Garai, R. K. Gupta, M. Hossain and P. K. Iyer, *J. Mater. Chem. A*, 2021, **9**, 26069–26076.
- (7) X. Gao, X. Zhang, W. Yin, H. Wang, Y. Hu, Q. Zhang, Z. Shi, V. L. Colvin, W. W. Yu and Y. Zhang, *Adv. Sci.*, 2019, **6**, 1900941.
- (8) L. Mao, W. Ke, L. Pedesseau, Y. Wu, C. Katan, J. Even, M. R. Wasielewski, C. C. Stoumpos and M. G. Kanatzidis, *J. Am. Chem. Soc.*, 2018, **140**, 3775–3783.

- (9) D. H. Cao, C. C. Stoumpos, O. K. Farha, J. T. Hupp and M. G. Kanatzidis, *J. Am. Chem. Soc.*, 2015, **137**, 7843–7850.
- (10) Z. Yuan, Y. Shu, Y. Xin and B. Ma, *Chem. Commun.*, 2016, **52**, 3887–3890.
- (11) W. Peng, J. Yin, K. T. Ho, O. Ouellette, M. De Bastiani, B. Murali, O. El Tall, C. Shen, X. Miao, J. Pan, E. Alarousu, J. H. He, B. S. Ooi, O. F. Mohammed, E. Sargent and O. M. Bakr, *Nano Lett.*, 2017, **17**, 4759–4767.
- (12) J. Hu, I. W. Oswald, S. J. Stuard, M. M. Nahid, N. Zhou, O. F. Williams, Z. Guo, L. Yan, H. Hu, Z. Chen, X. Xiao, Y. Lin, Z. Yang, J. Huang, A. M. Moran, H. Ade, J. R. Neilson and W. You, *Nat. Commun.*, 2019, **10**, 1276.
- (13) M. C. Gélvez-Rueda, W. T. Van Gompel, R. Herckens, L. Lutsen, D. Vanderzande and F. C. Grozema, *J. Phys. Chem. Lett.*, 2020, **11**, 824–830.
- (14) S. Ahmad, P. Fu, S. Yu, Q. Yang, X. Liu, X. Wang, X. Wang, X. Guo and C. Li, *Joule*, 2019, **3**, 794–806.
- (15) A. Burgos-Caminal, E. Socie, M. E. Bouduban and J. E. Moser, *J. Phys. Chem. Lett.*, 2020, **11**, 7692–7701.
- (16) J. Yin, R. Naphade, P. Maity, L. Gutiérrez-Arzaluz, D. Almalawi, I. S. Roqan, J. L. Brédas, O. M. Bakr and O. F. Mohammed, *Nat. Commun.*, 2021, **12**, 3995.
- (17) G. Walters, M. Wei, O. Voznyy, R. Quintero-Bermudez, A. Kiani, D. M. Smilgies, R. Munir, A. Amassian, S. Hoogland and E. Sargent, *Nat. Commun.*, 2018, **9**, 4214.
- (18) M. F. Bouduban, A. Burgos-Caminal, J. Teuscher and J.-E. Moser, *CHIMIA*, 2017, **71**, 231–235.
- (19) A. Dučinskas, G. C. Fish, M. A. Hope, L. Merten, D. Moia, A. Hinderhofer, L. C. Carbone, J. E. Moser, F. Schreiber, J. Maier, J. V. Milić and M. Grätzel, *J. Phys. Chem. Lett.*, 2021, **12**, 10325–10332.
- (20) A. A. Paraecattil, J. De Jonghe-Risse, V. Pranculis, J. Teuscher and J. E. Moser, *J. Phys. Chem. C*, 2016, **120**, 19595–19602.
- (21) C. M. Tanner, Y. C. Perng, C. Frewin, S. E. Sadow and J. P. Chang, *Appl. Phys. Lett.*, 2007, **91**, 203510.



- 
- (22) X. Zhang, X. Ren, B. Liu, R. Munir, X. Zhu, D. Yang, J. Li, Y. Liu, D. M. Smilgies, R. Li, Z. Yang, T. Niu, X. Wang, A. Amassian, K. Zhao and S. Liu, *Energy Environ. Sci.*, 2017, **10**, 2095–2102.
- (23) M. Shao, T. Bie, L. Yang, Y. Gao, X. Jin, F. He, N. Zheng, Y. Yu and X. Zhang, *Adv. Mater.*, 2022, **34**, 2107211.
- (24) Y. Zhang, R. Wang, Y. Li, Z. Wang, S. Hu, X. Yan, Y. Zhai, C. Zhang and C. X. Sheng, *J. Phys. Chem. Lett.*, 2019, **10**, 13–19.
- (25) V. I. Quelo, M. E. Bouduban, I. García-Benito, A. Fedorovskiy, S. Orlandi, M. Cavazzini, G. Pozzi, H. Trivedi, D. C. Lupascu, D. Beljonne, J. E. Moser, M. K. Nazeeruddin, C. Quarti and G. Grancini, *Adv. Func. Mater.*, 2020, **30**, 2000228.
- (26) M. T. Weller, O. J. Weber, J. M. Frost and A. Walsh, *J. Phys. Chem. Lett.*, 2015, **6**, 3209–3212.
- (27) A. Binek, F. C. Hanusch, P. Docampo and T. Bein, *J. Phys. Chem. Lett.*, 2015, **6**, 1249–1253.
- (28) J. Yan, W. Fu, X. Zhang, J. Chen, W. Yang, W. Qiu, G. Wu, F. Liu, P. Heremans and H. Chen, *Mater. Chem. Front.*, 2018, **2**, 121–128.
- (29) J. V. Milić, J. H. Im, D. J. Kubicki, A. Ummadisingu, J. Y. Seo, Y. Li, M. A. Ruiz-Preciado, M. I. Dar, S. M. Zakeeruddin, L. Emsley and M. Grätzel, *Adv. Energy Mater.*, 2019, **9**, 1–12.
- (30) M. C. Gélvez-Rueda, P. Ahlawat, L. Merten, F. Jahanbakhshi, M. Mladenović, A. Hinderhofer, M. I. Dar, Y. Li, A. Dučinskas, B. Carlsen, W. Tress, A. Ummadisingu, S. M. Zakeeruddin, F. Schreiber, A. Hagfeldt, U. Rothlisberger, F. C. Grozema, J. V. Milić and M. Graetzel, *Adv. Func. Mater.*, 2020, **30**, 1–9.
- (31) S. V. Bhosale, C. H. Jani and S. J. Langford, *Chem. Soc. Rev.*, 2008, **37**, 331–342.
- (32) M. A. Kobaisi, S. V. Bhosale, K. Latham, A. M. Raynor and S. V. Bhosale, *Chem. Rev.*, 2016, **116**, 11685–11796.
- (33) C. V. Franco, B. Mahler, C. Cornaggia, T. Gustavsson and E. Cassette, *Nanomaterials*, 2020, **10**, 1–15.



## 6 Conclusion and outlook

In this thesis, ultrafast spectroscopic techniques, principally transient absorption and electroabsorption spectroscopy, have been used to probe the photophysics of different materials relevant to the field of photovoltaics ranging from infrared absorbing organic dyes to two-dimensional perovskites.

The first results chapter focused on pentamethine cyanine (Cy5) dyes, where TAS was used to evidence high efficiency intrinsic photoinduced charge generation. Two different mechanisms were proposed, proceeding either via the excitation of Cy5 monomers followed by electron transfer to H-aggregates or via the direct excitation of H-aggregates followed by quenching by monomers. This symmetry-breaking charge separation process proceeded with a quantum yield of up to 86%, and the efficiency of the charge separation process was shown to be dependent upon the interchromophore distance, and therefore the choice of anion. The driving force was proposed to come from local electric fields arising from the arrangement of anions on the outside of H-aggregate cation stacks, as well as the intermixing of aggregate and monomer domains which provide the breaking of symmetry. Whilst the impact of anion size was investigated, this work could be further extended to see if intrinsic charge generation could also occur in cyanine dyes with longer polymethine chains (i.e. Cy7 dyes); these systems are currently being explored for use in transparent OPVs, and so such a study could provide important implications for such uses.

The second results chapter investigates if symmetry-breaking charge separation can also take place in other organic materials used in photovoltaics; the first part is dedicated to dicyanomethylene substituted squaraine (DCSQ) dyes, where it was found that intrinsic charge generation was not possible. This was determined by TA measurements on DCSQ1/C<sub>60</sub> bilayers which gave the spectral signatures of oxidised DCSQ1 which were absent from TA spectra of the neat dye. The lack of symmetry-breaking charge separation was proposed to be due to phase separation between the H-aggregates and the DCSQ1 monomers, as well as the neutral nature of the dye leading to an absence of local electric fields forming. Having explored dicyanomethylene substituted squaraine dyes, it would be interesting to determine whether intrinsic charge generation would be possible in other squaraine systems as they have been used extensively alongside PCBM in bulk heterojunction OPVs, and so if SB-CS were possible it could open the door to increase the PCE of such devices through improving the  $V_{OC}$ . Furthermore, having established that the presence of counterions played a role in the intrinsic charge generation mechanism in cyanine dyes, it would be interesting to explore this in the context of squaraine dyes.

The second half of this chapter, on the other hand, is focused on the HTM spiro-OMeTAD; here, symmetry-breaking charge separation was used to explain the anaerobic photooxidation of spiro-OMeTAD. The mechanism provided to explain the anaerobic photooxidation results in the formation of reduced spiro-OMeTAD<sup>-</sup> species - further work could be undertaken to determine if it is indeed formed upon photoexcitation, which would provide more evidence for the suggested mechanism. Spectroelectrochemistry could be used to isolate the absorption spectrum of the reduced spiro-OMeTAD<sup>-</sup>. Transient absorption spectroscopy, covering a wider range from the deep-UV to the near-infrared could then be undertaken (dependent on the absorption spectrum of spiro-OMeTAD<sup>-</sup>) to determine if the reduced species is formed upon photoexcitation.

The final results chapter is focused on two-dimensional (2D) perovskites, and it was shown that both the size of the organic spacer and the layer orientation impact upon the ultrafast photophysics. 2D perovskites with smaller spacers exhibited a larger photoin-

duced Stark effect, as a result of the larger photoinduced electric field, whilst low temperature TA measurements revealed that the photoinduced Stark effect in Ruddlesden-Popper 2D perovskites has a contribution from the quantum confined Stark effect which increases with decreasing temperature. This work could be built upon in the future by determining what happens to the charge transfer excitons, i.e. whether they undergo recombination, or separate into free charges, and whether the fate of charge transfer excitons is influenced by the interlayer distance. Finally, TA was also used to evidence electron transfer from the perovskite to a NDI-based electroactive spacer, a feature which could be exploited in future optoelectronic applications. It would be interesting to conduct further experiments to determine the rate of the electron transfer between the perovskite and the organic spacer, as well as determine whether the size of spacer has an impact on this rate.





## Acknowledgements

A wise man once said that 4 years is not a long time; however, it is long enough to meet a lot of great people who were instrumental in helping me throughout my 4 years at EPFL.

Firstly, I would like to express my gratitude to Prof. Jacques-E Moser for giving me the opportunity to do my PhD thesis in his group. I am grateful for being given the scientific freedom to study different systems, as well as the encouragement to go to a variety of scientific conferences across the continent. I will miss the great group dynamic that you have developed over the years. Finally, I appreciate the fact that your door was always open for both scientific and non-scientific chats and especially group trip discussions.

I would also like to thank Prof. Eric Vauthey, Prof. Kevin Sivula and Prof. Natalie Stingelin for being the members of my jury, as well as Prof. Jiri Vanicek for presiding over the exam.

Throughout the four years, I had the pleasure to have many great friends as colleagues. Starting with the old guard, I must extend my gratitude to Marine who taught me all there is to know about the laser systems in the femtocave whilst showing off your questionable British accent - it was a shame that our paths only crossed for a short time. Secondly, Arun, who although had already departed the group by the time I arrived, had a 100% attendance record for group outings and dinners - we shared lots of laughs together, and it was always great to hear your stories from times gone by in the lab. Finally, Andrés, thank you for being a great amigo throughout the two years we spent

---

in the lab together - we had some great times skiing, visiting Barcelona and debating the efficacy of bike mirrors. Also thank you for all of your invaluable guidance on the THz set-up!

Moving on to more recent group members, I would firstly like to thank Brener (aka B-Dog). I will never forget your crazy stories (most of which are regrettably not suitable for a PhD thesis), the office games we played to pass some time, our trips to Luigia and, of course, all of the questions you asked me. You were a great friend, and I wish that you could have spent more time in our lab, as the 15 months went by so quickly! Secondly, Vincent for all the fun, often random, discussions we had as well as the good times spent in the lab together - it was a shame that you got stuck in Belgium and that your PhD was cut short. Thirdly, Aaron - it was a pleasure having you in the lab for your masters thesis, and I'm glad you were able to come back for another year. We had some great (sometimes explosive!) times in the lab together. I will also look back fondly on our conference trips together, skiing in Austria and playing minigolf in Grindelwald. It would have been great to have you as a group member for more time! I must also thank Fara for all of the administrative support over the past four years.

I would also like to thank the other master students who I had the pleasure of supervising: André and Patricia. In particular, though, I would like to thank Juanma who became a great friend during his time in our group - we shared many great moments together both inside and out of the lab, and I wish you all the best for your PhD and future career.

Saving the best co-worker thank you until last, I must extend my thanks to Etienne - I am lucky that I was able to share my 4 years at EPFL with such a great friend. I will always look back fondly on the great times we had in the office watching marble races, doing sporcle quizzes and mots fléchés - all of which certainly helped me get through some less-fun scientific times. Outside of the lab, I must thank you for getting me into running and biking - we had some great runs and rides together, as well as trips away to Rome and Grindelwald. I wish you all the best for the future, and I know you will be successful at whatever you decide to do next!



---

Outside of our lab, I would like to give my appreciation to everyone who I have had the pleasure of collaborating with over the years: Algirdas, Essa, Jing, Jovana, Linfeng, Masaud, Natalie, Roland, Simon, Thomas, Tomislav, Wei-Hsu, Xia and Yameng. In particular, I would like to thank Prof. Frank Nüesch for introducing me to the topic of cyanine dyes, and for all of our scientific discussions over the years.

Sophie, I must thank you for all of the love and support that you have given me this year and for helping me throughout the writing process - your kind words always helped to pick me up and the adventures we have had together provided me the motivation to keep writing.

Finally, I would like to thank my parents and my brother for being supportive of my decision to come to Switzerland to do my PhD, and for always being there over the past four years.



## A List of abbreviations and chemical names

### Abbreviations

BHJ	Bulk heterojunction
CPA	Chirped pulse amplification
CTE	Charge transfer exciton
D/A	Donor/acceptor
DAS	Decay associated spectrum
DJ	Dion-Jacobson
DSSC	Dye-sensitised solar cell
EA/EDA	Electroabsorption/electro-modulated differential absorption
$E_g$	Bandgap
$E_p$	Phonon energy
ESA	Excited state absorption
FF	Fill factor
FRET	Förster resonance energy transfer
GSB	Ground state bleaching
HOMO	Highest occupied molecular orbital
HTM	Hole transport material
IC	Internal conversion
ISC	Inter-system crossing

LUMO	Lowest unoccupied molecular orbital
NOPA	Non-collinear optical parametric amplifier
OPV	Organic photovoltaic
PCE	Power conversion efficiency
RP	Ruddlesden-Popper
SB-CS	Symmetry-breaking charge separation
SE	Stimulated emission
SEM	Scanning electron microscopy
$S_n$	$n^{\text{th}}$ singlet electronic state
SWIR	Short wave infrared
TA(S)	Transient absorption (spectroscopy)
$T_n$	$n^{\text{th}}$ triplet electronic state
TOF	Time-of-flight
TREAS	Time resolved electroabsorption spectroscopy
$V_{\text{OC}}$	Open circuit voltage
VR	Vibrational relaxation

## Chemical names

Al(pfad) <sub>4</sub>	Tetrakis(perfluoro-1-adamantoxy)aluminate
Al(pftb) <sub>4</sub>	Tetrakis(nonafluoro-tert-butoxy)aluminate
CB	Chlorobenzene
Cy5	1,3,3-Trimethyl-2-[5-(1,3,3-trimethyl-1,3-dihydro-indol-2-ylidene) -penta-1,3-dienyl]-3H-indolium
DCE	1,2-Dichloroethane
DCSQ	Dicyanomethylene substituted squaraine
FA <sup>+</sup>	Formamidinium
FTO	Fluorine-doped tin oxide
ITO	Indium-doped tin oxide
MA <sup>+</sup>	Methylammonium
NDIEA	2,2'-(1,3,6,8-Tetraoxo-1,3,6,8-tetrahydrobenzo[lmn][3,8] -phenanthroline-2,7-diyl)bis(ethylammonium)
NOBF <sub>4</sub>	Nitrosyl tetrafluoroborate
P	Hexafluorophosphate
PC <sub>61(71)</sub> BM	Phenyl-C61(/71)-butyric acid methyl ester
PDEA	1,4-Phenylenediethylammonium
PDMA	1,4-Phenylenedimethylammonium
PEA	Phenylethylammonium
PMMA	Poly(methyl methacrylate)
Spiro-OMeTAD	2,2',7,7'-Tetrakis (N,N-di(4-methoxyphenylamine)-9,9' -spirobifluorene
SQ	Squaraine
tBP	4- <i>tert</i> -Butylpyridine
TFSI	Bis(trifluoromethanesulfonyl)imide



## **B** Supplementary figures

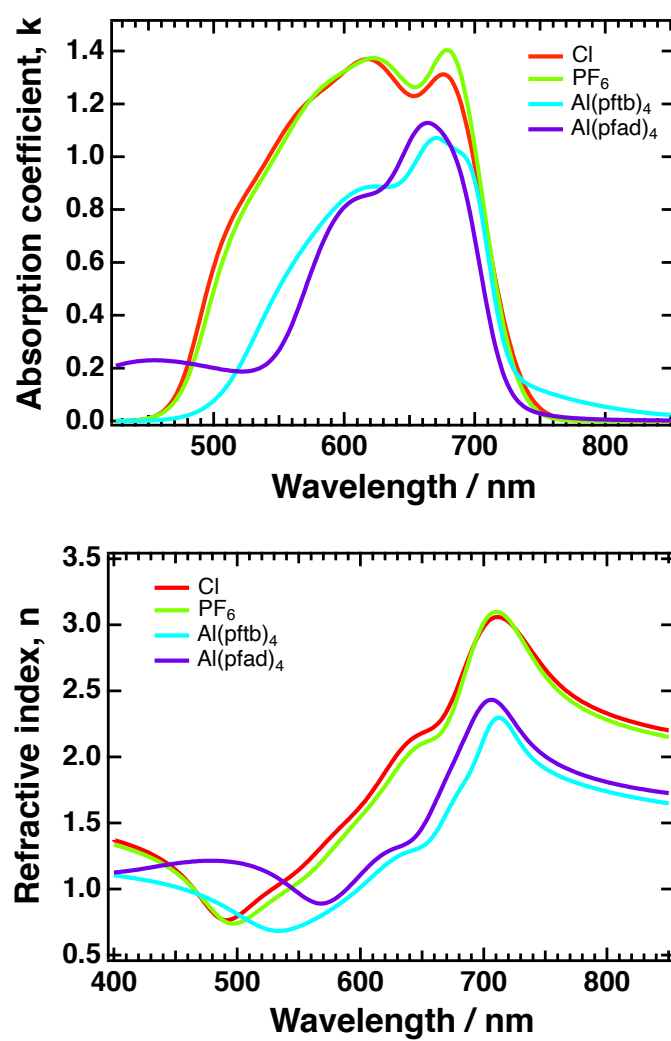
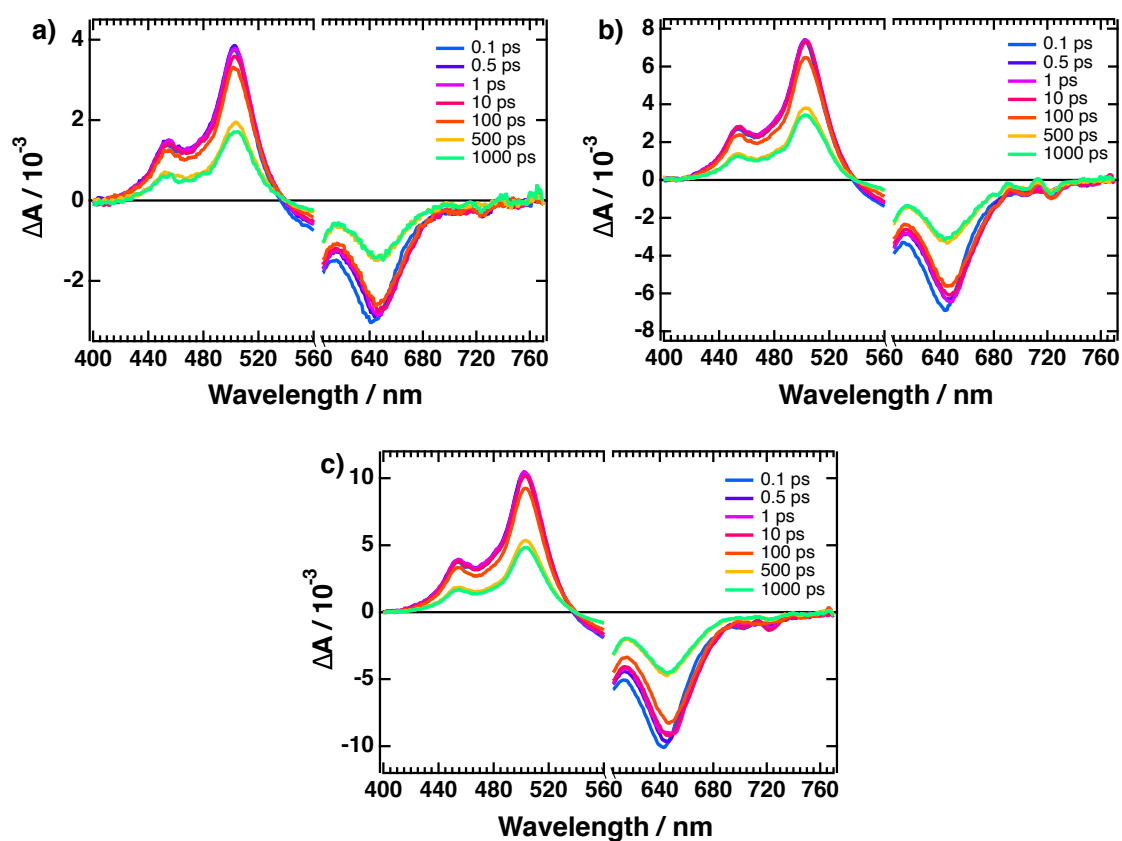
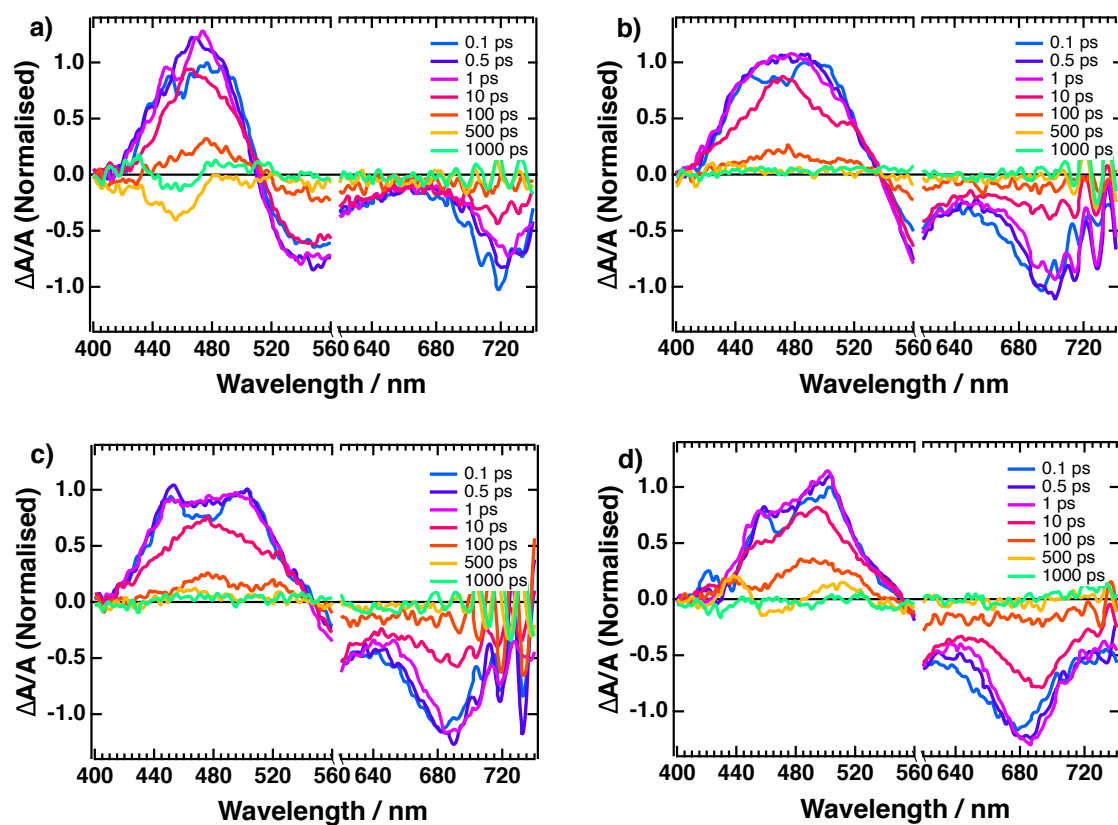


Figure B.1: Optical constants  $k$  and  $n$  as measured by ellipsometry.





**Figure B.2:** Transient absorption spectra of a solution of Cy5-P in acetonitrile measured at different fluences.



**Figure B.3:** Transient absorption spectra of different PMMA:Cy5-P blends: (a) 1:1, (b) 4:1, (c) 8:1 and (d) 12:1. Samples were excited at 580 nm, and the spectra have been normalised to the signal at 100 fs for ease of comparison between the different blends.

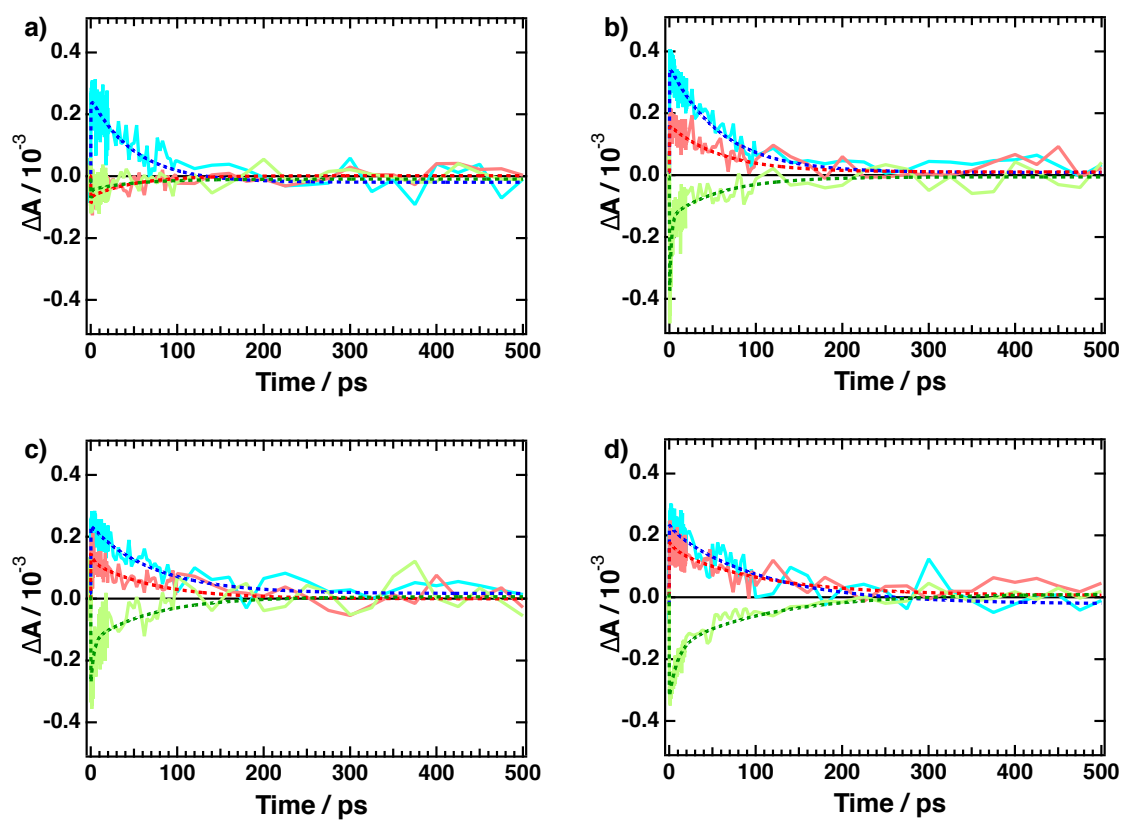


**Figure B.4:** Kinetic traces at 470 (blue), 520 (red) and 700 nm (green) for different ratios of PMMA:Cy5-P thin films. The dashed lines show the result of the global fitting procedure.

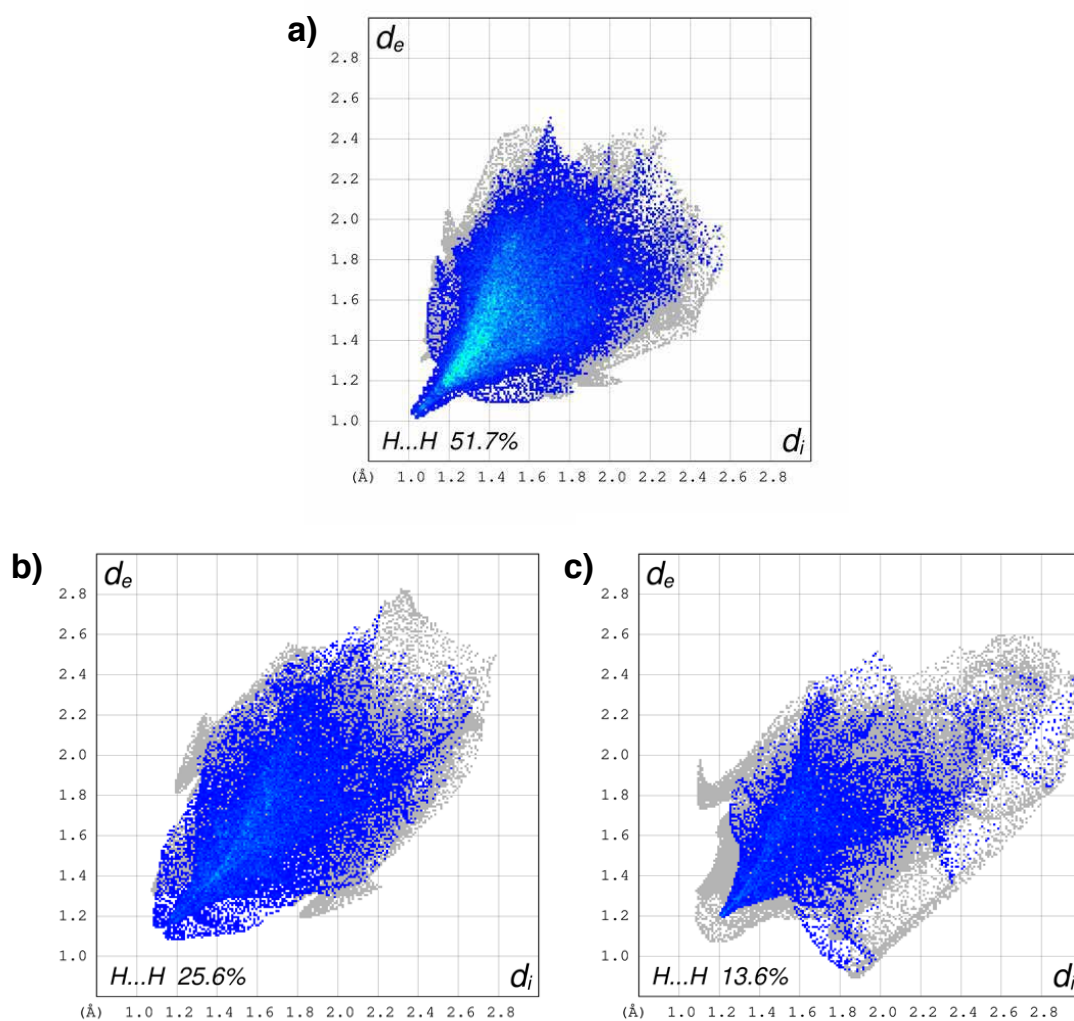


**Figure B.5:** Fingerprint plots showing the distribution of inter-cationic H-H contacts for (a) Cy5-PF<sub>6</sub>, (b) Cy5-[Al(pftb)<sub>4</sub>] and (c) Cy5-[Al(pfad)<sub>4</sub>].

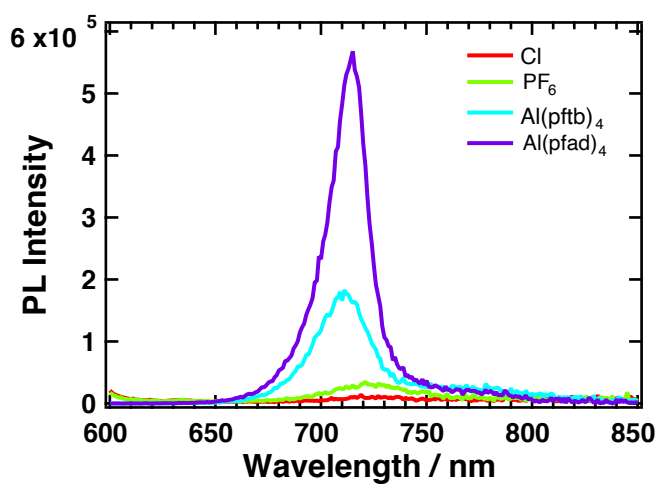


Figure B.6: Steady state photoluminescence spectra for different Cy5 thin films.

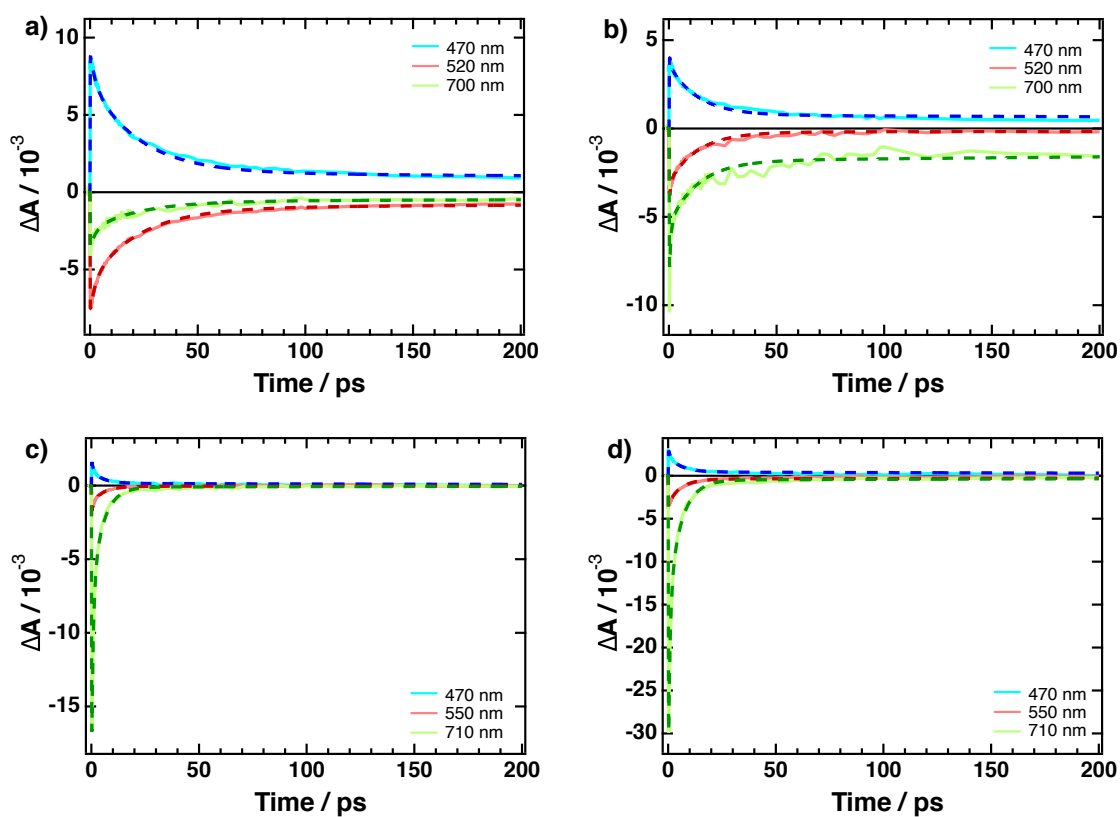
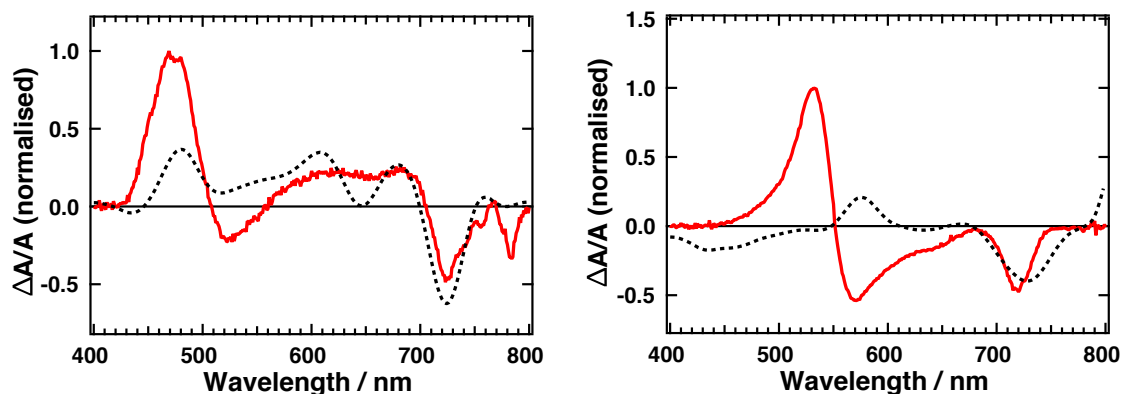
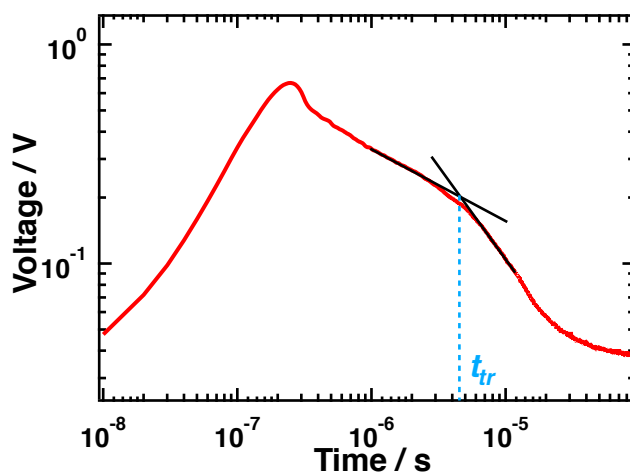


Figure B.7: Kinetic traces of different Cy5 blends incorporating different counterions: (a)  $\text{Cl}^-$ , (b)  $\text{PF}_6^-$ , (c)  $[\text{Al}(\text{pftb})_4]^-$  and (d)  $[\text{Al}(\text{pfad})_4]^-$ .



**Figure B.8:** Electroabsorption spectra of Cy5-PF<sub>6</sub> (left) and Cy5-[Al(ptbf)<sub>4</sub>] (right) fitted with a linear combination of the first and second derivative of their absorption spectra.



**Figure B.9:** An example of a photocurrent curve from a TOF measurement on Cy5-PF<sub>6</sub>. The sample was excited at  $\lambda = 630$  nm, with an applied voltage of 8 V and a resistance of 120  $\Omega$ . The transit time was found via the intersection of two asymptotes, shown by the blue dashed line.

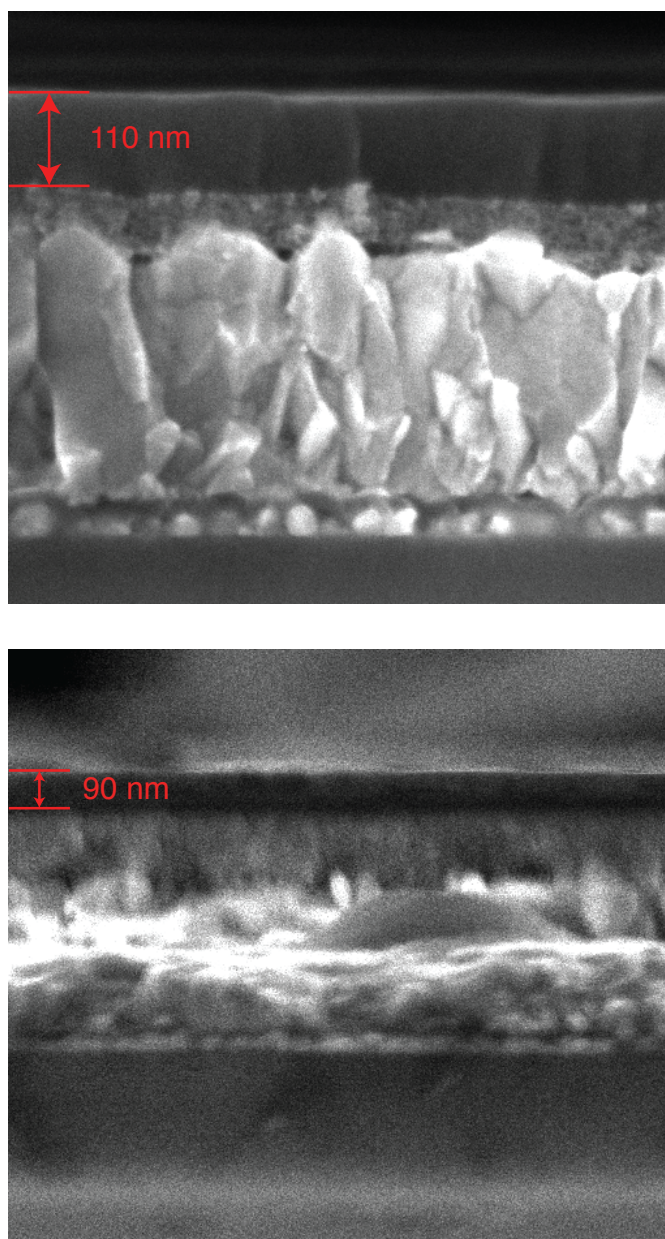


**Figure B.10:** Cross-sectional SEM images of Cy5-Cl (top) and Cy5-PF<sub>6</sub> TOF samples.

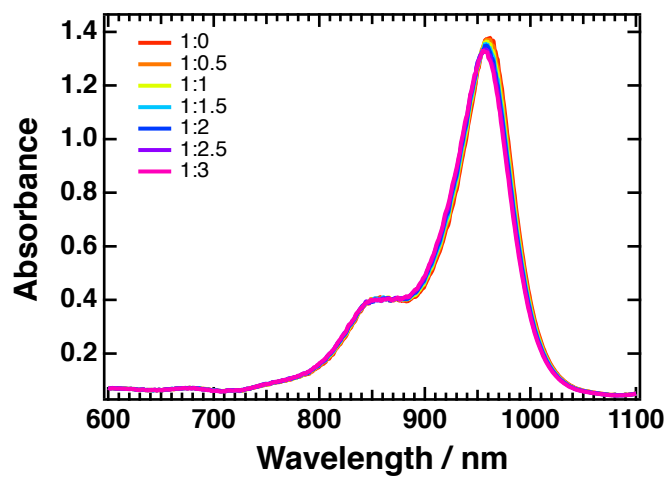


**Figure B.11:** Absorption spectra of solutions of various DCSQ1:NOBF<sub>4</sub> mol/mol blend ratios.

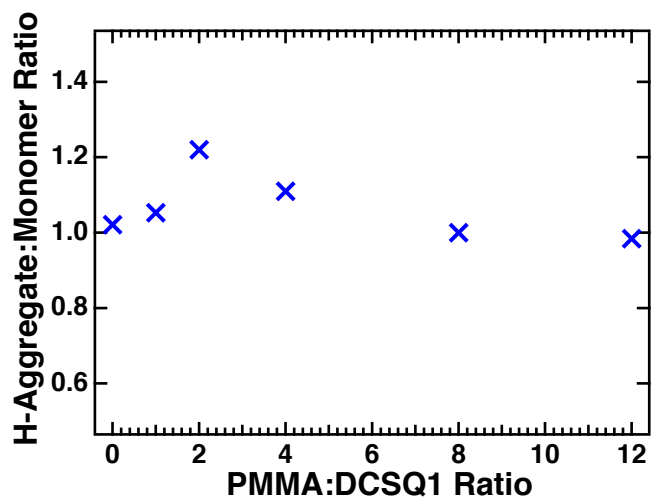


**Figure B.12:** Ratio of H-aggregate:monomer peak height as a function of the PMMA:DCSQ1 blend ratio.



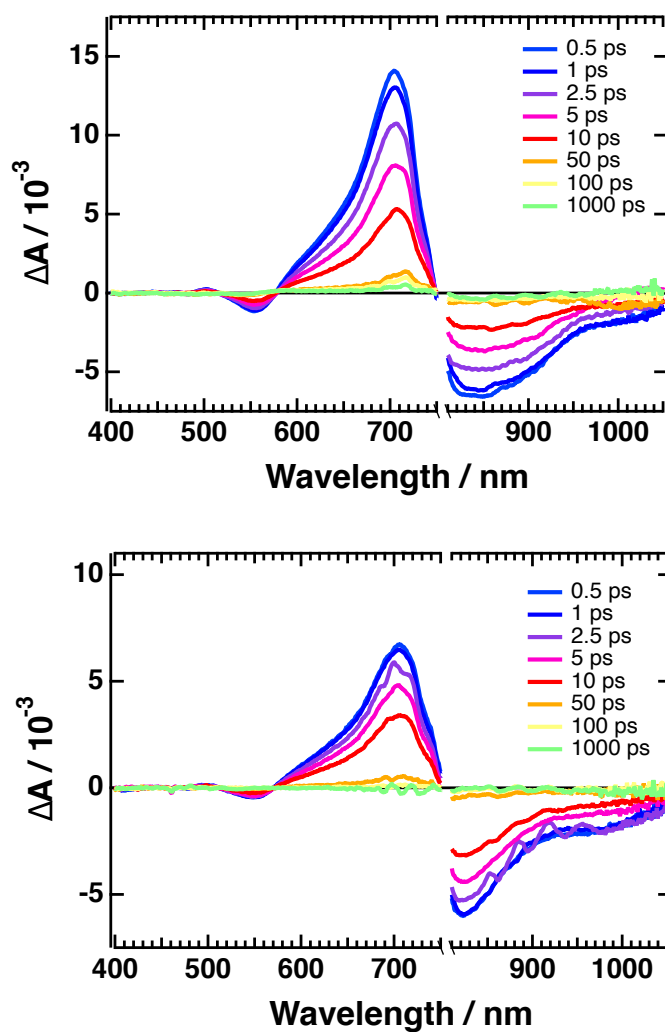


**Figure B.13:** Transient absorption spectra of 1:0 (top) and 1:12 DCSQ1:PMMA thin films. Samples were excited at 780 nm.

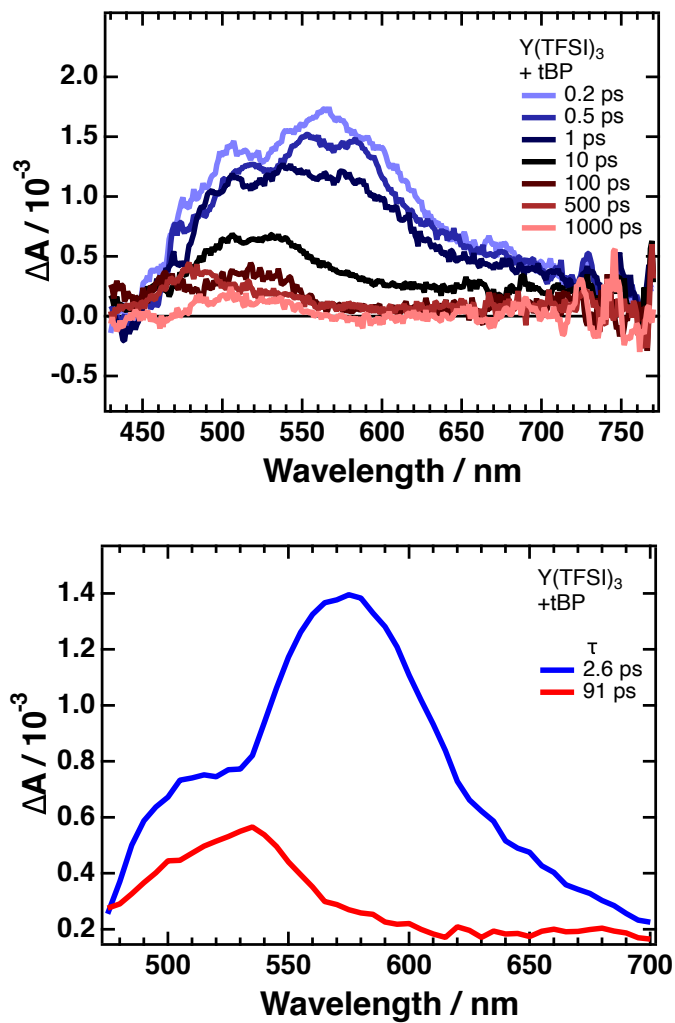


**Figure B.14:** Transient absorption spectrum of a thin film of spiro-OMeTAD with Y(TFSI)<sub>3</sub> and tBP added (top) exciting at 389 nm with a fluence of 12.5  $\mu\text{J cm}^{-2}$ . Decay associated spectra associated with fitting the TA spectrum with a bi-exponential function (bottom).

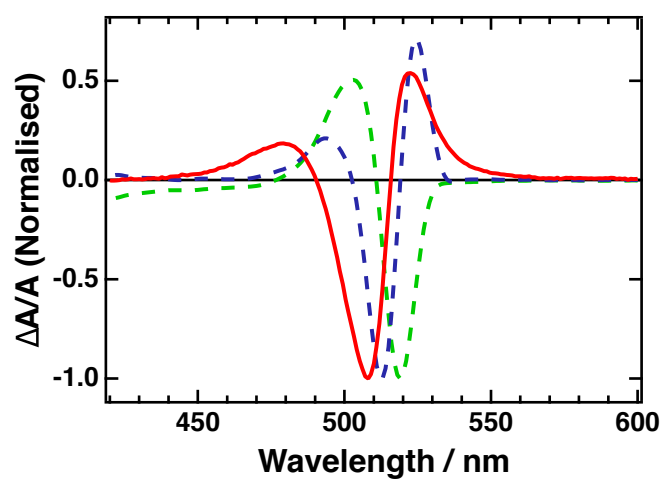


**Figure B.15:** TA spectrum of (PDMA)PbI<sub>4</sub> (red) alongside the first (green) and second (blue) derivative of the PDMA steady state absorption spectrum.

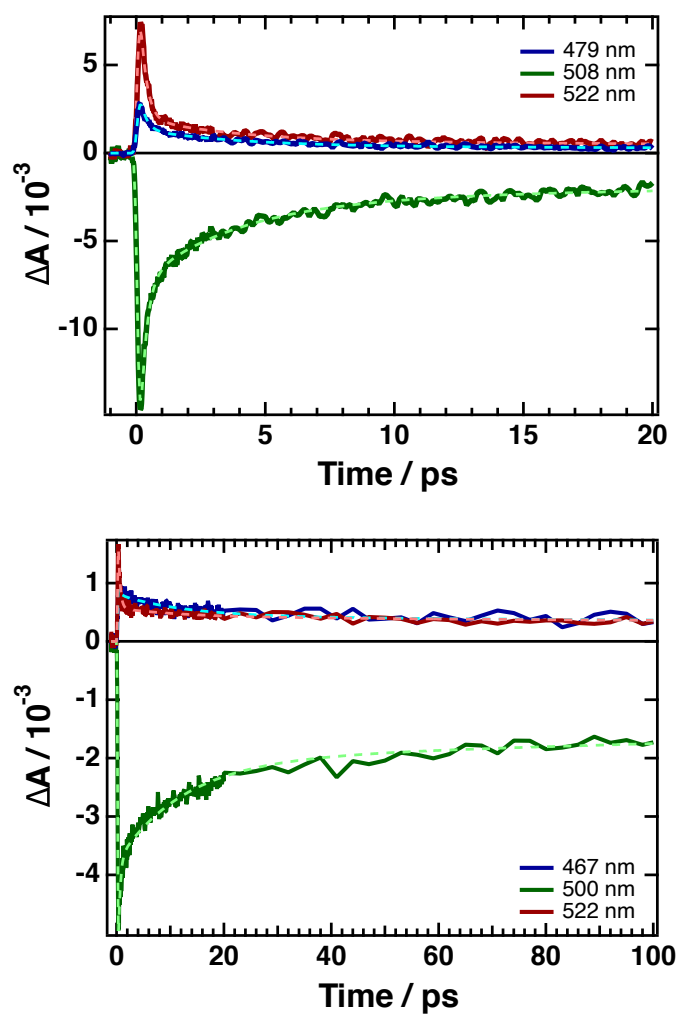


**Figure B.16:** Kinetic traces for the three peaks in the TA spectrum of (PDMA)PbI<sub>4</sub> (top) and (PDEA)PbI<sub>4</sub> (bottom). The dashed lines show the result of the global fitting procedure.

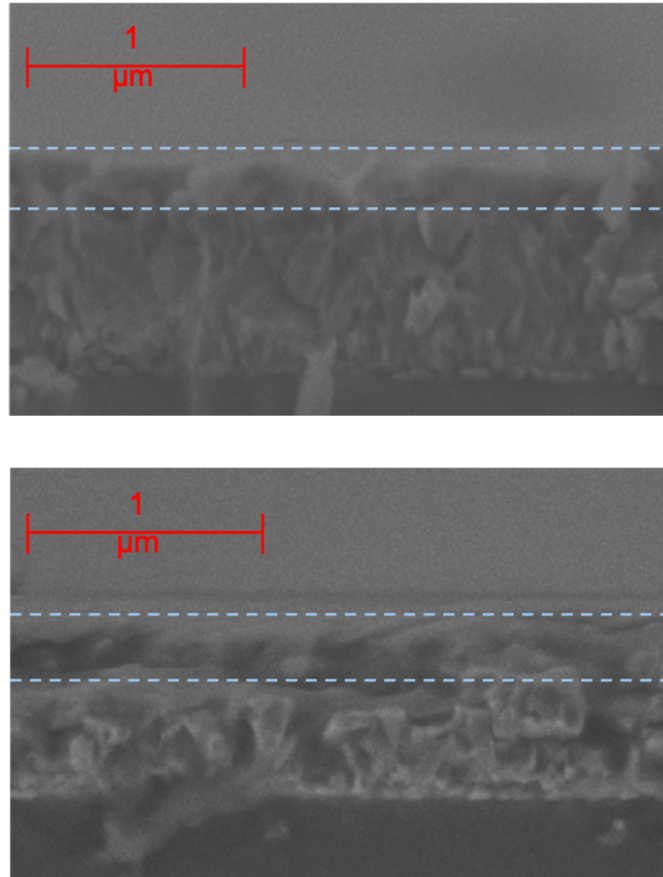


**Figure B.17:** Cross-sectional SEM images of (PDMA)PbI<sub>4</sub> (top) and (PDEA)PbI<sub>4</sub> (bottom). The samples were the same as used for the EA measurements and had the following sample structure: glass/FTO/Al<sub>2</sub>O<sub>3</sub>/perovskite/Ag.

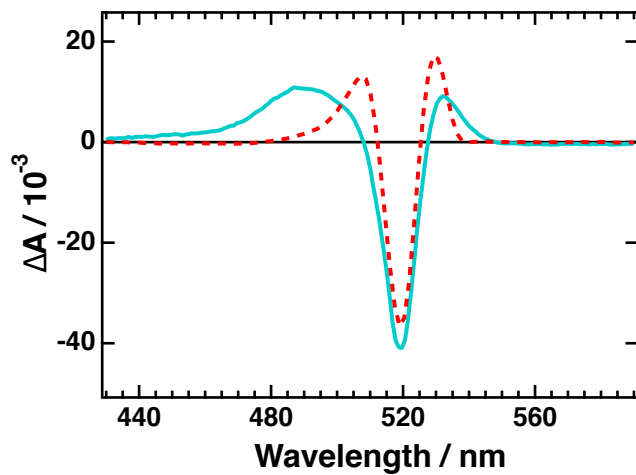


**Figure B.18:** TA spectrum of  $(\text{PEA})_2\text{PbI}_4$  (blue) fitted with a linear combination of the first and second derivative of its absorption spectrum (red).

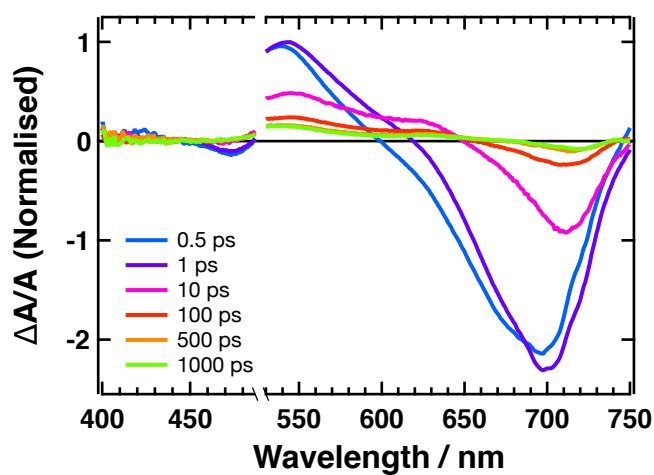


**Figure B.19:** TA spectrum of  $(\text{NDIEA})\text{FAPb}_2\text{I}_7$ , exciting at 510 nm with a fluence of  $16 \mu\text{J cm}^{-2}$ .

# George Cameron Fish

## Curriculum Vitae

Avenue du 24 Janvier 36

1020 Renens VD

+41 76 415 14 04

georgec.fish1@gmail.com

### Education

- 2018–2022 **PhD in Chemistry**, *École polytechnique fédérale de Lausanne*, Thesis title: "Unravelling the mechanism of ultrafast photoinduced charge generation in organic and hybrid photovoltaic systems", Thesis director: Prof. J.-E. Moser
- 2014–2018 **MSci. in Chemistry**, *Imperial College London*, Thesis title: "The effect of aggregation-induced energetics on the performance of bulk heterojunction solar cells employing non-fullerene acceptors", Thesis director: Prof. J.R. Durrant

### Work Experience

- 2018–2022 **Teaching Assistant**, *École polytechnique fédérale de Lausanne*
- Assistant for exercise sessions ("General Chemistry", 1st year bachelor students, 4 semesters)
  - Laboratory demonstrator (1st year bachelor students, 2 semesters)
  - Supervised 1 masters thesis
- 2020–2022 **Security Correspondent**, *Group for Photochemical Dynamics, École polytechnique fédérale de Lausanne*
- Managed safety and security within the research group
  - In charge of training new students and collaborators
- 2017 **Summer Research Intern**, *KAUST Solar Centre, King Abdullah University of Science and Technology, Saudi Arabia*
- Investigated the impact of additives on charge generation in organic solar cells employing new novel acceptor materials
  - Learnt state of the art fabrication and characterisation techniques

### List of publications

- G. C. Fish, A. T. Terpstra, A. Dučinskas, M. Almalki, M. Grätzel, J. V. Milić, J. -E. Moser. **Investigating the Impact of Spacer Size and Layer Orientation on Charge Transfer Excitons in 2D Perovskites**, *Manuscript in preparation*, 2022
- T. P. Baumeler, E. A. Alharbi, G. C. Fish, B. I. Carlsen, G. Kakavelakis, J. Ho Yum, M. D. Mensi, J. Gao, F. T. Eickemeyer, J. -E. Moser, S. M. Zakeeruddin, M. Grätzel. **Post-engineering via inorganic salts to reach highly efficient and stable perovskite solar cells**, *Manuscript in preparation*, 2022
- S. Kim, G. C. Fish, E. Socie, A. T. Terpstra, J. -E. Moser, M. Grätzel, N. Park. **Anaerobic Photo-Doping of Spiro-OMeTAD for Highly Stable and Efficient Perovskite Solar Cells**, *Manuscript submitted for publication*, 2022
- G. C. Fish, J. -E. Moser. **Spatio-Temporal Dynamics of Free and Bound Carriers in Photovoltaic Materials**, *Chimia*, 2022 **76**, 552
- A. Dučinskas, G. C. Fish, M. A. Hope, L. Merten, D. Moia, A. Hinderhofer, L. C. Carbone, J. -E. Moser, F. Schreiber, J. Maier, J. V. Milić, M. Grätzel. **The Role of Alkyl Chain Length and Halide Counter Ion in Layered Dion-Jacobson Perovskites with Aromatic**

- Spacers**, *J. Phys. Chem. Lett.* 2021, **12**, 10325-10332
6. G. C. Fish, J. M. Moreno-Naranjo, A. Billion, D. Kratzert, E. Hack, I. Krossing, F. Nüesch, J. -E. Moser. **Critical role of H-aggregation for high-efficiency photoinduced charge generation in pristine pentamethine cyanine salts**, *Phys. Chem. Chem. Phys.* 2021, **23**, 23886-23895
  7. E. A. Alharbi, A. Krishna, T. P. Baumeler, M. Dankl, G. C. Fish, F. Eickemeyer, O. Ouellette, P. Ahlawat, V. Škorjanc, E. John, B. Yang, L. Pfeifer, C. E. Avalos, L. Pan, M. Mensi, P. A. Schouwink, J. -E. Moser, A. Hagfeldt, U. Rothlisberger, S. M. Zakeeruddin, M. Grätzel. **Methylammonium Triiodide for Defect Engineering of High-Efficiency Perovskite Solar Cells**, *ACS Energy Lett.* 2021, **6**, 3650-3660
  8. A. Mishra, P. Ahlawat, G. C. Fish, F. Jahanbakhshi, M. Mladenović, M. Almalki, M. A. Ruiz-Preciado, M. C. Gelvéz-Rueda, D. J. Kubicki, P. A. Schouwink, V. Dufoulon, T. Schneeberger, A. Aslanzadeh, F. C. Grozema, S. M. Zakeeruddin, J. -E. Moser, U. Rothlisberger, L. Emsley, J. V. Milić, M. Grätzel. **Naphthalenediimide/Formamidinium-Based Low-Dimensional Perovskites**, *Chem. Mater.* 2021, **33**, 6412-6420
  9. Y. Ren, N. Flores-Díaz, D. Zhang, Y. Cao, J.-D. Decoppet, G. C. Fish, J. -E. Moser, S. M. Zakeeruddin, P. Wang, A. Hagfeldt, M. Grätzel. **Blue Photosensitizer with Copper(II/I) Redox Mediator for Efficient and Stable Dye-Sensitized Solar Cells**. *Adv. Func. Mater.* 2020, **30**, 2004804.
  10. A. Prlj, T. Begušić, Z. T. Zhang, G. C. Fish, M. Wehrle, T. Zimmermann, S. Choi, J. Roulet J. -E. Moser, J. Vaníček. **Semiclassical Approach to Photophysics Beyond Kasha's Rule and Vibronic Spectroscopy Beyond the Condon Approximation. The Case of Azulene**, *J. Chem. Theory Comput.* 2020, **16**, 2617-2626
  11. H. Cha, G. Fish, J. Luke, A. Alraddadi, H. W. Lee, W. Zhang, Y. Dong, S. Limbu, A. Wadsworth, I. P. Maria, L. Francàs, H. L. Sou, T. Du, J. -S. Kim, M. A. McLachlan, I. McCulloch, J. R. Durrant. **Suppression of Recombination Losses in Polymer:Non-fullerene Acceptor Organic Solar Cells due to Aggregation Dependence of Acceptor Electron Affinity**, *Adv. Energy Mater.* 2019, **9**, 1901254
  12. E. M. Speller, A. J. Clarke, N. Aristidou, M. F. Wyatt, L. Francàs, G. Fish, H. Cha, H. K. H. Lee, J. Luke, A. Wadsworth, A. D. Evans, I. McCulloch, J. -S. Kim, S. A. Haque, J. R. Durrant, S. D. Dimitrov, W. C. Tsoi, Z. Li. **Toward Improved Environmental Stability of Polymer:Fullerene and Polymer:Non-fullerene Organic Solar Cells: A Common Energetic Origin of Light- and Oxygen-Induced Degradation**, *ACS Energy Lett.* 2019, **4**, 846-852

## Conference contributions

### Oral presentations

- Central European Conference on Photochemistry 2022, Bad Hofgastein, Austria
- International Conference on Photochemistry 2021, Virtual
- Swiss Chemical Society Fall Meeting 2020, Virtual

### Poster presentations

- NCCR MUST Annual Meeting 2021, Grindelwald, Switzerland
- Swiss Chemical Society Fall Meeting 2019, Zürich, Switzerland
- Swiss Photochemical Society Meeting 2019, Fribourg, Switzerland
- 11th Conference on Hybrid and Organic Photovoltaics, HOPV 2019, Rome, Italy
- NCCR MUST Annual Meeting 2019, Grindelwald, Switzerland